Growth and Characterization of ZnO based Heterojunction diodes and ZnO Nanostructures by Pulsed Laser Ablation

Thesis submitted to
COCHIN UNIVERSITY OF SCIENCE AND TECHNOLOGY
in partial fulfillment of the requirements
for the award of the degree of
DOCTOR OF PHILOSOPHY

Ajimsha R S

Department of Physics
Cochin University of Science and Technology
Cochin – 682 022, Kerala, India

February 2008

Growth and Characterization of ZnO based Heterojunction diodes and ZnO Nanostructures by Pulsed Laser Ablation

Ph.D thesis in the field of material science

Author:

Ajimsha R S
Optoelectronic Devices Laboratory
Department of Physics
Cochin University of Science and Technology
Cochin – 682 022, Kerala, India
email: ajimsha@gmail.com

Supervisor:

Dr. M.K. Jayaraj
Reader
Optoelectronics Device Laboratory
Department of Physics
Cochin University of Science and Technology
Cochin – 682 022, Kerala, India
email: mkj@cusat.ac.in

February 2008

Dedicated to my Parents

Dr. M.K. Jayaraj
Reader
Department of Physics
Cochin University of Science and Technology
Cochin – 682 022

25th February 2008

Certificate

Certified that the work presented in this thesis entitled "*Growth and Characterization of ZnO based Heterojunction diodes and ZnO Nanostructures by Pulsed Laser Ablation*" is based on the authentic record of research done by Mr. Ajimsha R S under my guidance in the Department of Physics, Cochin University of Science and Technology, Cochin – 682 022 and has not been included in any other thesis submitted for the award of any degree.

Dr. M. K. Jayaraj

(Supervising Guide)

Phone : +91 484 2577404 extn 33 Fax: 91 484 2577595 email: mkj@cusat.ac.in

Declaration

Certified that the work presented in this thesis entitled "*Growth and Characterization of ZnO based Heterojunction diodes and ZnO Nanostructures by Pulsed Laser Ablation*" is based on the original research work done by me under the supervision and guidance of Dr. M. K. Jayaraj, Reader, Department of Physics, Cochin University of Science and Technology, Cochin-682022 has not been included in any other thesis submitted previously for the award of any degree.

Cochin – 22
25th Februaryr 2008 Ajimsha R. S.

Acknowledgements

The investigations in this thesis have been carried out under the supervision of Dr. M. K. Jayaraj, Reader, Dept. of Physics, Cochin University of Science and Technology. I express my deep sense of gratitude for his excellent guidance, competent advice, keen observations and persistent encouragement as well as personal attention given to me during the entire course of work, without which the successful completion of this work would not have been possible. I am deeply indebted to him for his kindness, constant encouragement and support.

It is with a particular pleasure that I acknowledge Dr. L .M. Kukreja, Raja Ramanna Centre for Advanced Technology, Indore for being as the principal collaborator of my project. I greatly acknowledge his valuable suggestions and discussions throughout this work.

I extend my sincere thanks to Prof. Godfrey. Louis, the Head of the Department of Physics and all other former Heads of the Dept. for allowing me to use the facilities. I greatly acknowledge the help and guidance of all the faculty members of the Department of Physics right from the beginning of my research work.

I wish to thank Dr. V. Unnikrishnan Nayar (Dean, Faculty od Science, CUSAT) and Dr. V. P. Mahadevan Pillai (Head, Department of Optoelectronics, University of Kerala) for their support and encouragement right from the MPhil classes

I also thank Dr. B. N. Sigh, Pankaj Misra and Dr. V. K. Dixit, Raja Ramanna Centre for Advanced Technology, Indore for the valuable help during the course of PhD work.

I wish to thank SAIF, IIT Chennai and Dr. P. V. Sathyam(IOP, Bhuvanewar) for TEM measurements. I express my sincere thanks to Cochin University and DAE-BRNS for financial assistance at the various levels of my PhD program.

With a sense of gratitude, I am thankful to all the office and library staff of the Department of Physics and the technical staff at USIC for all the help and cooperation.

I sincerely acknowledge Dr. B. Premlet for driving towards the beautiful world of Physics.I would like to thank Dr. K. Manzoor, Dr. Prasanth, Dr. Deepthy Menon and Dr. U. Sajeev for their encouragement all the time.

I specially appreciate the sincere support of Dr. Aldrin and Dr. Manoj for all the guidance and encouragement given throughout the research work. I would like to express my sincere appreciation to my colleagues in the OED lab Reshmi, Rahana, Mini, Anila teacher, Vanaja Madam, Asha, Saji, Aneesh, Sreeja, Ratheesh, Arun, Ragitha and Krishna prasad for all the help they had extended.

I remember my friends Jayakrishnan, Vinu V Namboory, Manu Punnen John P. U. Jijo, Gopikrishnan, V. C. Kishore, Binoy Joseph, Manoj. E, Hysen Thomas, Sreekumar. A, Ratheesh. P. M, Radhakrishnan, Manu. B, Rajesh. M, Chithra R Nayak and Jisha for their valuable friendship and some memorable moments during various stages of my life at CUSAT. I also extend my thanks to all my friends in Dept. of Physics, CUSAT for their sincere help and co operation throughout this work.

I wish to express my sincere gratitude to Raj Mohan, Swarish, Ranjith. R Aneehsettan, Biju chettan, Rajeshettan, Muraliettan, Lakshmi Narayan, Raviettan and all other malayali friends in RRCAT, Indore for their love affection during the time I spent in Indore.

I am also thankful to Prince sir, Anuraj, Vineetha. B, Sukesh and Saritha for their valuable help during various stages of my work.

Words are inadequate to express the beauty of the moments which I spent with my dear friends Anoop G, and Rani J R right from the MPhil classes.

I am deeply indepted to my Swapna chechi and Unniettan for their love, affection, constant encouragement and support throughout my work.

Now it is time to remember my Joshy sir and family who has been a stable support during the entire course of work with their brain and heart spent a lot for me.

I express my deep sense of gratitude to my fiancee Devi and her family for their inspiration in the final stages of my work.

I record my deep and utmost gratitude to my Amma and Achan for selfless support, motivation, encouragements, patience and tolerance during the entire period of my work.

I thank all my well wishers.

Last but not the least I thank God almighty for the blessing he has showed on me.

Ajimsha R S

Contents

Chapter 2
Experimental techniques and characterization tools

Chapter 3
Transparent p-$AgCoO_2$/n-ZnO heterojunction fabricated by pulsed laser deposition

Preface

Transparent conducting oxides (TCO's) have been known and used for technologically important applications for more than 50 years. The oxide materials such as In_2O_3, SnO_2 and impurity doped SnO_2: Sb, SnO_2: F and In_2O_3: Sn (indium tin oxide) were primarily used as TCO's. Indium based oxides had been widely used as TCO's for the past few decades. But the current increase in the cost of indium and scarcity of this material created the difficulty in obtaining low cost TCO's. Hence the search for alternative TCO material has been a topic of active research for the last few decades. This resulted in the development of various binary and ternary compounds. But the advantages of using binary oxides are the easiness to control the composition and deposition parameters. ZnO has been identified as the one of the promising candidate for transparent electronic applications owing to its exciting optoelectronic properties. Some optoelectronics applications of ZnO overlap with that of GaN, another wide band gap semiconductor which is widely used for the production of green, blue-violet and white light emitting devices. However ZnO has some advantages over GaN among which are the availability of fairly high quality ZnO bulk single crystals and large excitonic binding energy. ZnO also has much simpler crystal-growth technology, resulting in a potentially lower cost for ZnO based devices.

Most of the TCO's are n-type semiconductors and are utilized as transparent electrodes in variety of commercial applications such as photovoltaics, electrochromic windows, flat panel displays. TCO's provide a great potential for realizing diverse range of active functions, novel functions can be integrated into the materials according to the requirement. However the application of TCO's has been restricted to transparent electrodes,

notwithstanding the fact that TCO's are n-type semiconductors. The basic reason is the lack of p-type TCO, many of the active functions in semiconductor originate from the nature of *pn*-junction. In 1997, H. Kawazoe et al reported the $CuAlO_2$ as the first p-type TCO along with the chemical design concept for the exploration of other p-type TCO's. This has led to the fabrication of all transparent diode and transistors.

Fabrication of nanostructures of TCO has been a focus of an ever-increasing number of researchers world wide, mainly due to their unique optical and electronic properties which makes them ideal for a wide spectrum of applications ranging from flexible displays, quantum well lasers to *in vivo* biological imaging and therapeutic agents. ZnO is a highly multifunctional material system with highly promising application potential for UV light emitting diodes, diode lasers, sensors, etc. ZnO nanocrystals and nanorods doped with transition metal impurities have also attracted great interest, recently, for their spin-electronic applications

This thesis summarizes the results on the growth and characterization of ZnO based diodes and nanostructures by pulsed laser ablation. Various ZnO based heterojunction diodes have been fabricated using pulsed laser deposition (PLD) and their electrical characteristics were interpreted using existing models. Pulsed laser ablation has been employed to fabricate ZnO quantum dots, ZnO nanorods and ZnMgO/ZnO multiple quantum well structures with the aim of studying the luminescent properties.

Chapter 1 presents a brief description on the transparent conducting oxide (TCO). It includes an introduction, general properties, classification of TCO, brief description and a short review of the materials studied in the present

investigation. Introduction to nanotechnology, followed by description of basic nanostructures such as quantum dot, nanorods and quantum well and a short review of ZnO based nanostructures are also presented in this chapter

Chapter 2 describes in detail the growth techniques and characterization tools employed for ZnO based heterojunction diodes and ZnO based nanostructures. The heterojunction diodes, nanorods and quantum wells were deposited using PLD. The details of PLD technique with a short description on the rf magnetron sputtering and vacuum evaporation are also included in this chapter. Various physical and chemical synthesis techniques of quantum dots, especially liquid phase laser ablation (LP-PLA) technique has been described in this chapter. Thin films grown were characterized by various analytical techniques, thickness measurement using stylus profiler, morphological analysis using scanning electron microscope (SEM) and atomic force microscopy (AFM), composition analysis like energy dispersive x-ray analysis (EDX), inductively coupled plasma.- atomic emission spectroscopy (ICP-AES) analysis and x-ray photoelectron spectroscopy (XPS), structural characterization using x-ray diffraction method, microstructure analysis using transmission electron microscopy (TEM), determination of band gap, Raman spectra studies, photoluminescence, electrical characterization consisting of two probe resistivity method and hall measurement and thermo power measurement are briefly described in this chapter.

Chapter 3 describes the growth and characterization of transparent p-$AgCoO_2$/n-ZnO heterojunction diode by PLD. The PLD of $AgCoO_2$ thin films was carried out using the sintered target of $AgCoO_2$, which was synthesized in-house by hydrothermal process. The band gap of these thin films was found to be

~3.89 eV and they had transmission of ~ 55% in the visible spectral region. Although Hall measurements could only indicate mixed carrier type conduction but thermoelectric power measurements of Seebeck coefficient confirmed the p-type conductivity of the grown $AgCoO_2$ films. The PLD grown ZnO films showed a band gap of ~3.28 eV, an average optical transmission of ~85% and n-type carrier density of ~4.6 x 10^{19} cm^{-3}. The junction between p-$AgCoO_2$ and n-ZnO was found to be rectifying. The ratio of forward current to the reverse current was about 7 at 1.5V. The diode ideality factor was much greater than 2.

Chapter 4 deals with the fabrication of p-Si/ZnO heterojunction diode by the PLD of ZnO at different oxygen pressures. These heterojunctions were found to be rectifying with the maximum forward to reverse current ratio of about 1000 in the applied voltage range from -5 to +5 V. Turn-on voltage of the heterojunctions was found to depend on the ambient oxygen pressure during the growth of the ZnO film. The current density-voltage characteristics and the variation of the series resistance of the n-ZnO/p-Si heterojunctions were found to be in line with the Anderson model and Burstein-Moss (BM) shift.

Chapter 5 presents the studies on luminescent ZnO based multiple quantum wells and nanorods. ZnO/ZnMgO Multiple Quantum Well (MQW) of well layer thickness of 2 nm was grown on sapphire (0001) substrate by PLD at a substrate temperature 400^{o}C. Efficient room temperature photoluminescence (PL) was observed from these MQW's, which was found to be blue shifted as compared to the room temperature near band edge PL from ZnO thin film of 200 nm grown at same experimental conditions. ZnO thin films were deposited using room temperature PLD by varying the oxygen pressure and found a pressure window for the growth of (002) oriented polycrystalline ZnO thin films.

Morphological analysis using Scanning Electron Microscope (SEM) and Atomic Force Microscopy (AFM) demonstrated the formation ZnO nanorods at a particular oxygen pressure in this pressure window. Room temperature violet luminescence was observed from these ZnO nano rods. Temperature dependent photoluminescent studies of both ZnMgO/ZnO MQW and ZnO nano rods were carried out and the results are discussed.

Chapter 6 describes the preparation of highly transparent, luminescent and bio-compatible ZnO quantum dots in water, methanol and ethanol using liquid phase pulsed laser ablation technique without the aid of any surfactant. Transmission electron microscopy (TEM) analysis confirms the formation of good crystalline ZnO quantum dots with uniform size distribution of 7 nm. The emission wavelength was tuned by playing the native defect chemistry ZnO quantum dots and laser fluence. Maximum concentration ZnO quantum dots without loosing the transparency was observed to be 17 μg/ml from inductively coupled plasma - atomic emission spectroscopy (ICP-AES) analysis. Highly luminescent non-toxic ZnO quantum dots have exciting application potential as fluorescent probes in biomedical applications. ***Chapter 7*** summarizes the main results in the thesis and the scope for future works.

Part of the thesis has been published in internationally referred journals

1 Transparent p-$AgCoO_2$/n-ZnO diode heterojunction fabricated by pulsed laser deposition.
R. S. Ajimsha, K. A. Vanaja, M. K. Jayaraj, P. Mishra, and L .M. Kukreja Thin Solid Films 515 (2007) 7352.

2 Luminescence from surfactant free ZnO quantum dots prepared by Laser ablation in liquids.
R. S. Ajimsha, G. Anoop, Arun aravind and M. K. Jayaraj Electrochem. Solid St. Lett. 11 (2008) K 14.

3 Electrica**l** Characteristics of n-ZnO/p-Si Heterojunction Diodes Grown by Pulsed Laser Deposition at Different Oxygen Pressures.
R. S. Ajimsha, M. K. Jayaraj, and L. M. Kukreja. J. Electron. Mater. DOI: 10.1007/s11664-007-0365-4 (**In press).**

4 Violet luminescence from ZnO nanorods grown by room temperature Pulsed Laser Deposition.
R. S. Ajimsha, R. Manoj and M. K. Jayaraj. (Submitted to Curr. Appl. Phys.).

5 Photoluminescence studies on ZnMgO/ZnO Quantum well grown by low temperature Pulsed Laser Deposition
R. S. Ajimsha, M. K. Jayaraj, P. Mishra and L .M. Kukreja (To be communicated).

Conference Proceedings

1 Transparent p-$AgCoO_2$/n-ZnO p-n Junction fabricated by pulsed laser deposition
R. S. **Ajimsha,** K. A. Vanaja, M. K. Jayaraj, P. Mishra and L .M. Kukreja, PLD-2005.

2 Room temperature Photoluminescence from Low temperature Grown ZnMgO/ZnO Quantum well by Pulsed Laser Deposition
R. S. Ajimsha, M. K. Jayaraj, P. Mishra, and L .M. Kukreja, PLD-2007.

Other internationally referred journals to which author has contributed

1 Characterization of Radio Frequency plasma using Langmuir Probe and Optical Emission Spectroscopy
M. Nisha, K. J. Saji, **R. S Ajimsha**, N. V Joshy, and M. K Jayaraj, J. of Appl. Phys. 99, 033304 (2006).

2 Effect of surface roughness on Photoluminescent spectra of silicon nanocrystals grown by off axis pulsed laser deposition
J. R. Rani, **R. S. Ajimsha,** V. P. Mahadevan Pillai, M. K. Jayaraj and R. S. Jayasree. J. Appl. Phys. 100, 014302 (2006).

3 p-type electrical conduction α-$AgGaO_2$ delafossite thin film
K. A. Vanaja, **R. S. Ajimsha**, A. S. Asha and M. K. Jayaraj, Appl. Phys. Lett. 88 (2006) 212103.

4 Growth of Zinc Oxide thin films for optoelectronic application by pulsed laser deposition
K. J. Saji, R. Manoj, **R. S. Ajimsha**, and M. K. Jayaraj, Proc. SPIE Vol. 6286, 62860D (Aug. 28, 2006).

5 Pulsed Laser Deposition of p-type α-$AgGaO_2$ thin films
K. A. Vanaja, **R. S. Ajmsha**, A. S. Asha, K. Rajeev Kumar, and M. K. Jayaraj. Thin Solid Films 516 (2008) 1426.

6 Synthesis of highly luminescent, bio-compatible ZnO quantum dots doped with Na
B. Vineetha, K. Manzoor, **R. S. Ajimsha**, P. M. Aneesh and M. K. Jayaraj. Synthesis and Reactivity in Inorganic, Metal-organic and Nano-Metal Chemistry 38 (2008) 1.

7 p-$AgCoO_2$/n-ZnO heterojunction diode grown by rf magnetron sputtering
K. A.Vanaja, P. Umannada, **R. S. Ajimsha**, S. Jayalekshmi and M. K.Jayaraj (Bulletin of Material Science: under revision).

8 Enhanced nonlinear optical properties of Er doped Si nanoparticles prepared by off-axis pulsed laser deposition
J. R. Rani, V. P. Mahadevan Pillai, C. S. Suchand Sandeep, Reji Philip, **R. S. Ajimsha** and M. K. Jayaraj (To be communicated).

Conference proceedings

1 Photoluminescence characteristics of silicon nanoparticles prepared by off axis PLD,
J. R. Rani, **R. S. Ajimsha**, V. P. M.Pillai and M. K. Jayaraj,
Proceedings of National conference on Luminescence and its applications Vol XII (2005) p164-166.

2 Optical characterization of Silicon nanoparticles prepared by off axis PLD.
J. R. Rani, **R. S. Ajimsha**, V. P. Mahadevan Pillai and M. K. Jayaraj, NLS 2004.

3 Off axis pulsed laser deposition of silicon nanoparticles,
J. R.Rani, **R. S. Ajimsha**, R. Manoj, V. P. Mahadevan Pillai and M.K.Jayaraj, IUMRS-ICA 2004, Taiwan.

4 Studies on RF plasma using Optical Emission Spectroscopy
K. J. Saji.**,** .M. Nisha, **R. S. Ajimsha.**, N. V. Joshy and M. K Jayaraj, 19th National Symposium on Plasma and Technology, PLASMA – 2004.

Chapter 1

Introduction to transparent conducting oxides and nanostructures

This chapter gives an overview of the development of transparent conducting oxides, particularly the zinc oxide as an n type conductor. The recent development of delafossite materials as p type transparent conductors brings the possibility of uv emitting light emitting diodes and transparent p–n junction. An introduction to nanostructures followed by a review of various zinc oxide based nanostructures is presented in this chapter.

1.1. Introduction to transparent conducting oxides

Semiconductor physics has been advanced significantly in the field of research and industry in the past few decades due to it's numerous practical applications. There is immense interest in developing those materials, which maintain their required properties under extreme environmental conditions. One of the most important fields of current interest in material science is the fundamental aspects and applications of semiconducting transparent thin films. Such materials are highly conducting and exhibit high transparency in the visible region of the electromagnetic spectrum. Because of the unique property, transparent conducting oxides (TCO's) are finding wide range of applications in research and industry. They are fundamental layers of the basic devices in the transparent electronics.

A TCO is a wide band gap semiconductor that has relatively high concentration of free electrons in the conduction band. These arise either from defects in the material or from extrinsic dopants, the impurity levels which act as shallow donor level. The high carrier concentration causes the absorption of electromagnetic radiations in both visible and IR portions of the spectrum [1]. A TCO must necessarily represent a compromise between electrical conductivity and optical transmittance; a careful balance between these properties is required. Reduction of the resistivity involves either an increase in carrier concentration or in the mobility. Increase in the former will enhance the absorption in the visible region while increase in mobility has no adverse effect on optical properties. Therefore the focus of research for new TCO materials is on achieving materials with higher electron mobilities. The above goal can be attained by synthesizing

the material with longer electron relaxation times or lower electron effective mass.

1.2. General properties of transparent conducting oxides

1.2.1. Transparency and conductivity

As far as the properties of a solid are concerned, one can see that optical transparency and electrical conductivity are antonyms to each other. This can be easily proved using the Maxwell's equations of electromagnetic theory as described below [2].

For electromagnetic (em) waves passing through an uncharged semiconducting medium, the solution to Maxwell's equation gives the real and complex parts of the refractive index as

$$n^2 = \frac{\varepsilon}{2}\left[\left\{1+\left(\frac{2\sigma}{\upsilon}\right)^2\right\}^{1/2}+1\right] \qquad (1.1)$$

$$k^2 = \frac{\varepsilon}{2}\left[\left\{1+\left(\frac{2\sigma}{\upsilon}\right)^2\right\}^{1/2}-1\right] \qquad (1.2)$$

where n is the refractive index of the medium, k is the extinction coefficient, ε is the dielectric constant, σ is the conductivity of the medium and ν is the frequency of the electromagnetic radiation. In the case of an insulator, where $\sigma \to 0$, then $n \to \varepsilon^{1/2}$ and $k \to 0$. This implies that an insulator is transparent to electromagnetic waves.

For a perfect conductor, the solution to the Maxwell's equation yields, the reflected and transmitted component of the electric field vector as $E_R = -E_I$ and

$E_T = 0$. This means that the wave is totally reflected with 180^0 phase difference. In other words, a good conductor reflects the radiations incident on it, while a good insulator is transparent to the electromagnetic radiations.

1.2.2. Correlation of electrical and optical properties

The optical phenomena in the IR range can be explained on the basis of Drude's theory for free electrons in metals [3-5]. When the free electrons interact with an em field, it may lead to polarization of the field within the material. It affects the relative permittivity ε. For an electron moving in an electric field, the equation of motion can be written as,

$$m\left(\frac{d}{dt}+\frac{1}{\tau}\right)\delta v(t) = F \qquad (1.3)$$

where τ is the relaxation time .

The force on an electron in an alternating field is given by

$$F = -eE\, e^{-i\omega t} \qquad (1.4)$$

Let us assume a solution to (1.4) in the form $\delta \mathbf{v} = \delta v\, e^{-i\omega t}$

Then (1.3) becomes,

$$m\left(-i\omega+\frac{1}{\tau}\right)\delta v = -eE$$

or ,
$$\delta v = -\frac{e\tau/m}{1-i\omega\tau} \qquad (1.5)$$

The current density is

$$j = nq\delta v = \frac{ne^2\tau}{m(1-i\omega\tau)}E,$$

where n is the electron concentration and q is the charge on the electron.

The electrical conductivity is

$$\sigma(\omega) = \frac{ne^2\tau}{m(1-i\omega\tau)} = \sigma_0 \frac{1+i\omega\tau}{1+(\omega\tau)^2} \qquad (1.6)$$

Here, $\sigma_0 = ne^2\tau / m$ is the dc conductivity.

At high frequencies, $\omega\tau >> 1$, we can write,

$$\sigma(\omega) = \sigma_0\left(\frac{1}{(\omega\tau)^2} + \frac{i}{\omega\tau}\right) = \frac{ne^2}{m\omega^2\tau} + i\frac{ne^2}{m\omega}$$

In this equation the imaginary term is dominant and is independent of τ. Thus we can express the result as a complex dielectric constant instead of expressing it as a complex conductivity.

The dielectric constant $\varepsilon = 1 + (4\pi P/E)$

Where $P = -\dfrac{ne^2/m}{\omega^2 + i\omega/\tau}E$

Then, $$\varepsilon(\omega) = 1 - \frac{4\pi ne^2/m}{\omega^2 + i\omega/\tau} \qquad (1.7)$$

This expression gives the dielectric constant of a free electron gas. For $\tau \to \infty$ the dielectric constant is positive and real if $\omega^2 > 4\pi ne^2/m$. Electromagnetic wave cannot propagate in a medium with negative dielectric constant because then wave vector is imaginary and the wave decays exponentially. Waves incident on such a medium are totally reflected. We can denote the cut off frequency as $\omega_p = \left(4\pi ne^2/m\right)^{1/2}$ this is known as the plasma frequency. The material is transparent to the em radiation whose frequency is greater than the plasma frequency.

1.2.3. Electrical properties

Numerous investigations have been made on the electrical properties of transparent conducting oxide films to understand the conduction phenomena [6,7]. Researchers have made a systematic study on the effect of various parameters such as nature of substrate, substrate temperature, film thickness, dopant and its concentration etc [8,9] on the electrical properties of TCO films. The high conductivity of the TCO films results mainly from non stoichiometry. The conduction electrons in these films are supplied from donor sites associated with oxygen vacancies or excess metal ions [10]. These donor sites can be easily created by chemical reduction. Unintentional doping (which happens mainly in the case of film deposition by spray pyrolysis), intentional doping and contamination by alkali ions from the glass substrate can affect electrical conductivity.

One of the major factors governing the conductivity of TCO films is the carrier mobility. The mobility of the carriers in the polycrystalline film is dependent on the mechanism by which carriers are scattered by lattice

imperfections. The various scattering mechanisms involved in semiconducting thin films are acoustic deformation potential scattering [11], piezoelectric scattering [12], optical phonon scattering [13] neutral impurity scattering [14], ionized impurity scattering [15], electron-electron scattering [16] and grain boundary scattering [17].

In the case of a polycrystalline film, the conduction mechanism is dominated by the inherent inter-crystalline boundaries rather than the intra-crystalline characteristics. These boundaries generally contain fairly high densities of interface states that trap free carriers by virtue of the inherent disorders and the presence of trapped charges. The interface states results in a space charge region in the grain boundaries. Due to this space charge region, band bending occurs, resulting in potential barriers to charge transport.

1.2.4. Optical properties and plasma frequency

The optical properties of a transparent conducting film depend strongly on the deposition parameters, microstructure, level of impurities and growth techniques. Being transparent in the visible and NIR range and reflecting to IR radiations, they act as selective transmitting layer. The transmission spectrum of a TCO is given in figure 1.1 where in the x-axis; λ_{gap} represents the wavelength corresponding to the band gap and λ_p is the plasma wavelength.

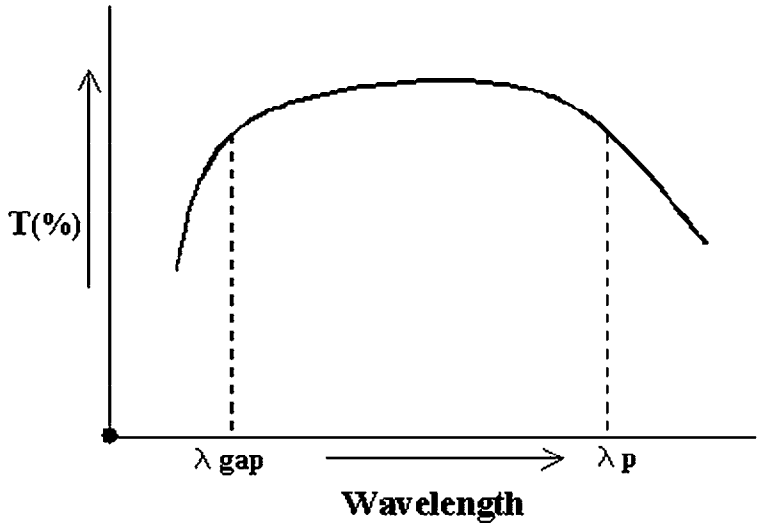

Figure 1.1. Transmission spectrum of TCO.

The transmission spectrum shows that for wavelengths longer than plasma wavelength the TCO reflects radiation while for shorter wavelengths TCO is transparent. At frequencies higher than the plasma frequency, the electrons cannot respond to the changing electric field of the incident radiation, and the material behaves as a transparent dielectric. At frequencies below the plasma frequency, the TCO reflects the incident radiation while at frequencies above the band gap of the material, the material absorbs the incident radiation. For most TCO materials, the plasma frequency falls in the near-infrared part of the spectrum, and the visible region is in the higher, transparent frequency range. The plasma frequency increases approximately with the square root of the conduction-electron concentration. The maximum obtainable electron concentration and the plasma frequency of TCOs generally increase in the same order as the resistivity [18].

1.2.5. Optical and electrical performance

TCOs have two important qualities with which they can be judged, optical transmission and electrical conductivity, and these two parameters are somewhat inversely related, a method of comparing the properties of these films is essential. Figure of merit have allowed researchers to compare the various results in a reasonable and direct manner. Researchers have developed different methods for finding the figures of merit of the films. One of the earliest equations defining a figure of merit was developed by Fraser and Cook [19] and is given by the relation $F_{FC} = \frac{T}{R_s}$ where T is the transmission and R_s is the sheet resistance of the thin film. This value was often multiplied by 1000 to allow comparisons of numbers greater than one. This definition depends on the film thickness.

Another definition for figure of merit, F_H, developed by Haacke [20] is also related to the above definition. However, F_H puts more emphasis on the optical transparency because F_{FC} was too much in favor of sheet resistance, resulting in a maximum figure of merit at relatively large film thicknesses. The figure of merit was redefined as $F_H = \frac{T_a^x}{R_s}$ where x>1. Haacke selected the value of x = 10. The definition by Haacke is also thickness dependent. The third definition for figure of merit was developed by Iles and Soclof [21]. A figure of merit that is independent of film thickness is given by $F_{1s} = R_s[1-T] = \frac{\alpha}{\sigma}$. By this definition, a lower value of figure of merit indicates films of better quality.

Most of the variation in the figure of merit of TCO is due to differences in mobility, but the free-electron concentration does not affect the figure of merit. The electron mobility is determined by the electron-scattering mechanisms that operate in the material. First of all, some scattering mechanisms, such as scattering of electrons by phonons, are present in pure single crystals. Practical TCO's need much higher doping levels and for these high doping levels, scattering by the ionised dopant atoms become another important mechanism that alone limits the mobility. This maximum mobility is lowered still further by other scattering mechanisms such as grain-boundary scattering, present in polycrystalline thin films. The best TCO films, ZnO:F and Cd_2SnO_4, have been prepared with mobilities in the range of 50–60 $cm^2 V^{-1} s^{-1}$ [22].

1.2.6. Work function and thermal stability

The work function of a TCO is defined as the minimum energy required to remove an electron from the fermi level to the vacuum level. ZnO has a work function of 4.57eV [23]. Generally TCOs will have an increase in resistivity if heated to a high enough temperature for a long enough time. TCOs remain stable to temperatures slightly above the optimised deposition temperature.

1.2.7. Minimum deposition temperature

The substrate temperature, during deposition of TCO thin films, must be at a sufficiently high in order to develop the required properties for the TCO. The required temperatures are usually found to increase in the following order: ITO<ZnO<SnO_2<Cd_2SnO_4 [6]. ITO is preferred for deposition on thermally sensitive substrates, such as plastic, while cadmium stannate requires highly refractory substrates to achieve its best properties.

1.2.8. Diffusion barriers between transparent conductors and sodium-containing glass substrates

When TCOs are deposited on sodium containing glass, such as soda-lime glass, sodium can diffuse into the TCO and increase its resistance. This effect is particularly noticeable for tin oxide, because sodium diffuses rapidly at the high substrate temperatures (often 550^0C) used for its deposition. It is common to deposit a barrier layer on the glass prior to the deposition of tin oxide. Silica or alumina is used commonly as the barrier layer between soda-lime glass and tin oxide.

1.2.9. Etching patterns in TCOs

For some applications of TCOs, such as displays, heaters, or antennas, parts of the TCO must be removed. Zinc oxide is the easiest material to etch, tin oxide is the most difficult, and indium oxide is intermediate in etching difficulty [6]. Series-connected thin-film solar cells need to remove TCOs along patterns of lines. This removal is usually carried out by laser ablation.

1.2.10. Chemical durability

The ability of a TCO to withstand corrosive chemical environments is inversely related to its ease of etching. Tin oxide is the most resistant TCO, while Zinc oxide is readily attacked by acids or bases.

1.2.11. Mechanical hardness

The mechanical durability of TCOs is related to the hardness of the crystals from which they are formed. Titanium nitride and tin oxide are even harder than glass and can be used in applications that have these coatings exposed. Zinc oxide is readily scratched, but can be handled with care. Thin silver films are so fragile that they cannot be touched and can be used only when coated with protective layers.

1.2.12. Production costs

The costs of producing a transparent conducting material depend on the cost of the raw materials and the processing of it into a thin layer. The cost of the raw materials generally increases in this order: Cd <Zn<Ti< Sn< Ag< In. The costs of the deposition methods typically increase in the following order: Atmospheric pressure CVD<Vacuum Evaporation <Magnetron Sputtering<Low-Pressure CVD < Sol-gel <Pulsed Laser Deposition <MBE <MOCVD. The speed of the process is also very important in determining the cost.

1.2.13. Toxicity

Some of the elements used in TCOs are toxic. This increases the cost of processing them because of the need to protect workers and prevent the escape of toxic materials into the environment [6]. Toxicity of the elements generally increases in as Zn<Sn<In<Ag<Cd. Cadmium compounds are carcinogens and thus are heavily regulated and even prohibited from being used for some applications.

1.2.14. Classification of TCOs

Ingram et al classifies TCO structurally into four main families [24] as given in table1.1. The first family has cations tetrahedrally coordinated by oxygen, and is *n*-type in character. ZnO is the only known oxide to possess this coordination exclusively. The second family has cations in octahedral coordination, and is also *n*-type in character. This is the largest family of TCOs, including CdO, In_2O_3, SnO_2, $CdIn_2O_4$, Cd_2SnO_4, and most of the best *n*-type complex oxide materials. The third family of TCOs has cations in linear coordination with oxygen, and is *p*-type in character. This family includes

$CuAlO_2$, related Cu- and Ag-based delafossites and $SrCu_2O_2$. Finally, the cage-structure oxide, $12CaO{\cdot}7Al_2O_3$, is listed as the first member of a potential new family of TCOs; it is *n*-type in character.

Table 1.1. Families of transparent conducting oxides.

Structural feature	**Carrier type**	**Examples**
Tetrahedrally-coordinated cations	*n*-type	ZnO
Octahedrally-coordinated cations	*n*-type	CdO, In_2O_3, SnO_2, Cd_2SnO_4, etc.
Linearly-coordinated cations	*p*-type	$CuAlO_2$, $SrCu_2O_2$, etc.
Cage framework	*n*-type	$12CaO{\cdot}7Al_2O_3$

1.3. n-type transparent conducting oxide

Present studies involves mainly the growth and characterization of heterojunction diodes with ZnO as n-type TCO and ZnO based nanostructures. A brief account of the ZnO and an outline of the previous work on ZnO as a TCO is presented in this section.

1.3.1. Zinc oxide (ZnO)

There has been a great deal of interest in zinc oxide (ZnO) semiconductor materials, as seen from the surge of a relevant number of publications. The interest in ZnO is fueled and fanned by its prospects in optoelectronics applications owing to its direct wide band gap (Eg~3.3 eV at 300 K). The unique optoelectronic properties of zinc oxide, the low cost and its non-

toxicity have attracted considerable interest over the last few years. The optical and electrical properties, high chemical and mechanical stability makes ZnO as one of the most promising material for TCO. The abundance of ZnO in nature makes it a low cost material than most of the currently used TCO's (SnO_2, ITO). The average amount of zinc available on earth's crust is 132 ppm while Indium is only 0.1 ppm and tin is 40 ppm. Zinc oxide occurs in nature as the mineral zincite. Zinc oxide crystallises in the hexagonal wurtzite (B 4-type) lattice. The zinc atoms are nearly in the position of hexagonal close packing. Every oxygen atom lies within a tetrahedral group of four zinc atoms.

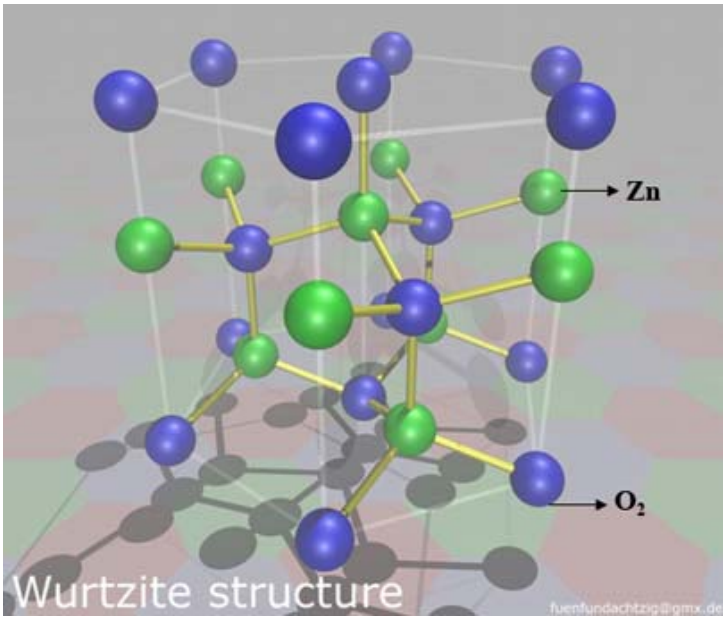

Figure 1.2. Wurtzite structure of ZnO.

The lattice constants are a = 3.24 A^o and c = 5.19 A^o [8].

All these tetrahedras point in the same direction along the hexagonal axis giving the crystal its polar symmetry. The wurtzite structure is shown in figure 1.2. Some optoelectronic applications of ZnO overlap with that of GaN, another wide-gap semiconductor (Eg~3.4 eV at 300 K) which is widely used for production of green, blue-ultraviolet, and white light-emitting devices. However, ZnO has some advantages over GaN among which are the availability of fairly high-quality ZnO bulk single crystals and a large exciton binding energy (60 meV). ZnO also has much simpler crystal-growth technology, resulting in a potentially lower cost for ZnO-based devices.

Good crystalline ZnO films can be grown at relatively low temperatures (less than 700°C). The large exciton binding energy of (60 meV) paves the way for an intense near-band-edge excitonic emission at room and higher temperatures, because this value is 2.4 times that of the room-temperature (RT) thermal energy (k_BT = 25 meV). There have also been a number of reports on laser emission from ZnO-based structures at RT and beyond. It should be noted that besides the above-mentioned properties of ZnO, there are additional properties which make it preferable over other wide-band-gap materials: its high energy radiation stability and amenability to wet chemical etching [25]. Several experiments confirmed that ZnO is very resistive to high-energy radiation, [26–28] making it a very suitable candidate for space applications. ZnO is easily etched in all acids and alkalis, and this provides an opportunity for fabrication of small-size devices. In addition, ZnO has the same crystal structure and close lattice parameters to that of GaN and as a result can be used as a substrate for epitaxial growth of GaN films [29, 30].

ZnO has recently found other niche applications as well, such as fabrication of transparent thin-film transistors [31], where the protective covering preventing light exposure is eliminated since ZnO-based transistors are insensitive to visible light. By controlling the doping level electrical properties can be changed from insulator through *n*-type semiconductor to metal while maintaining optical transparency that makes it useful for transparent electrodes for solar cells [32]. ZnO is also a promising candidate for spintronics applications [33]. Dietl *et al* [34] predicted a Curie temperature of > 300 K for Mn-doped ZnO.

However, one important problem should be overcome before ZnO could potentially make inroads into the world of optoelectronics devices: the growth of *p*-type-conducting ZnO crystals.

The origin of p type conductivity in zinc oxide has been controversial. From a first principles calculation, Yamamoto and Yoshida [35] proposed that ‘‘co-doping’’ of donor acceptor dopants (e.g. Ga and N, respectively) in ZnO might lead to p-type conduction. In this method the simultaneous doping of both acceptor (N) and donor (Ga) into the ZnO lattice were carried out with an acceptor concentration twice that of the donor concentration to get a maximum conductivity in p-ZnO. The essential approach of this method is to stabilize the N substitution in the appropriate ZnO lattice sites by the formation of N–Ga–N type bonds, which reduce the N–N repulsive interaction (Madelung Energy) thereby making the acceptor level shallower, thus enhancing the acceptor doping. Successful p type doping of ZnO was first demonstrated by Joseph et al. [36] with a room temperature resistivity of 0.5 Ω cm and a carrier concentration

of 5 x 10^{19} cm^3 in p-type ZnO thin films deposited on glass substrate with Ga and N as dopants.

Thin films grown by spray pyrolysis of nitrogen doped p type ZnO have a carrier concentration of 10^{18} cm^3 and resistivity of 10^{-2} Ω cm [37]. The low density of compensative native defects as well as the hydrogen passivation in the ZnO:N film grown by ultrasonic spray pyrolysis (USP) probably account for the good p type conduction. The high hole mobility may be due to the nanocrystal structure of ZnO based films grown by ultrasonic spray pyrolysis. The photoluminescence spectrum exhibits a strong near-band-edge emission and a very weak deep-level emission in both undoped and N-doped ZnO films, indicating that the ZnO-based films grown by the USP technique are very close to stoichiometry and of optically high quality.

p-type conductivity of intrinsic ZnO thin films deposited by plasma-assisted metal-organic chemical vapor deposition with a hole concentration above 10^{17} cm^{-3} was achieved at the growth temperatures of 250 and 300 °C. It is speculated that the oxygen chemical potential is enhanced by virtue of oxygen plasma, which can lower the formation energy of some acceptor defect, such as zinc vacancy, and this accounts for the p-type conductivity. Increasing the growth temperature to 350 and 400 °C results in n-type conductivity with an electron concentration around 10^{17} cm^{-3}. The inversion to n-type conductivity can be explained as the compensation effect by the ionized oxygen vacancy donor, which is readily formed at high growth temperatures. The *p*-type behavior is temperature dependent. The origin of intrinsic p-type behavior has been ascribed to the formation of zinc vacancy and some complex acceptor center. Understanding of these intrinsic acceptor states will help to elucidate the

extrinsic as well as intrinsic p-type doping mechanism in ZnO [38]. The films grown at optimum conditions show a resistivity of 12.7 Ω cm and a hole concentration of 1.88 x 10^{17} cm^{-3}.

Arsenic doped ZnO thin films show p type conductivity. ZnO: As films grown on O – face of ZnO substrates and Si – face of SiC show p type conductivity with a carrier concentration of 9 x 10^{16} cm^{-3} and mobility of 6 cm^2/Vs. is obtained with resistivity of 12 Ω cm for thin films. The PL emission at 3.359 eV is attributed to acceptor bound exciton emission and the PL emission at 3.322 eV and 3.273 eV is attributed to recombination emissions between free electrons and acceptor holes. The donor to acceptor recombinations result in PL emissions at 3.219 eV and 3.172 eV. [39].

1.4. p-type transparent conducting oxides

$AgCoO_2$ have been used as the p-type layer in the all transparent p-n heterojunction fabricated in the present studies. A brief account of delafossites has been reviewed in this section.

NiO thin film was the first reported p-TCO with a moderate 40% transparency in the visible region and a high 7.0 Scm^{-1} room-temperature conductivity [40]. The bandgap of NiO single crystal is between 3.6 and 4.0 eV [41]. Nickel vacancies as well as excess oxygen in interstitial sites are responsible for enhanced p-type conductivity of the material [42]. The p type TCOs reported so far generally have less conductivity than that reported for n type TCOs. The large electronegativity of oxygen could be producing a strong localization of the valance band edge of oxides thereby producing a deep trap where positive holes are localised [43]. These holes cannot migrate even under

an applied field. Thus efforts should be made to modulate or modify the energy band structure to reduce the localisation of the valance band edge so as to increase the mobility of the holes. Cu_2O and Ag_2O show p type conductivity. However their low band gap (~ 2eV) make it impossible to use them as transparent conductors. Analysing the structure of these compounds show linear coordination of two oxygen ions to Cu^+ ions this could be an indication of the fact that the $3d^{10}$electrons of Cu^+ have comparable energy with O $2p^6$ electrons. This could be reducing the localization effects of the traps produced at the valance band edge. But the three dimensional interaction of Cu^+ ions should be expanding the band edge effectively reducing the band gap. Thus if the Cu^+ interactions could be reduced while the linear coordination with two oxygen atoms be retained in any crystal structure, this would produce p type transparent conductors.

Owing to the strong ionic nature of metal-oxygen bonding, holes are typically localized at the valence band edge, which is dominated by oxygen-2p levels therefore limiting p-type conduction. Two methods have been suggested to enhance the covalency between metal oxygen bonding, thereby limiting localization. Choosing cations having closed d-shells of energy comparable to that of the oxygen-2p levels (i.e., Cu^+, Ag^+, and Au^+, especially when found in linear coordination with oxygen [69]), and choosing a structure in which oxygen adopts tetrahedral coordination. An aggressive search for a viable p-type TCO was motivated by the report of Kawazoe et al. [44] on the optical and electrical properties of copper aluminate ($CuAlO_2$) thin films prepared by laser ablation. $CuAlO_2$, which crystallizes in the delafossite structure having the general formula $A^{1+}B^{3+}O^{2-}$ show p-type conduction. The delafossite structure comprises

of alternating layers of slightly distorted edge-shared BO_6 octahedral and two-dimensional close-packed A-cation planes forming linear O–A^{1+}–O "dumbbells" [45] as found in the well-known p-type oxide semiconductor Cu_2O [46]. The delafossite structure is shown in figure 1.3. Furthermore, the oxygen atoms are coordinated by four cations (one A^{+1} and three B^{3+}). Depending on the stacking of the layers, two polytypes are possible.

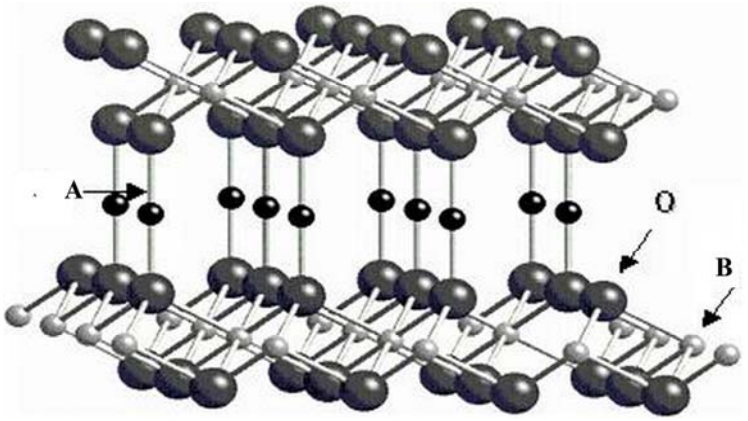

Figure 1.3 Delafossite structure

The "3R" polytype consists of "AaBbCcAaBbCc..." stacking along the *c*-axis and has rhombohedral symmetry with the space group $R\bar{3}m$ (No. 166), whereas the "2H" polytype consists of an alternate stacking sequence ("AaBbAaBb...") and has the space group *P*63/*mmc* (No. 194) [47].

$CuYO_2$ is p-type semiconductor having wide bandgap isostructural with $CuAO_2$ delafossite (where A= Fe, Co, Rh, Ga,Sc,Y or lanthanides) [48]. Intercalation with oxygen to form $CuAO_{2+\delta}$ phases is possible for compounds with large A^{3+} cations. Cava et al [49, 50] have investigated the properties of

polycrystalline $CuYO_{2+\delta}$ and $CuLaO_{2+\delta}$ phases. The $CuYO_{2+\delta}$ doped with calcium show conductivity as high as 10 Scm^{-1} after the oxygen intercalation. Similar observation of increase in conductivity has been reported for $CuScMgO_{2+\delta}$ films on oxygen intercalation [51]. But the oxygen intercalation results in reduced transmittance in these films.

$CuAlO_2$ was the first prepared in the thin film form by Kawazoe [69]. Many materials including $CuGaO_2$ [48, 52], $CuScO_2$ [52] and $CuYO_2$ [52] were also prepared in the bulk form all these materials show low conductivity (< 10^{-1} S cm^{-1}) and have low transmittance in the visible range. (≈ 50%). Doped copper delafossites like $CuGaO_2$:Fe, $CuInO_2$:Ca, $CuYO_2$:Ca, $CuFe_{1-x}V_xO_2$ etc also show low conductivity and transmittance [53, 54]. Silver based delafossites are difficult to synthesis by solid state reactions. They are not as stable as the Cu based delafossites. Thin films of $AgInO_2$ showed n type conductivity. Magnesium doping in bulk $AgInO_2$ leads to p type conduction. Very low conductivity is observed for these powders. The other silver based delafossites reported are also low conducting. They include $AgCrO_2$, $AgScO_2$, and $AgGaO_2$. p type conductivity of 2 x 10^{-1} S cm^{-1} and transparency of 50% in the visible is obtained for thin films of $AgCoO_2$ [53]. $AgGaO_2$ thin films shows a transparency of 50% in the visible with p-type electrical conductivity 3.2 x 10^{-4} Scm^{-1} [55]. The cause of p type conductivity in these materials is due to excess oxygen (or metal deficit) in the crystallite sites. Changing the preparation conditions of the materials result in deviation of composition from stoichiometry in these materials. Thin film preparation of silver based delafossite compounds is a challenging task due to the instability of the silver compounds. The Cu – 3d character of the valance band edge of the copper based delafossite have an edge

over the O – 2p character of the valance band edge of silver based delafossites. Since the d mainfold holes are more mobile than the p mainfold holes [56].

The development of p type transparent oxide materials has lead to the fabrication of all oxide diodes and transistors. The progress achieved in the field of semiconductor oxide diodes and transistors has paved way for newer applications for transparent conductors and a new field of electronics called transparent electronics has been defined.

1.5. Introduction to nanotechnology

Nanotechnology is known as the technology of the 21st century which deals with the synthesis and study of ultra fine materials and their employment in technology for various applications. It can be defined as the synthesis and engineering at the molecular level for possible device applications where nanoscience deals with the investigations of phenomena and properties exhibited by materials at the nano level.

Enhanced luminescence efficiency at the nano level enlightened the area of fluorescent probes in biomedical applications. The idea of nanoscale molecular device is not entirely new, and has been around since days immemorial, Richard Feynmann, who said in 1960 “there is plenty of room at the bottom”. Materials consisting of particles with diameter less than 100 nm have attracted a great deal of recent research attention. Owing to their ultrafineness in size and very high surface area, these particles possess dramatic changes in physical and chemical properties as compared to their bulk counterparts which makes them ideal templates to study the physics at the nanolevel from a fundamental point of view in addition to the vast application

potential in versatile fields [57, 58]. Nanoparticles behave quite different from their coarser-grained counterparts of the same composition due to the high surface to volume ratio. The more loosely bound surface atoms constitute a significant fraction of the sample and their properties influence its behaviour. For example, the melting point of gold is dramatically reduced when the particle diameter drops below 5 nm. Improvements can be made in the mechanical and fluorescent properties of materials.

Optical properties are modified because of the quantum size effects on the band structure. Optical energy band gap is blue shifted for ultra fine materials. Nano sized gold is green in colour which is a semiconductor while bulk is a noble yellow metal!. We can make junctions with the same materials with different grain sizes due to the modified band structures of these ultra fine particles. This gives scope for a variety of applications in the semiconductor industry.

1.5.1. Size quantization effects in the nanoregime

Quantization in ultra fine particles originates from the confinement of charge carriers in semiconductors with potential wells of narrow dimensions less than the de-Broglie wavelength of electron and holes. Confinements could be mere electronic, excitonic or polaronic based on the grain size and excitation energy [59]. Under these conditions, the energy bands of electrons and holes becomes close to discrete energy levels as of in atom and thus a semiconductor becomes atom like. In addition to the large change in electronic/optical properties, they also exhibit change in the effective redox potentials of photo-generated carriers. Size quantization effects on the optical properties of semiconductors are extensively studied [60-64]. In CdS nanocrystals, a blue shift

in energy band gap of 1.54 eV is obtained for a particle with radius 1nm. Blue shift in band gap is observed for many other semiconductors also because of the quantum confinement effects.

1.5.2. Optical properties

Optical properties of ultra fine particles are profoundly modified by the grain size dependant confinement effects. In the ultra fine regime, due to very small wave function overlapping, the energy levels tends to be discrete and when the grain sizes are reduced to the order of exciton Bohr radius limit of the material, they are near molecule like materials and hence the energy levels tend to be discrete and thus there is confinement of carriers. This will alter the band gap towards the high energy limits. Thus by manipulating grain sizes, materials with same chemical formulae but different band gaps can be synthesized. The influence of grain size vis a vis quantum confinement have been investigated extensively [65-67].

1.6. Introduction to various nanostructures

Brief description of different nanostructures such as quantum dot, quantum well and nano wire is included in this section.

1.6.1. Quantum dot

A quantum dot is a semiconductor nanostructure that confines the motion of conduction band electrons, valence band holes or excitons (pairs of conduction band electrons and valence band holes) in all three spatial directions [68]. The confinement can be due to electrostatic potentials (generated by external electrodes, doping, strain, impurities) and the presence of an interface between different semiconductor materials (e.g. in the case of self-assembled

quantum dots). This can also be due to the presence of the semiconductor surface (e.g. in the case of a semiconductor nanocrystal). A quantum dot has a discrete quantized energy spectrum [69]. The corresponding wave functions are spatially localized within the quantum dot, but extend over many periods of the crystal lattice. A quantum dot contains a small finite number (of the order of 1-100) of conduction band electrons, valence band holes, or excitons, i.e., a finite number of elementary electric charges

Small quantum dots, such as colloidal semiconductor nanocrystals, can be as small as 2 to 10 nanometers, corresponding to 10 to 50 atoms in diameter and a total of 100 to 100,000 atoms within the quantum dot volume [68]. Quantum dots can be contrasted to other semiconductor nanostructures [70]: 1) quantum wires, which confine the motion of electrons or holes in two spatial directions and allow free propagation in the third. 2) Quantum wells, which confine the motion of electrons or holes in one direction and allow free propagation in two directions. Optical properties like luminescent intensity and emission wavelength can be tuned by controlling the size of the semiconductor quantum dots. For example silver at a particular size in the nano level behaves like an insulator instead of very good conductor. Brus established a relation between band gap and particle size, demonstrating that band gap decreases with increase of particle size [71].

1.6.2. Quantum well

A quantum well is a potential well that confines particles, which were originally free to move in three dimensions, to two dimensions, forcing them to occupy a planar region. The effects of quantum confinement take place when the quantum well thickness becomes comparable at the de Broglie wavelength of the

carriers [72,73] (generally electrons and holes), leading to energy levels called "energy subbands", i.e., the carriers can only have discrete energy values [68].

Quantum wells are formed in semiconductors by having a material with low band gap, like gallium arsenide sandwiched between two layers of a material with a wider band gap, like aluminium arsenide. These structures can be grown by molecular beam epitaxy or chemical vapor deposition with control of the layer thickness down to monolayer [74]. Confinement of carrier in one dimension changed the density of states in such a way that, both the luminescent efficiency and energy of luminescence emission will be enhanced. Because of their quasi-two dimensional nature, electrons in quantum wells have a sharper density of states than bulk materials. As a result quantum wells are in wide use in diode lasers [68]. They are also used to make HETMs (high electron mobility transistors), which are used in low-noise electronics. Quantum well infrared photo detectors are also based on quantum wells, and are used for infrared imaging.

1.6.3. Nano wire (Nanorod)

In nano wires, two of the dimensions are cut off. Materials could be made into the nanowires in which one of the degrees of freedom is retained for the charge carriers electrons and holes. Hence the diameter of the nanorod is few tens of nanometers. Hence confinement is stronger as there is only one degree of freedom. A nano wire or nanorod is an electrically conducting wire, in which quantum effects are affecting transport properties. Due to the confinement of conduction electrons in the transverse direction of the wire, their transverse energy is quantized into a series of discrete values E_0, E_1 etc [68, 70]. It is

possible to make quantum wires out of metallic carbon nanotubes, atleast in limited quantities [70].

Among the known one-dimensional (1D) nanomaterials, ZnO has three key advantages. First, it exhibits both semiconducting and piezoelectric (PZ) properties that can form the basis for electromechanically coupled sensors and transducers. Second, ZnO is relatively biosafe and biocompatible [75], and it can be used for biomedical applications with little toxicity. Finally, ZnO exhibits the most diverse and abundant configurations of nanostructures known so far, such as nano wires [76], nanobelts (NBs) [77], nanosprings [78], nanorings [79], nanobows [80], and nanohelices [81].

1.7. ZnO based nanostructures

Pulsed laser ablation has been employed in the present work for the growth of various ZnO based nanostructures like quantum dots, nanorods and quantum wells. This section includes a short review of the previous work on quantum dots, nanorods and quantum wells.

1.7.1. Quantum dots

Synthesis of nanoparticles has been a focus of an ever-increasing number of researchers world wide, mainly due to their unique optical and electronic properties [82-85] which makes them ideal for a wide spectrum of applications ranging from flexible displays [86], lasers [87, 88] to *in vivo* biological imaging and therapeutic agents [89]. Quantum dots based on CdSe [90], CdTe [91] or CdSe/ZnS core/shell [92] materials are one of the most studied colloidal systems due to their excellent, size tunable light emitting properties. However, recently cyto toxicity studies revealed that these quantum

dots are acutely cyto toxic due to the liberation of free radicals of Cd^{+} and Se^{-} into the blood stream. These findings may limit the application potential of cadmium or selenium containing quantum dots, particularly for biological applications. ZnO being biocompatible and posses strong emission bands in the UV [93] and visible (green [94], blue [95] and violet [96] regions), nanostructured ZnO have attracted the attention of the researchers world wide. The UV peak was usually considered as the characteristic emission of ZnO and attributed to the band edge emission or the exciton transition. Reports on blue [95] and violet [96] PL in ZnO are scarcely available. Liquid phase pulsed laser ablation (LP-PLA) technique has been recently evolved to be potential method for the synthesis of nanoparticles [97, 98]. In the present studies, surfactant free ZnO nanoparticles have been prepared using LP-PLA technique.

1.7.2. Nanorods

ZnO nanostructures have been paid much more attention due to their room-temperature UV lasing properties. Especially, the synthesis of one dimensional (1-D) ZnO nanostructures has been of growing interest owing to the promising application in photonic devices, UV lasers, sensors, etc. So far, various methods, including chemical vapor deposition (CVD) [99], chemical vapour transport and condensation (CVTC) [100], thermal evaporation [101], hydrothermal methods [102], metal organic chemical vapor deposition [103], soft solution route [104], and template assisted [105], have been developed to grow 1-D ZnO nanostructures. Vapor liquid-solid [106] and vapor-solid [107] mechanisms are commonly employed to explain the growth process. Pulsed laser deposition (PLD) is recognized as an important method for synthesizing ZnO nanorods with excellent electronic and optical properties [108]. Room

temperature growth of luminescent ZnO nanorods using PLD is demonstrated in the present thesis work.

1.7.3. Quantum well

Stimulated emission has been observed in quantum well structures utilizing the alloys of ZnO. It is expected that the observation of the excitonic stimulated emission phenomenon should be favored in quantum wells owing to the enhanced binding energy of excitons and hence by the larger stability of the exciton states. However, in other II-VI materials stimulated emission has been mostly demonstrated only at low temperatures and rarely at room temperature. But, the excitons in ZnO-based quantum well (QW) heterostructures exhibit strong stability as compared to bulk semiconductors or III–V QWs due to the enhancement of the binding energy [109, 110] and the reduction of the exciton–phonon coupling [111] caused by quantum confinement. Due to these effects, excitons are expected to play an important role in many-body processes such as laser action and nonlinear absorption of II–VI-oxide QWs even at room temperature. For example, excitonic gain has been demonstrated in ZnO/ZnMgO QWs. A detailed study of excitons in ZnO multiple quantum wells (MQWs) is thus important for understanding the optical properties of these wide gap heterostructures, especially in view of their application to ultraviolet–blue optoelectronic devices [112]. In addition, the effect of built-in electric fields inside QW layers might be taken into account for ZnO QWs having a relatively high barrier height. Misra *etal* [113] reported the growth of ZnMgO/ZnO quantum well using PLD at higher temperature. They also presented room temperature luminescence from this quantum well. Present studies includes the

low temperature fabrication ZnMgO/ZnO quantum well giving room temperature luminescence.

1.8. **Conclusion**

TCO's have been discussed in this chapter both from the point of view of theoretical perspective and addressing the previous reports. Various p-type TCO's reported till date have been presented. ZnO has been paid more attention, since ZnO is the core material in the present work. P-type TCO's are generally less transparent compared to ZnO and posses low mobility. It would be sensible to work towards the goal of improving the mobility and transparency of p-type TCO's. The application potential of ZnO is much more driving inroads with the expense of nanotechnology.

1.9. References

1 T. J. Coutts, T. O. Mason, J. D. Perkins and D. S. Ginley, NREL/CP **520** (1999).

2 D. J. Griffits, *Introduction to Electrodynamics*, 3rd Edn, Prentice – Hall of India Pvt. Ltd, New Delhi. (2002).

3 I. Hamberg and C.G. Granqvist, J. Appl. Phys. **60** (1986) R123.

4 J. Hu and R. G. Gordon, J Appl. Phys. **71** (1992) 880.

5 I. Hamberg, A. Hjortsberg, and C. G. Granqvist, Appl. Phys. Lett. **40** (1982) 362.

6 R. G. Gordon, Proc. Of MRS workshop "*Transparent conducting oxides (TCOs)*" August **25** (2000) 5.

7 K. L. Chopra, S. Major and D. K. Pandya, Thin Solid Films **102** (1983) 1.

8 E. Shanthi, V. Dutta, A. Banerjee, and K. L. Chopra, J. Appl. Phys. **51** (1980) 6243.

9 A .De and S. Ray, J. Phys. D: Appl.Phys. **24** (1991) 719.

10 H.L. Hartnagel, A.L. Dawar, A.K.Jain and C. Jagadish, *Semiconducting transparent thin films*, IOP publishers, Bristol (1995).

11 J. Bardeen and W. Shockley, Phys. Rev. **80** (1950) 72.

12 A. R. Huston, J. Appl. Phys. **32** (1961) 2287.

13 H. Ehrenreich, J. Appl. Phys. **32** (1961) 2155.

14 C. Erginsoy, Phys. Rev. **79** (1950) 1013.

15 V. A. Johnson, and K. Lark–Horovitz, Phys. Rev. **71** (1947) 374.

16 J. Appel, Phys. Rev. **122** (1961) 1760.

17 R. L Petritz, Phys. Rev. **104** (1956) 1508.

18 T. J.Coutts, D. L. Young and L. Xiaonan, MRS Bull. **8** (2000) 58.

19 D. B. Fraser and H. D. Cook, J. Electrochem. Soc. **119** (1972) 1368.

20 G. Haacke, Appl. Phys. **47** (1976) 4086.

21 P. A. Iles and S. I. Soclof, I. E. E. Photovoltaic Specialists Conference, (1976) 978.

22 T. X. Li, T. Gessert, C. DeHart, T. Barnes, H. Moutinho, Y. Yan, D. Young, M. Young, J. Perkins, and T. Coutts, NREL/CP-520-31017 (2001).

23 R. L. Hoffmann, *Development, Fabrication and Characterization of Transparent Electronic Devices*, Master of Sciences Thesis, Oregon State University (1992).

24 B. J. Ingram, G.B. Gonzalez, D.R. Kammler, M.I. Bertoni and T.O. Mason, Journal of Electroceramics, **13** (2004) 167.

25 D. C. Look, Mater. Sci. Eng., B **80** (2001) 381.

26 D. C. Look, D. C. Reynolds, J. W. Hemski, R. L. Jones, and J. R. Sizelove, Appl. Phys. Lett. **75** (1999) 811.

27 A. Y. Polyakov, N. B. Smirnov, A. V. Govorkov, E. A. Kozhukova, V. I. Vdovin, K. Ip, M. E. Overberg, Y. W. Heo, D. P. Norton and S. J. Pearton, J. Appl. Phys. **94** (2003) 2895.

28 S. O. Kucheyev, J. S. Williams, C. Jagadish, J. Zou, C. E X. Gu, M. A. Reshchikov, A. Teke, D. Johnstone, H. Morkoc, B. Nemeth, and J. Nause, Appl. Phys. Lett. **84** (2004) 2268.

29 B. M. Ataev, W. V. Lundin, V. V. Mamedov, A. M. Bagamadova and E. E. Zavorin, J. Phys: Condens Matter **13** (2001) 211.

30 F. Hamdani, M. Yeadon and D. J. Smith, J. Appl. Phys. **83** (1998) 983.

31 R. L. Hoffman, B. J. Norris and J. F. Wager, Appl. Phys. Lett. **82** (2003) 733.

32 L. Stolt, J. Hedstrom, J. Kessler, M. Ruckh, K. O. Velthaus, and H. W. Schock, Appl. Phys. Lett. **62** (1992) 597.

33 K. Sato and H. K Yoshida, Semicond. Sci. Technol. **17** (2002) 367.

34 T. Dietl, H. Ohno, F. Matsukura, J. Cibert, and D. Ferrand, Science **287** (2000) 1019.

35 T. Yamamoto and H.K. Yoshida, Jpn. J. Appl. Phys. **38** (1999) L166.

36 M. Joseph, H. Tabata and T. Kawai, Jpn. J. Appl. Phys. **38** (1999) L1205.

37 J. L. Zhao, X. M. Li, J. M. Bian, W. D. Yun and C. Y. Zhang, Journal of Crystal Growth **280** (2005) 495.

38 Y. J. Zeng, Z. Z. Ye, W. Z. Xu, J. G. Lu, H. P. He, L. P. Zhu, B. H. Zhao, Y. Che and S. B. Zhang, Appl. Phys. Lett **88** (2006) 262103

39 Y. R. Ryu, T. S. Lee and H. W. White, Appl. Phys. Lett. **83** (2003) 87.

40 H. Sato, T. Minami, S. Takata and T. Yamada, Thin Solid Films **236** (1993) 27.

41 D. Adler and J. Feinleib, Phys. Rev. B **2** (1970) 3112.

42 E. Antolini, J. Mater. Sci. **27** (1992) 3335.

43 H. Yanagi, *Transparent p/n type oxide semiconductors with delafossite structure: Chemical design and material exploration.* PhD Thesis, Tokyo Institute of Technology, Japan, (2001).

44 H. Kawazoe, M. Yasukawa, H. Hyodo, M. Kurita, H. Yanagi and H. Hosono, Nature **389** (1997) 939.

45 H. Kawazoe, H. Yanagi, K. Ueda, and H. Hosono, MRS Bulletin **25** (2000) 28.

46 L. Kleinman and K. Mednick, Phys. Rev. B **21** (1980) 1549.

47 K. Ueda, S. Inoue, H. Hosono, N. Sarukura and M. Hirano, Appl. Phys. Lett. **78** (2001) 2333.

48 R. D. Shannon, D. B. Rogers, and C.T. Prewitt, Inorg Chem **10** (1971) 713.

49 R. J. Cava, H. W. Zandbergen, A. P. Ramierz, H. Takagi, C. T. Chen, J. J. Krajewski, W. F. Peck.jr, J. V. Waszczak, G. Meigs, R. S. Roth, and L. F. Schneemeyer, J. Solid State Chem. **104** (1993) 437.

50 R. J. Cava, W. F. Peck.jr, J. J. Krajewski, S. W. Chenog, and H. Y. Hwang, J. Mater Res **9** (1994) 314.

51 H. Yanagi, S. Park, A. D. Draeseke, D. A. Keszler and J. Tate, J. Solid State Chem. **175** (2003) 34.

52 B. U. Kohler and M. Z. Jansen, Anorg Allg Chem, **543** (1986) 73

53 J. Tate, M. K. Jayaraj, A. D. Draeseke, T. Ulbrich, A. W. Sleight, K. A. Vanaja, R. Nagarajan, J. F. Wager and R. L. Hoffman, Thin solid films, **411** (2002) 119.

54 R. Nagarajan, N. Duan, M. K. Jayaraj, J. Li, K. A. Vanaja, A. Yokochi, A. Draeseke, J. Tate and A. W. Sleight, International Journal of Inorganic Materials, **3** (2001) 265.

55 A. Vanaja, R. S. Ajimsha, A. S Asha and M. K. Jayaraj, Appl. Phys Lett. **88** (2006) 212103.

56 A. Banerjee and K. K. Chattopadhyay, Progress in Crystal Growth and Characterisation of materials. **50** (2005) 52.

57 Masashige, Shinkai, M. Yanase, M. Suzuki, Hiroyuki, Honda, T. Wakabayashi, J. Yoshida and T. Kobayashi, J. Magn. Magn. Mater. **194** (1999) 176.

58 U. O. Hafeli and G. J. Pauer, J. Magn. Magn. Mater. **194** (1999) 76.

59 K. E. Gonsalves, S. P. Rangarajan and J. Wang edited by Hari Singh Nalwa, *Nanostructured Materials and Nanotechnology*, Academic Press (2002).

60 A. Henglein, Chem Rev **89** (1989) 1861.

61 H. Weller, H. M Schmidt, U. Koch, A. Fojtik, S. Baral, A Henglein, W. Kunath and K. Weiss, E. Diemen, Chem. Phys. Lett, **124** (1986) 557.

62 H Weller, Adv.Mater, **5,** (1993) 88.

63 D Heyes, O.I Micic, T Nenadovic, V Swayambhunathan and D Miesel, J. Phys. Chem, **93** (1989) 4603.

64 C.H Fischer and A. Henglein, J. Phys. **93** (1989) 5578.

65 C. Allan, M. Delerue and M. Lannoo, Appl. Phys. Lett, **70** (1997) 2437.

66 M. Goryll, L Vescan, K. Schmidt, S. Mesters, H. Luth, and K Szot, Appl. Phys.Lett, **71** (1997) 410.

67 G. Allan, C. Delerue and M. Lannoo, Appl. Phys. Lett, **71** (1997) 1189.

68 V. V. Mitin, V. A. Kochelap and M. A. Stronscio, *Quantum Heterostructures*, Cambridge University Press, Cambridge (1999).

69 J. H. Davies, *The Physics of Low-Dimensional Semiconductors*, Cambridge University Press, Cambridge (1998).

70 P. Harrison, Quantum Wells, Wires and Dots, John Wiley, New York (2000).

71 L. Brus J. Phys. Chem. **90** (1986) 2555.

72 C. Delerue and M. Lanno, Nanostructures, Springer, New-Delhi (2004).

73 S. V. Gaponenko, *Optical properties of semiconductor nanocrystals, Cambridge Press*, Cambridge (1998)

74 A. Shik, *Quantum Wells*, World Scientific, Singapore (1999).

75 G. Thomas, *Chemistry for Pharmacy and Life Sciences: Including Pharmacology and Biomedical Science*, Pentice-Hall, Englewoods Cliffs, NJ (1996).

76 M. H. Huang, Y. Wu, H. Feick, N, Tran, E. Weber and P. Yang, Adv. Mater. **13** (2001)113.

77 Z. W. Pan, Z. R. Dai and Z. L. Wang, Science **291** (2001)1947.

78 X. Y. Kong and Z. L. Wang, Nano Lett. **3** (2003)1625.

79 X. Y. Kong, Y. Ding, R. Yang and Z. L. Wang, Science **303** (2004) 1348.

80 W. L. Hughes and Z. L. Wang, J. Am. Chem. Soc. **126** (2004) 6703.

81 P. X. Gao, Y. Ding, W. Mai, W. L. Haghes, C. Lao and Z. L. Wang Science **309** (2005) 1700.

82 Y. Wu and P. Yang, Chem. Mater. **12** (2000) 605.

83 A. M. Morales and C. M. Lieber, Science **279** (1998) 208.

84 W. S. Shi, Y. F. Zheng, N. Wang, C. S. Lee and S. T. Lee, J. Vac, Sci.Technol.B **19** (2001) 115.

85 M. H. Huang, S. Mao, H. Feick, H.Yan, Y. Wu, H. Kind, E. Weber, R. Russo and P.Yang, Science, **292** (2001) 1897.

86 K. Manzoor, S. R. Vadera and N. Kumar Appl. Phys. Lett. **84** (2004) 284.

87 J. T. Andrews, P. Sen, J. Appl. Phys. **91** (2002) 2827.

88 L. V. Asryana, M. Grundmann, N. N. Ledentsov, O. Stier and D. Bimberg, J. Appl. Phys, **90** (2001) 1666.

89 X. Gao, Y. Cui, R. M. Levenson, L. W. K.Chung and S. Nie, Nature Biotechnology **22** (2004) 969.

90 M. Gao, B. Richter, S. Kirstein, and H. Mohwald, J. Phys. Chem. B **102** (1998) 4103.

91 N. P. Gaponik, D. V. Talapin and A. L. Rogach, Phys. Chem. Chem. Phys. **1** (1999) 1787 .

92 P. Palinginis and H. Wing, Proceedings of Quantum Electronics and Laser Science Conference (2001) , QELS '01, pp 3.

93 E. M. Wong and P. C. Searson, Appl. Phys. Lett. **74** (1999) 2939.

94 F. K. Shan, G. X. Liu, W. J. Lee, G. H. Lee, I. S. Kim, and B. C. Shin, Appl. Phys. Lett. **86** (2005) 221910.

95 J. J. Wu and S. C. Liu, Adv. Mater. (Weinheim, Germany) **14** (2002) 215.

96 Q. P. Wang, D. H. Zhang, Z. Y. Xue, and X. T. Hao, Appl. Surf. Sci. **201** (2002) 123.

97 W. T. Nichols, T. Sasaki and N. Koshizaki, J. Appl. Phys. **100** (2006) 114913.

98 R. M. Tilaki, A. Iraji zad and S. M. Mahdavi, Journal of Nanoparticle Research **9,** (2007) 853.

99 Z.X. Zhang, J.X. Wang, H.J. Yuan, Y. Gao, D.F. Liu, L. Song, Y.J. Xiang, X.W. Zhao, L.F. Liu, S.D. Luo, X.Y. Dou, S.C. Mou, W.Y. Zhou and S.S. Xie, J. Phys. Chem. B **109** (2005) 18352.

100 Y. Wu, H. Kind, E. Weber, R. Russo and P. Yang, Science **292** (2001) 1897.

101 H. T. Ng, J. Li, M. K. Smith, P. Nguyen, A. Cassell, J. Han and M. Meyyappan, Science **300** (2003) 1249.

102 S. J. Henley, M. N. R. Ashfold, D. P. Nicholls, P. Wheatley and D. E. Cherns, Appl. Phys. A **79** (2004) 1169

103 B. P. Zhang, N. T. Binh, Y. Segawa, K. Wakatsuki and N. Usami, Appl. Phys. Lett. **83** (2003) 1635.

104 J. H. Choy, E. S. Jiang, J. H. Won, J. H. Chung, D. J. Jang and Y. W. Kim, Adv. Mater. **15** (2003) 1911.

105 Y. Li, G. W. Meng, L. D. Zhang and F. Pillipp, Appl. Phys. Lett. **76** (2000) 2011.

106 A. M. Morales and C. M. Lieber, Science **279** (1998) 208.

107 P. M. Gao, Y. Ding, W. J. Mai, W. L. Hughes, C. S. Lao and Z. L. Wang, Science **309** (2005) 1700.

108 Y. Zhang, R. E. Russo and S. S. Mao, Appl. Phys. Lett. **87** (2005) 043106.

109 H. D. Sun, T. Makino, N. T. Tuan, Y. Segawa, Z. K. Tang, G. K. L. Wong, M. Kawasaki, A. Ohtomo, K. Tamura and H. Koinuma, Appl. Phys. Lett. **77 (**2000) 4250.

110 H. D. Sun, T. Makino, Y. Segawa, M. Kawasaki, A. Ohtomo, K. Tamura and H. Koinuma, J. Appl. Phys. **91 (**2002) 1993.

111 H. D. Sun, T. Makino, N. T. Tuan, Y. Segawa, M. Kawasaki, A. Ohtomo, K. Tamura and H. Koinuma, Appl. Phys. Lett. **78 (**2001) 2464.

112 T. Makino, N. T. Tuan, H. D. Sun, C. H. Chia, Y. Segawa, M. Kawasaki, A. Ohtomo, K.Tamura and H. Koinuma, Appl. Phys. Lett. **77** (2000) 975.

113 P. Misra, T. K. Sharma, S. Porwal and L. M. Kukreja, Appl. Phys. Lett. **89** (2006) 161912.

Chapter 2

Experimental techniques and characterization tools

This chapter presents the various deposition techniques used for the growth of transparent conducting oxide thin films. This chapter also describes the various characterization tools employed for analyzing the films.

2.1. Thin film preparation techniques

Properties of various materials in the bulk form were found to be highly useful in transparent electronics. But the application in optoelectronics devices demands these materials in thin film form retaining the interesting properties of the bulk material. In order to satisfy these requirements, various thin film preparation techniques were employed by the researchers. Thin film properties are strongly dependent on the methods of deposition, the substrate materials, the substrate temperature, the rate of deposition and the background pressure. The application and the properties of the given material determine the most suitable technique for the preparation of thin films of that material. In this thesis, pulsed laser deposition (PLD) was mainly used for growing thin film. The following sections discuss the methodology and experimental set-up used in various thin film deposition techniques.

2.1.1. Pulsed laser deposition (PLD)

Pulsed laser deposition, is a very effective thermal evaporation technique for the preparation of epitaxial films under moderate vacuum, or ultrahigh vacuum conditions. PLD is applicable to the deposition of a wide variety of oxide materials, including TCO materials [1, 2]. PLD is the deposition method of choice in the case of phase pure growth of multicomponent compositions. PLD technique requires a UV nanosecond pulsed laser source such as the frequency tripled (355 nm) or quadrupled (266 nm) solid state Nd:YAG laser, or the KrF (248 nm) or ArF (193 nm) excimer laser. In a typical PLD process, a focused train of high energy laser pulses, derived from a UV nanosecond pulsed laser source, is rastered over the target. A suitable substrate, often heated, is brought into contact with the laser plume (formed by the high

pulse energy beam–target interaction) comprising of atomic and molecular species ablated from the target. Typically, for TCO film deposition, the substrate temperature is maintained between 450 and 700 °C, and the oxygen partial pressure is usually kept below several millitorr. In the case of metal oxides, oxygen pressure plays a key role in n-type conductivity. Decrease in oxygen pressures promote the formation of oxygen vacancies which generates free carriers. For metal targets, the oxygen content in the chamber can be carefully regulated to promote formation of a targeted flux of oxygen radicals in the laser plume. This results in the appropriate oxygen deficient metal oxide film. This concept was exploited in the fabrication of ZnO: Al [3]. Although very high deposition rates up to ~ 600 μm/h have been reported, rates on the order of ~1 μm/h are more typical when high quality, epitaxial thin films are desired.

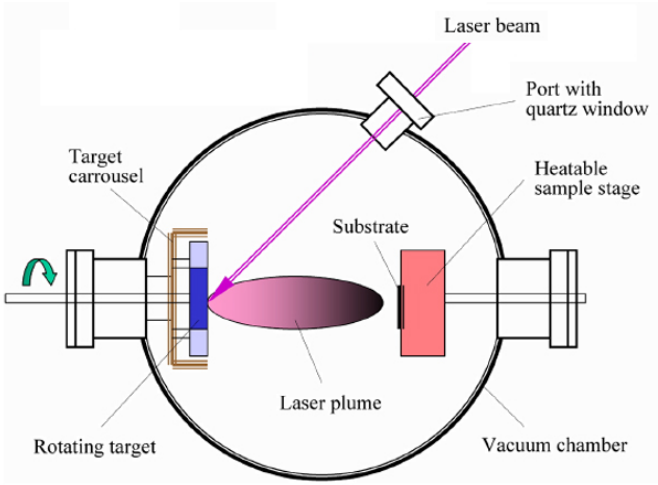

Figure. 2.1. Shematic diagram of a PLD chamber

Figure. 2.1. shows a schematic view of a pulsed laser deposition chamber. Provisions are made for controlling the ambient atmosphere within the chamber and substrate heating. Short wavelength irradiation of the target material creates an ablation plume that contacts the substrate. Bhosle *et al.* [4] investigated the role of substrate behavior and deposition conditions on the electrical and optical properties of Ga:ZnO films. The nature of grain orientation and grain boundary morphology that resulted from various deposition conditions, was found to play a significant role in carrier concentration and the mobility in thin films deposited on glass substrates. The PLD process is a versatile technique amenable to coupling with ultraviolet irradiation [5], oxygen radical assisted deposition [3], or magnetic field promoted deposition [6]. Thus, a magnetic field perpendicular to the laser plume is useful in preparing good quality Al:ZnO films. Deposited films exhibited a markedly low resistivity of 8.54×10^{-5} Ω cm and an average transmittance exceeding 91% over the visible wavelength range. The low resistivity is due to the fact that crystal growth disorder that originated at the film substrate interface could be suppressed through application of an external magnetic field that interacted with the plasma plume thereby yielding an increased mobility. C-axis orientation was promoted at the substrate, giving rise to the observed increase in mobility [7, 6]. Thus far, PLD has been the primary technique used to deposit TCO films that exhibit exceptionally low resistivity of the order of 10^{-5} Ω cm [6-9].

i) Mechanisms of PLD

The mechanism of pulsed laser deposition, in contrast to the simplicity of the set-up, is a very complex physical phenomenon. It not only involves the physical process of laser-material interaction under the impact of high-power

pulsed radiation on solid target, but also the formation of plasma plume with highly energetic species and even the transfer of the ablated material through the plasma plume onto the heated substrate surface. Thus the thin film formation process in PLD generally can be divided into the following four stages.

1. Laser radiation interaction with the target
2. Dynamics of the ablated materials.
3. Deposition of the ablation materials on the substrate.
4. Nucleation and growth of a thin film on the substrate surface

Each stage in PLD is critical to the formation of quality epitaxial, crystalline, stoichiometric and uniform thin film.

In the first stage, the laser beam is focused onto the surface of the target. At sufficiently high flux densities and short pulse duration, all elements in the target are rapidly heated up to their evaporation temperature. Materials are dissociated from the target surface and ablated out with stoichiometry as in the target. The instantaneous ablation rate is highly dependent on the fluences of the laser shining on the target. The ablation mechanisms involve many complex physical phenomena such as collisional, thermal, and electronic excitation, exfoliation and hydrodynamics.

During the second stage, the emitted materials tend to move towards the substrate according to the laws of gas-dynamics. The spot size of the laser and the plasma temperature has significant effects on the deposited film uniformity. The target-to-substrate distance is another parameter that governs the angular spread of the ablated materials. A mask placed close to the substrate could reduce the spreading.

The third stage is important to determine the quality of the thin film. The ejected high-energy species impinge onto the substrate surface and may induce various type of damage to the substrate. These energetic species sputter some of the surface atoms and a collision region is formed between the incident flow and the sputtered atoms. Film grows after a thermalized region is formed. The region serves as a source for condensation of particles. When the condensation rate is higher than the rate of particles ejected by the sputtering, thermal equilibrium condition can be reached quickly and film grows on the substrate surface.

The effect of increasing the energy of the adatoms has a similar effect of increasing substrate temperature on film growth [11]. Typical power densities involved in PLD are approximately 50 MW cm^{-2} for a reasonable growth rate (> 1 A^{o}/shot). The plasma is formed initially during laser target interaction in vacuum or in air and then again an explicit laser – plasma interaction occurs. Due to which ions in the plasma are accelerated to as much as 100 – 1000 eV [11]. Nucleation-and-growth of crystalline films depends on many factors such as the density, energy, ionization degree, and the type of the condensing material, as well as the temperature and the physico-chemical properties of the substrate.The two main thermodynamic parameters for the growth mechanism are the substrate temperature T and the supersaturation D_m of laser plasma. They can be related by the following equation

$$D_m = kT \ln(R/R_e) \qquad (2.1)$$

where k is the Boltzmann constant, R is the actual deposition rate, and R_e is the equilibrium value of deposition rate of the thin film at the temperature T.

The nucleation process depends on the interfacial energies between the three phases present – the substrate, the condensing material and the vapour. The critical size of the nucleus depends on the driving force, i.e. the deposition rate and the substrate temperature. For the large nuclei, a characteristic of small supersaturation, they create isolated patches (islands) of the film on the substrate, which subsequently grow and coalesce together. As the supersaturation increases, the critical nucleus shrinks until its height reaches on atomic diameter and its shape is that of a two-dimensional layer. For large supersaturation, the layer-by-layer nucleation will happen for incompletely wetted foreign substrates.

The crystalline film growth depends on the surface mobility of the adatom (vapour atoms). Normally, the adatom will diffuse through several atomic distances before sticking to a stable position within the newly formed film. The surface temperature of the substrate determines the adatom's surface diffusion ability. High temperature favours rapid and defect free crystal growth, whereas low temperature or large supersaturation crystal growth may be overwhelmed by energetic particle impingement, resulting in disordered or even amorphous structures.The mean thickness (N_{99}) at which the growing thin and discontinuous film reaches continuity, is given by the formula

$$N_{99} = A(1/R)^{1/3} \exp(-1/T) \qquad (2.2)$$

where R is the deposition rate (supersaturation related) and T is the temperature of the substrate and A is a constant related to the materials[11].

In the PLD process, due to the short laser pulse duration (~10 ns) and hence the small temporal spread (~10 ms) of the ablated materials, the deposition rate can be enormous (~10 nm/s). Consequently a layer-by-layer nucleation is favoured and ultra-thin and smooth film can be produced. In addition the rapid deposition of the energetic ablation species helps to raise the substrate surface temperature. In this respect PLD tends to demand a lower substrate temperature for crystalline film growth.

Pulsed laser deposition is the main growth technique used in the present study. The deposition was carried out in a vacuum chamber pumped by a turbo-molecular pump (Pfeiffer Vacuum Inc, Germany). The laser used was the third harmonics (355 nm) of Nd:YAG laser (Spectra Physics model GCR 150).

2.1.2. Sputtering

The sputtering process involves the creation of gas plasma usually of an inert gas such as argon by applying voltage between a cathode and anode. The cathode is used as a target holder and the anode is used as a substrate holder. Source material is subjected to intense bombardment by ions. By momentum transfer, particles are ejected from the surface of the cathode and they diffuse away from it, depositing a thin film onto a substrate. Sputtering is normally performed at a pressure of 10^{-2} –10^{-3} Torr.

Normally there are two modes of powering the sputtering system; dc and rf biasing [12–15]. In dc sputtering system a direct voltage is applied between the cathode and the anode. This method is restricted for conducting materials only. Radio frequency sputtering is suitable for both conducting and non-conducting materials; a high frequency generator (13.56 MHz) is connected

between the electrodes of the system. Magnetron sputtering is a process in which the sputtering source uses, magnetic field at the sputtering target surface.

This method appears to be the most popular technique for film deposition, owning to its cost effectiveness and capability for growing thin films on large area substrates; therefore, it became a somewhat conventional. A large number of publications (~ 1/3), relevant to TCO, do indeed pertain to this sputtering process. However, early applications of this method to deposition of TCO films were found to be quite costly, and sputtering was limited by low deposition rates, low ionization efficiencies in the plasma, and marked substrate heating effects which often led to inferior films [16]. Magnetron sputtering approaches were developed to help overcome these limitations. Magnetron sputtering is particularly useful when high deposition rates and low substrate temperatures are required. More recent developments have been made with a particular attempt to enhance deposition rates and to deposit films onto large area substrates through various technological improvements, such as closed field unbalanced magnetron sputtering, the use of variable field strength magnetrons, and pulsed magnetron sputtering [16–20]. Large area ITO film (30×40 cm^2) has been deposited onto glass substrates by r.f. magnetron sputtering, which exhibited good uniformity and homogeneity [21].

2.1.2. Vacuum evaporation

It is the most widely used technique for the preparation of thin films for the deposition of metals, alloys, and also many compounds, as it is very simple and convenient. Here the only requirement is to have a vacuum environment in which sufficient amount of heat is given to the evaporants to attain the vapour pressure necessary for the evaporation. The evaporated material is allowed to

condense on a substrate kept at a suitable temperature. A resistively heated tungsten or tantalum source is used to evaporate the charge. The important control parameters are the substrate temperature, evaporation rate, source to substrate distance and the oxygen partial pressure. Transparent conductors can be evaporated in three ways (i) by directly evaporating the metal oxides, (ii) reactive evaporation of the metal in the presence of oxygen and (iii) post oxidation of metal films. Always some deficiency of oxygen will be there when an oxide material is evaporated. To avoid this, the films must either be evaporated in the partial pressure of oxygen or require a post deposition heat treatment in air. Reports on the growth of ITO thin films by evaporation involve reactive evaporation of either metallic alloy or an oxide mixture [22-25]. Films grown by vacuum evaporation using oxide mixtures are usually deficient in oxygen and an oxygen partial pressure of 10^{-4} Torr is necessary to have transparent thin films. The preferred orientation observed in the vacuum evaporated films was (111). Thermal evaporation technique has been used for the deposition of metal electrodes in the present study.

2.2. Techniques for synthesis of nanostructured materials

As particle sizes drop from microns to tens of nanometers, metallic nanoparticles cease to behave as bulk metal and begin exhibiting quantum mechanical behavior similar to that of individual atoms**.** Ten hydrogen atoms stacked side-by-side measure only a single nanometer. The lure of nanotechnology is not just making small devices; but to construct the smallest physical structures possible. A single atom is only a tenth of a nanometer in diameter. Nanotechnology is, in a very literal sense, an opportunity to play with

nature's own building blocks [26]. The realization of the full potential of nano technological system has so far been limited due to their difficulties in their synthesis and subsequent assembly into useful functional structures and devices. The three steps in the development of nano science and technology include material preparation, property characterization and device fabrication. Preparation of nano particle is being advanced by numerous physical and chemical techniques. Nano structured materials are synthesized using a combination of approaches, for example melting and solidification process followed by thermodynamical treatments, or solution/vacuum deposition, and growth process. In many cases however the final product is dictated by the kinetics of thermodynamics of systems. There are basically two broad areas of synthetic techniques for nanostructured materials namely

(1) Physical methods and

(2) Chemical method

2.2.1. Physical methods

Several different physical methods are currently in use for the synthesis and commercial production of nano structured materials. The first and the most widely used technique involve the synthesis of single-phase metals and ceramic oxides by the inert-gas evaporation technique [27]. The generation of atom clusters by gas phase condensation proceeds by evaporating a precursor material, either a single metal or a compound, in a gas maintained at a low pressure, usually below 1 atm. The evaporated atoms or molecules undergo a homogeneous condensation to form atom clusters via collisions with gas atoms or molecules in the vicinity of a cold-powder collection surface. The clusters once formed must be removed from the region of deposition to prevent further

aggregation and coalescence of the clusters. These clusters are readily removed from the gas condensation chamber either by natural convection of the gas or by forced gas flow. Sputtering is another technique used to produce nano structured materials clusters as well as a variety of thin films. This method involves the ejection of atoms or clusters of designated materials by subjecting them to an accelerated and highly focused beam of inert gas such as argon or helium. The third physical method involves the generation of nanostructured materials via severe mechanical deformation. In this method nano structured materials are produced not by cluster assembly but rather by structural degradation of coarser-grained structures induced by the application of high mechanical energy. The nanometer-sized grains nucleate within the shear bands of the deformed materials converting a coarse-grained structure to an ultra fine powder. The heavy deformation of the coarser materials is effected by means of a high-energy ball mill or a high-energy shear process. Although this method is very useful in generating commercial quantities of the material, it suffers from the disadvantage of contamination problems resulting from the sources of the grinding media.

Self-assembled quantum dots nucleate spontaneously under certain conditions during molecular beam epitaxy [MBE] and metallorganic vapour phase epitaxy[MOVPE], when a material is grown on a substrate to which it is not lattice matched. The resulting strain produces coherently strained islands on top of a two-dimensional “wetting layer”. This growth mode is known as Stranski-Krastanov growth. The islands can be subsequently buried to form the quantum dot. This fabrication method has potential for applications in quantum cryptography (i.e. single photon sources) and quantum computation [27]. The

main limitations of this method are the cost of fabrication and the lack of control over positioning of individual dots.

Laser ablation had been identified as a versatile technique for the preparation of nanostructured thin films, mainly nanorods, quantum wells and quantum dots. Precise control over the size of the nanostructures could be attained by playing various deposition parameters like substrate temperature, substrate to target distance, gaseous atmosphere in the chamber and laser energy density during the pulsed laser deposition [28]. Recently liquid phase-pulsed laser ablation technique (LP-PLA) has been evolved as a synthesis technique for the preparation of nano particles [29]. In this method, the bulk target of the material is immersed in a liquid taken in a beaker (for example water) and then the laser beam (from Nd: YAG or excimer laser) is allowed to focus through the liquid on to the target surface. A simple experimental setup of LP-PLA technique is shown in figure 2.2. Plasma of the ejected species disperses directly to the liquid in which the target is immersed. By controlling the energy density of the laser beam and using liquids containing surfactants, size of the particle can be tuned. This LP-PLA is very simple, by product free and clear technique, because quantum dots can be directly dispersed in liquid medium without the play of much chemistry. Transparent and highly luminescent ZnO quantum dots dispersed water can be prepared by this method using third harmonic Nd: YAG laser.

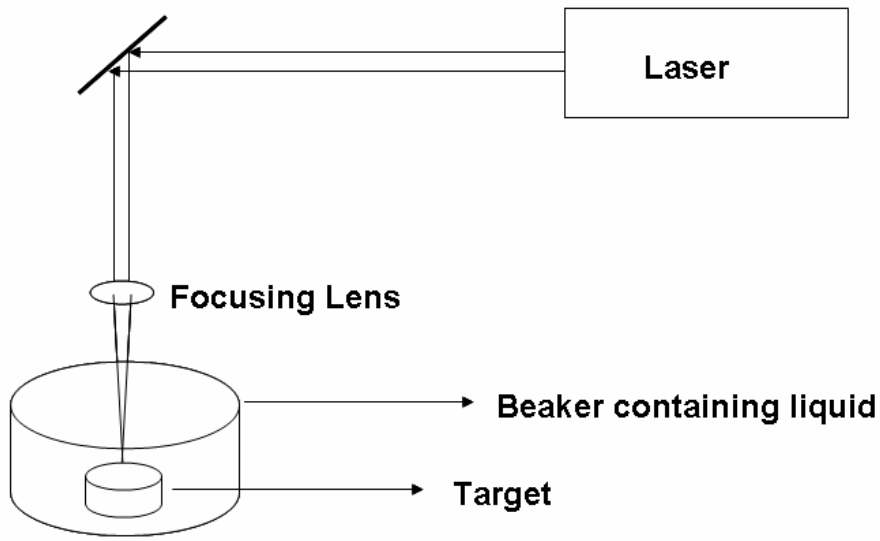

Figure 2.2. Shows the setup of liquid phase laser ablation

2.2.2. Chemical methods

Chemistry has played a major role in developing new materials with novel and technologically important properties. The advantage of chemical synthesis is its versatility in designing and synthesizing new materials that can be refined into a final product. The primary advantage that chemical processes offer over other methods is good chemical homogeneity, as chemical synthesis offers mixing at the molecular level. Molecular chemistry can be designed to prepare new materials by understanding how matter is assembled on an atomic or molecular level and the consequent effects on the desired material macroscopic properties. A basic understanding on the principles of crystal chemistry, thermodynamics, phase equilibrium and reaction kinetics is important to take advantage of the many benefits that chemical processing has to offer.

There are certain difficulties in chemical processing. In some preparations, the chemistry is complex and hazardous. Contamination can also result from the byproducts being generated or side reactions in the chemical process. This should be minimized or avoided to obtain desirable properties in the final product. Agglomeration can also be a major cause of concern at any stage in a synthetic process and it can dramatically alter the properties of the materials. Agglomeration frequently makes it more difficult to consolidate nanoparticles to a fully dense and compact. Finally, although many chemical processes are scalable for economical production, it is not always straight forward for all systems.

Solution chemistry is used sometimes to prepare the precursor, which is subsequently converted to the nano phase particles by non-liquid phase chemical reactions. Precipitation of a solid from a solution is a common technique for the synthesis of fine particles. The general procedure involves reactions in the aqueous or non-aqueous solutions containing the soluble or suspended salts [27]. Once the solution becomes super saturated with the product, the precipitate is formed by either homogeneous or heterogeneous nucleation. The formation of a stable material with or without the presence of a foreign species is referred to as heterogeneous or homogeneous nucleation. The growth of the nuclei after formation usually proceeds by diffusion, in which case concentration gradients and reaction temperatures are very important in determining the growth rate of particles, for example to form mono dispersed particles. For instance to form unagglomerated particles with a very narrow size distribution, all the nuclei must form at nearly the same time and the subsequent growth must occur without further nucleation or agglomeration of particles.

Nano structured materials are also prepared by chemical vapour deposition (CVD) or chemical vapour condensation (CVC). In these processes a chemical precursor is converted to the gas phase and it then undergoes decomposition at either low or atmospheric pressure to generate the nanostructured particles. These products are then subjected to transport in a carrier gas and collected on a cold substrate, from where they are scarped and collected. The CVC method may be used to produce a variety of powders and fibers of metals, compounds, or composites. The CVD method has been employed to synthesis several ceramic metals, intermetallics, and composite materials. Semiconductor clusters have traditionally been prepared by use of colloids, micelles, polymers, crystalline hosts, and glasses [27]. The clusters prepared by these methods have poorly defined surfaces and a broad size distribution, which is detrimental to the properties of semiconductor materials. A more detailed discussion on nanomaterial preparation and nanostructure fabrication can be found in the recent literature [27].

2.3. Characterization tools

2.3.1. Thin film thickness

Thickness is one of the most important thin film properties to be characterized since it plays an important role in the film properties unlike a bulk material. Reproducible properties are achieved only when the film thickness and the deposition parameters are kept constant. Film thickness may be measured either by in-situ monitoring of the rate of deposition or after the film deposition.

The thicknesses of the thin films prepared for the work presented in this thesis were measured by a stylus profiler (Dektak 6M).

i) Stylus profiler

The stylus profiler takes measurements electromechanically by moving the sample beneath a diamond tipped stylus. The high precision stage moves the sample according to a user defined scan length, speed and stylus force. The stylus is mechanically coupled to the core of a linear variable differential transformer (LVDT). The stylus moves over the sample surface. Surface variations cause the stylus to be translated vertically. Electrical signals corresponding to the stylus movement are produced as the core position of the LVDT changes. The LVDT scales an ac reference signal proportional to the position change, which in turn is conditioned and converted to a digital format through a high precision, integrating, analog-to-digital converter [30]. The film whose thickness has to be measured is deposited with a region masked. This creates a step on the sample surface. Then the thickness of the sample can be measured accurately by measuring the vertical motion of the stylus over the step.

2.3.2. Surface morphology

Surface morphology is an important property since while going for multilayer devices roughness of the thin film surface play an important role. Some of the characterization tools which clearly demonstrates an idea about the surface of the thin films is described below.

i) Scanning electron microscope (SEM)

The scanning electron microscope (SEM) is a microscope that uses electrons rather than light to form an image. There are many advantages for using the SEM instead of a light microscope [31, 32]. The SEM has a large depth of field, which allows a large amount of the sample to be in focus at the same time. The SEM also produces images of high resolution, which means that closely spaced features can be examined at a high magnification. Preparation of the samples is relatively easy since most SEMs only require that sample should be conductive. The combination of higher magnification, larger depth of focus, greater resolution, and ease of sample observation makes SEM one of the most heavily used instruments in the research field. The electron beam comes from a filament, made of various types of materials. The most common is the Tungsten hairpin gun. This filament is a loop of tungsten that functions as the cathode. A voltage is applied to the loop, causing it to heat up. The anode, which is positive with respect to the filament, forms powerful attractive forces for electrons. This causes electrons to accelerate toward the anode. The anode is arranged, as an orifice through which electrons would pass down to the column where the sample is held. Other examples of filaments are lanthanum hexaboride filaments and field emission guns.

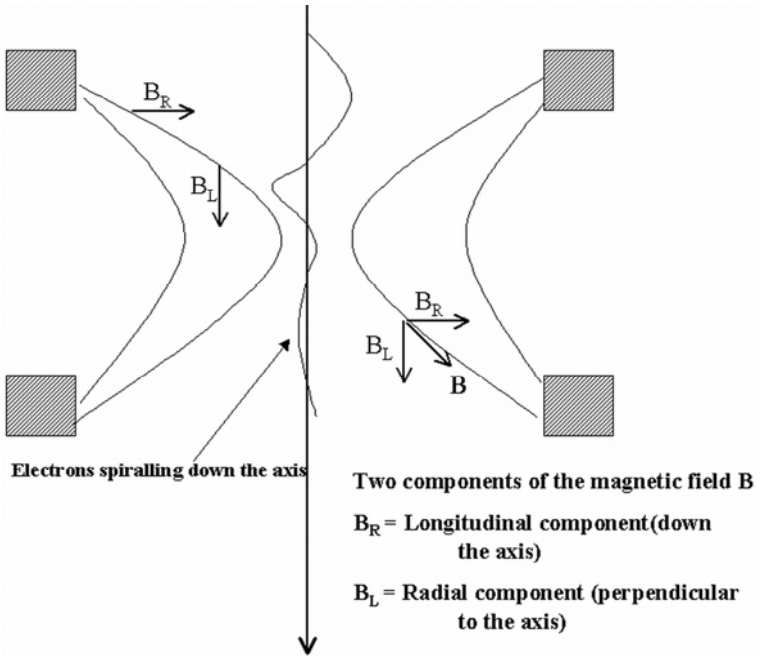

Figure 2.3. The focusing of electrons in SEM

The streams of electrons that are attracted through the anode are made to pass through a condenser lens, and are focused to very fine point on the sample by the objective lens (figure 2.3). The electron beam hits the sample, producing secondary electrons from the sample. These electrons are collected by a secondary detector or a backscatter detector, converted to a voltage, and amplified. The amplified voltage is applied to the grid of the CRT that causes the intensity of the spot of light to change. The image consists of thousands of spots of varying intensity on the face of a CRT that correspond to the topography of the sample. In the present thesis, JEOL JSM 5600 was used for SEM analysis.

ii) Atomic force microscopy (AFM)

Following the invention of the scanning tunneling microscope (STM), a number of new scanning probe microscopes (SPM) has been developed that use the key components of the STM. One of the most important SPM is the atomic force microscope (AFM) [31, 32]. In atomic force microscopy a tip, integrated to the end of a spring cantilever, is brought within the interatomic separations of a surface, such that the atoms of the tip and the surface are influenced by interatomic potentials. As the tip is rastered across the surface, it bounces up and down with the contours of the surface. By measuring the displacement of the tip (*i.e.* the deflection of the cantilever), one can theoretically map out the surface topography with atomic resolution. The first AFM's measured cantilever deflections using a piggy-backed STM. Later instruments used more practical optical techniques. The AFM is essentially identical in concept to the scanning profilometer, except that the deflection-sensitivity and resolution are improved by several orders of magnitude.

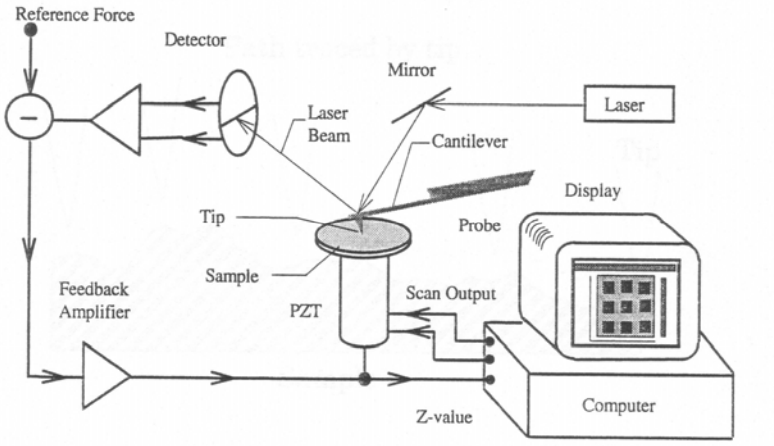

Figure 2.4. The essential elements of an AFM

There are a large number of applications for the AFM, including biological systems, polymers, and a host of insulator and semiconductor materials.

a) Operating principles of AFM

An AFM images a surface in a manner analogous to the gramophone stylus sensing the groves of gramophone disk. The essential elements of an AFM are shown in the figure 2.4. The tip is attached to a cantilever type spring as shown in the figure 2.5. As the tip and sample interact, forces act on the tip and cause the cantilever (spring) to deflect. The cantilever position is monitored by a position detector. The output of the detector is connected to a feedback controller that regulates the force between the sample and the tip by moving the sample up or down. The sample is moved by a PZT scanning actuator. The cantilever must be soft enough to deflect a measurable amount without damaging the surface features of the sample. The amount of deflection is proportional to the force acting on the tip:

$$F_{spring} = -k \cdot \Delta Z \tag{2.3}$$

where F is the force on the sample, k is the spring constant of the cantilever, and, ΔZ is the deflection of the cantilever.

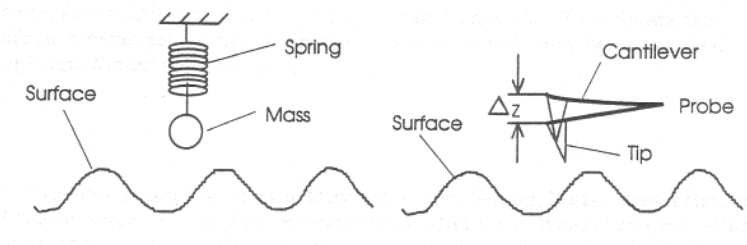

Figure 2.5. shows how the tip is attached to the cantilever.

Variations of AFM include contact mode, dynamic force mode, phase mode, current image, friction force microscope, magnetic force microscope, surface potential microscope, *etc*. In the present work, AFM from Veeco was used for the morphological study

2.3.2. Compositional analysis

In order to check the stoichiometry of the deposited films, compositional analysis is essential and some of the characterization tools used in the present investigation is described below.

i) Energy dispersive x-ray (EDX) analysis

EDX analysis stands for energy dispersive x-ray analysis. It is sometimes referred to also as EDS or EDAX analysis. It is a technique used for identifying the elemental composition of the specimen, on an area of interest thereof. The EDX analysis system works as an integrated feature of a scanning electron microscope (SEM), and can not operate on its own without the latter [31, 32].

During EDX Analysis, the specimen is bombarded with an electron beam inside the scanning electron microscope. The bombarding electrons collide with the specimen atom's own electrons, knocking some of them off in the process. A position vacated by an ejected inner shell electron is eventually occupied by a higher-energy electron from an outer shell. To be able to do so, however, the transferring outer electron must give up some of its energy by emitting an X-ray. The amount of energy released by the transferring electron depends on which shell it is transferring from, as well as which shell it is transferring to. Furthermore, the atom of every element releases X-rays with unique amounts of energy during the transferring process. Thus, by measuring

the energy of the X-rays emitted by a specimen during electron beam bombardment, the identity of the atom from which the X-ray was emitted can be established.

The output of an EDX analysis is an EDX spectrum, which is a plot of how frequently an X-ray is received for each energy level. An EDX spectrum normally displays peaks corresponding to the energy levels for which the most X-rays had been received. Each of these peaks are unique to an atom, and therefore corresponds to a single element. The higher a peak in a spectrum, the more concentrated the element is in the specimen. An EDX spectrum plot not only identifies the element corresponding to each of its peaks, but the type of X-ray to which it corresponds as well. For example, a peak corresponding to the amount of energy possessed by X-rays emitted by an electron in the L-shell going down to the K-shell is identified as a K_α peak. The peak corresponding to X-rays emitted by M-shell electrons going to the K-shell is identified as a K_β peak as shown in figure 2.6.

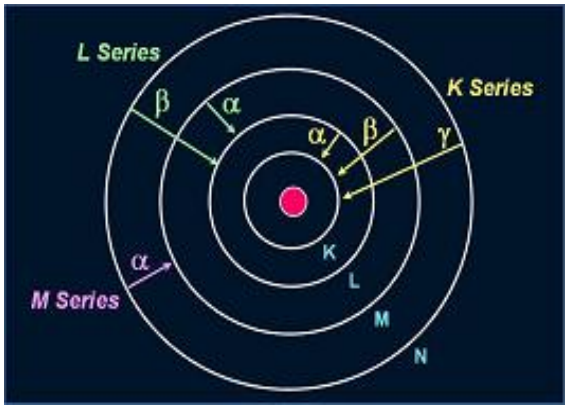

Figure 2.6. The emission of x rays.

ii) X-ray photoelectron spectroscopy (XPS)

X-ray photoelectron spectroscopy is also known as electron spectroscopy for chemical analysis or ESCA. In XPS, radiation from an x-ray source strikes the sample. The deep inner shell electrons are excited and both core and valence band electrons are ejected with characteristic energy and release of x-ray photoelectrons [31, 32].

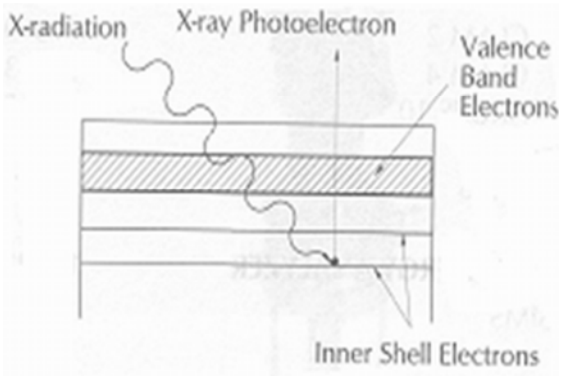

Figure 2.7. The electronic transitions due to the incident x-rays.

Electronic transitions are shown in the figure 2.7. Depending on the atomic structures, the wavelength of the x-ray will be different. Electrons emitted from atoms within a few atomic layers of the surface escape and are energy analyzed. Results provide quantitative and qualitative information about oxidation states of surface and near-surface atoms, surface impurities, and fundamental interactions between surface species. Standard XPS provides excellent chemical information but restricted spatial data. If, however, a lens with a narrow acceptance angle is placed at the

energy analyzer's entrance, small area XPS (SAXPS) provides an image of surface features with a resolution of 280 pm (as shown in the figure 2.8).

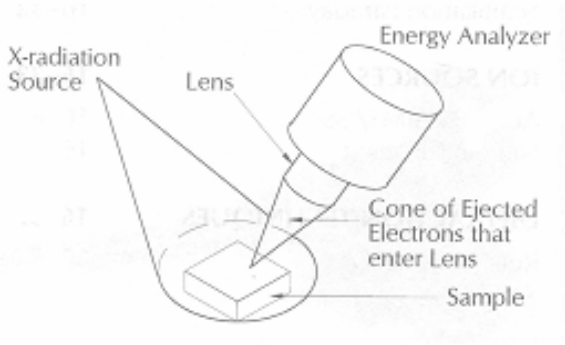

Figure 2.8. Small area XPS (SAXPS)

If the X-ray source is monochromatic, the electron's kinetic energy is used to measure its binding energy from the relation X-ray energy minus binding energy equals kinetic energy. The most common source creates X-rays by bombarding either Al or Mg targets with high energy electrons to produce 1486.6eV and 1253.6eV photons, respectively. Increasingly, synchrotron radiation (the tangential photon flux formed when high energy charged particles are deflected) is the source of choice. The photon energy, ranging from infrared to X-ray, is resolved by a monochromator into a monoenergetic, high flux beam that provides much greater experimental flexibility than a fixed frequency X-ray source. XPS with Al K_{α} radiation source (1486.6 eV) was used in the present investigation.

iii) Inductively coupled plasma – Atomic emission spectroscopy (ICP-AES)

Inductively coupled plasma atomic emission spectroscopy (ICP-AES), also referred to as inductively coupled plasma optical emission spectrometry (ICP-OES), is a type of spectrophotometric technique, exploiting the fact that excited electrons emit energy at a given wavelength as they return to ground state [33]. This technique uses plasma called inductively coupled plasma to produce excited atoms. The fundamental characteristic of this process is that each element emits energy at specific wavelengths peculiar to its chemical character. Although each element emits energy at multiple wavelengths, in the ICP-AES technique it is most common to select a single wavelength (or a very few) for a given element. The intensity of the energy emitted at the chosen wavelength is proportional to the amount (concentration) of that element in the analyzed sample. Thus, by determining which wavelengths are emitted by a sample and by determining their intensities, the analyst can quantify the elemental composition of the given sample relative to a reference standard. ICP –AES measurement was done in the present work using Thermo Electron IRIS INTREPID II XSP DUO.

2.3.3. Structural characterization

i) X-ray diffraction

The structural characterization was done by recording the X-ray diffraction (XRD) pattern of the samples. XRD pattern was taken using Rigaku X-ray diffractometer with Cu-K_α radiation (λ=1.5414A^0). A given substance always produces a characteristic diffraction pattern whether that substance is present in the pure state or as one constituent of a mixture of substances. This

fact is the basis for the diffraction method of chemical analysis. The particular advantage of X-ray diffraction analysis is that it discloses the presence of a substance, as that substance actually exists in the sample and not in terms of its constituent chemical elements. Diffraction analysis is useful whenever it is necessary to know the state of chemical combination of the elements involved or the particular phase in which they are present. Compared with ordinary chemical analysis the diffraction method has the advantage that it is usually much faster, requires only very small quantity of sample and is non destructive [34, 35].

The basic law involved in the diffraction method of structural analysis is the Bragg's law. When monochromatic beam of x-rays impinge upon the atoms in a crystal lattice, each atom acts as a source of scattering. The crystal acts as series of parallel reflecting planes. The intensity of the reflected beam at certain angles will be maximum when the path difference between two reflected waves from two different crystal planes is an integral multiple of λ. This condition is termed as Bragg's law and is given by $n\lambda = 2d \sin\theta$, where n is the order of diffraction, λ is the wavelength of X-rays, d is the spacing between consecutive parallel planes and θ is the glancing angle (or the complement of the angle of incidence) [36].

X-ray diffraction studies give a whole range of information about the crystal structure, orientation, average crystalline size and stress in the powder. Experimentally obtained diffraction patterns of the sample are compared with the standard powder diffraction files published by the international centre for diffraction data (ICDD). The average grain size of the film can be calculated using the Scherrer's formula [34],

$$d = \frac{0.9\lambda}{\beta Cos\theta} \qquad (2.4)$$

where, λ is the wavelength of the x-ray and β is the full width at half maximum intensity in radians. The lattice parameter values (a and c) for hexagonal system can be calculated from the following equations using the (hkl) parameters and the interplanar spacing d.

$$\frac{1}{d^2} = \frac{4}{3}\left(\frac{h^2 + hk + k^2}{a^2}\right) + \frac{l^2}{c^2} \qquad (2.5)$$

X-ray diffraction measurements of the films in the present studies were done using Rigaku automated x-ray diffractometer. The filtered copper K_α (λ=1.5418A^0) radiation was used for recording the diffraction pattern. XRD measurent of samples in this thesis work was done using Rigaku with Cu-K_α radiation (1.5414 A^o).

ii) Transmission electron microscopy (TEM)

Transmission electron microscopy (TEM) is an imaging technique whereby a beam of elecrons is focused onto a specimen causing an enlarged version to appear on a fluorescent screen or layer of photographic film or to be detected by a CCD camera. The first practical transmission electron microscope was built by Albert Prebus and James Hillier at the University of Torondo in 1938 using concepts developed earlier by Max Knoll and Ernst Ruska. Electrons are generated by a process known as thermionic discharge in the same manner as the cathode in a cathode ray tube, or by field emission; they are then accelerated by an electric field and focused by electrical and magnetic fields onto the sample. The electrons can be focused onto the sample providing a resolution far

better than is possible with light microscopes, and with improved depth of vision. Details of a sample can be enhanced in light microscopy by the use of stains. Similarly with electron microscopy, compounds of heavy metals such as osmium, lead or uranium can be used to selectively deposit in the sample to enhance structural details. The electrons that remain in the beam can be detected using a photographic film, or fluorescent screen [31]. So areas where electrons are scattered appear dark on the screen, or on a positive image.

An additional class of these instruments is the electron cryomicroscope, which includes a specimen stage capable of maintaining the specimen at liquid nitrogen or liquid helium temperatures. This allows imaging specimens prepared in vitreous ice, the preferred preparation technique for imaging individual molecules or macromolecular assemblies. Another type of TEM is the scanning transmission electron microscope (STEM), where the beam can be rastered across the sample to form the image. In analytical TEMs the elemental composition of the specimen can be determined by analysing its X-ray spectrum or the energy-loss spectrum of the transmitted electrons. Modern research TEMs may include aberration correctors, to reduce the amount of distortion in the image, allowing information on features on the scale of 0.1 nm to be obtained (resolutions down to 0.08 nm has been demonstrated, so far). Monochromators may also be used which reduce the energy spread of the incident electron beam to less than 0.15 eV.

From TEM images, size of the nanoparticles can be determined. Parallel lines in the high resolution transmission electron micrograph (HRTEM) represents planes in the crystal lattice and distance between them corresponds to d spacing. By comparing these d spacing values with the JCPDS data, one can

identify the orientation of the planes in the synthesized material. Selective area electron diffraction (SAED) is the map of the reciprocal lattice which will also give the signature of various planes in which material has been grown. Depending on the crystalline nature of the material, the SAED pattern will be orderly arranged spots, distinguishable ring or fused rings. But in the case of quantum dots concentric rings were observed in the SAED. The d spacing of the planes corresponding to the rings can be determined by the following equation

$$(Dd) = CL\lambda \tag{2.6}$$

Where L is the effective camera length, λ is the de-Broglie wavelength of the accelerating electrons, D is the ring diameter of a standard electron diffraction pattern and d is the interplanar spacing [31]. The term in the right hand side of the equation is referred to as the camera constant. TEM, JEOL operating at an accelerating voltage of 200 kV was used for the confirmation of the formation of nanoparticles in the present work.

2.3.4. Optical studies

i) Determination of band gap energy

a) Transmission spectroscopy

Intrinsic optical absorption of a single photon across the band gap is the dominant optical absorption process in a semiconductor. When the energy of the incident photon ($h\nu$) is larger than the band gap energy, the excitation of electrons from the valence band to the empty states of the conduction band occurs. The light passing through the material is then absorbed and the number of electron hole pairs generated depends on the number of incident photons $S_0(\nu)$ (per unit area, unit time and unit energy). The frequency ν is related to the wavelength λ by the relation, $\lambda = c/\nu$, where c is the velocity of light. The

photon flux $S(x,\nu)$ decreases exponentially inside the crystal according to the relation [37],

$$S(x,\nu) = S_0(\nu) \exp(-\alpha x) \qquad (2.7)$$

where, the absorption coefficient α, ($\alpha(\nu) = 4\pi k\upsilon/c$) is determined by the absorption process in semiconductors and k is the extinction coefficient.

For the parabolic band structure, the relation between the absorption coefficient (α) and the band gap of the material is given by [37],

$$\alpha = \frac{A}{h\nu} (h\nu - E_g)^r \qquad (2.8)$$

where, r = 1/2 for allowed direct transitions, r = 2 for allowed indirect transitions, r = 3 for forbidden indirect transitions and r = 3/2 for forbidden direct transitions. A is the parameter which depends on the transition probability. The absorption coefficient can be deduced from the absorption or transmission spectra using the relation,

$$I = I_0 e^{-\alpha t} \qquad (2.9)$$

where, I is the transmitted intensity and I_0 is the incident intensity of the light and t is the thickness of the film. In the case of direct transition, from equation 2.8, $(\alpha h\nu)^2$ will show a linear dependence on the photon energy ($h\nu$). A plot of $(\alpha h\nu)^2$ against $h\nu$ will be a straight line and the intercept on energy axis at $(\alpha h\nu)^2$ equal to zero will give the band gap energy. The transmissions of the

thin films were recorded using Jasco V 500 spectrophotometer in the present studies.

b) Diffuse reflectance spectroscopy

The measurement of diffused radiation reflected from a surface constitutes the area of spectroscopy known as diffuse reflectance spectroscopy. Diffuse reflectance spectrometry concerns one of the two components of reflected radiation from an irradiated sample, namely specular reflected radiation, R and diffusely reflected radiation, R_∞. The former component is due to the reflection at the surface of single crystallites while the latter arises from the radiation penetrating into the interior of the solid and re-emerging to the surface after being scattered numerous times. These spectra can exhibit both absorbance and reflectance features due to contributions from transmission, internal and specular reflectance components as well as scattering phenomena in the collected radiation.

Based on the optical properties of the sample, several models have been proposed to describe the diffuse reflectance phenomena. The Kubelka-Munk model put forward in 1931 is widely used and accepted in diffuse reflectance infrared spectrometry.

The intensity of the reflected light depends on the scattering coefficient s and the absorption coefficient k. The reflectance data can be converted to absorbance by Kubelka-Munk equation [38,39]. Kubelka-Munk equation is as

$$\text{Log}\,[(1- r_\infty)^2 /2\, r_\infty\,] = \text{Log}\, k - \text{Log}\, s \qquad (2.10)$$

Where $r_\infty = R_\infty(\text{sample})/ R_\infty(\text{standard})$. Here the standard used is MgO. R_∞ (standard) is taken as unity. R_∞(sample) is the diffuse reflectance of the sample ($R= I_{sam}/I_{ref}$).

Equation 2.10 Implies,

$$(1- R)^2 /2\, R = k/s \qquad (2.11)$$

The band gap is estimated from the plot of $\{(k/s).h\nu\}^2$ vs. hν (hν is the photon energy) by extrapolating the graph to the x axis. DRS was recorded using Jasco V 500 spectrophotometer in the present studies.

ii) Photoluminescence (PL)

Luminescence in solids is the phenomenon in which electronic states of solids are excited by some energy from an external source and the excited states release energy as light. When short-wavelength light illuminate a solid and result in the emission of higher wavelength, the phenomenon is called photoluminescence (PL) [40]. PL is divided into two major types: Intrinsic and extrinsic depending on the nature of electronic transition producing it.

a) Intrinsic luminescence

There are three kinds of intrinsic: 1) band-to-band luminescence 2) exciton luminescence 3) cross-luminescence.

1) Band –to –band luminescence:

Luminescence owing to the band-to-band transition, ie to the recombination of an electron in the conduction band with a hole in the valance band, can be seen

in pure crystal at relatively high temperature. This has been observed in Si,Ge and IIIb-Vb compounds such as GaAs.

2) Exciton luminescence:

An exciton is a composite particle of an excited electron and a hole interacting with one another. It moves in a crystal conveying energy and produces luminescence owing to the recombination of the electron and the hole. There are two kinds of excitons: Wannier exciton and Frenkel exciton.

The Wannier exciton model express an exciton composed of an electron in the conduction band and a hole in the valence band bound together by couloumb interaction. The expanse of the wavefunction of the electron and hole in Wannier exciton is much larger than the lattice constant. The excitons in IIIb-Vb and IIb-VIb compounds are examples for Wannier exciton. The Frenkel exciton model is used in cases where expanse of electron and hole wave function is smaller than lattice constant. The excitons in organic molecular crystals are examples of Frenkel exciton.

3) Cross luminescence:

Cross luminescence is produced by the recombination of an electron in the valance band with a hole created in the outer most core band. This is observed in number of alkali and alkaline-earth halides and double halides. This takes place only when the energy difference between the top of valance band and that of conduction band is smaller than the band gap energy. This type of luminescence was first observed in BaF_2.

b) Extrinsic luminescence

Luminescence caused by intentionally incorporated impurities, mostly metallic impurities or defects is classified as extrinsic luminescence. Most of the observed type of luminescence of practical application belongs to this category. Intentionally incorporated impurities are activators and materials made luminescent in this way are called phosphors. Extrinsic luminescence in ionic crystals and semiconductors is classified into two types: unlocalized and localized. In the unlocalized type, the electrons and holes of the host lattice participate in the luminescence process, while in localized type the luminescence excitation and emission process are confined in a localized luminescence center. For studying the low temperature PL of thin films, a fourth harmonic pulsed Nd: YAG laser operating at 266 nm was used as an exciting source and resulting luminescence was collected using gated CCD in the temperature range 77 K to 300 K. The emission and excitation spectra for the liquid samples are recorded using Fluorolog –3 spectroflurometer having a 150W Xenon arc lamp, monochromator and a CCD detector.

iii) Raman spectroscopy

Raman spectroscopy is a technique that can detect both organic and inorganic species and measure the crystallanity of solids. Raman spectroscopy is based on the Raman effect, first reported by Raman in 1928 [41]. If the incident photon imparts part of it's energy to the lattice in the form of a phonon it emerges as a lower energy photon. This down converted frequency shift is known as *Stokes-shifted* scattering. Anti-stokes shifted scattering results when the photon absorbs a phonon and emerges with higher energy. The anti-Stokes mode is much weaker than the Stokes mode and it is the Stokes-mode scattering

that is usually monitored. In Raman spectroscopy a laser beam, referred to as the pump, is incident on the sample. The weak scattered light or the Raman signal is passed through a double monochromator to reject the Raleigh scattered light and the Raman shifted wavelengths are detected by a photodetector. Various properties of the semiconductors, mainly composition and crystal structure can be determined. The Stokes line shifts and broadens becomes asymmetric for microcrystalline Si with grain sizes below 10 nm [42]. The lines become very broad for amorphous semiconductors, allowing distinction to be made between single crystal, polycrystalline, and amorphous materials. In the present work, Raman studies was carried out with micro Raman (Jobin Yvon Horiba) with excitation source as argon ion laser (488 nm).

2.3.5. Electrical characterization

i) Resistivity by two probe method

The resistivity of some of the films with high resistance was determined by the two-probe method with the electrodes in planar geometry. Evaporated indium layers or high conducting silver paste was used as the electrodes. The current voltage measurements were carried out using a Keithley`s source measure unit (Model SMU 236). The resistivity (ρ) of the films was calculated applying ohm's law, by the relation $\rho = RA/L$. Here R is the resistance given by the slope of the current – voltage characteristic curves, A is the area of the film in planar geometry given by the product of the film thickness and the width of the film, L is the spacing between the electrodes. The I-V measurements were taken using a Keithley's source measure unit (SMU 236).

ii) Hall measurement

The electrical resistivity of a semiconductor thin film can be written using Ohm's law,

$$\rho = \frac{1}{en\mu} \qquad (2.12)$$

where 'ρ' is the film resistivity, 'e' is the electronic charge, 'n' is the number of carriers corresponding to the carrier concentration and 'μ' is the carrier mobility. According to Ohm's law the carrier mobility affects resistivity. Low resistivity can be achieved by increasing the carrier concentration or mobility or both. Increasing carrier concentration is self-limiting because at some point the increased number of free carriers decreases the mobility of the film due to carrier scattering. Hence there is a trade off between the carrier density and carrier mobility for achieving low resistivity.

In the case of Zinc oxide films, the resistivity (ρ), carrier concentration (n), sheet resistance and carrier mobility (μ) were measured using four point probe in the van der Pauw configuration [43]. Samples used were 1 cm x 1 cm in size. The ohmic contacts were made using indium. Indium paste was applied at the corners of the sample symmetrically as shown in figure 2.9.

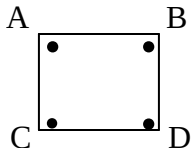

Figure 2.9. Symmetric contact of the four probes for taking the hall measurements.

Let R_1 be the potential difference between A and B per unit current through C and D or vice versa. Similarly R_2 the potential difference between B and C per unit current through D and A.

Then sheet resistance R_s can be calculated using the relation

$$R_s = \left(\frac{\pi}{\ln 2}\right)\left(\frac{R_1 + R_2}{2}\right) f\left(\frac{R_1}{R_2}\right) \qquad (2.13)$$

Where $f\left(\frac{R_1}{R_2}\right)$ is the van der Pauw function and is given by the relation,

$$f\left(\frac{R_1}{R_2}\right) = 1 - 0.3466\left(\frac{R_1 - R_2}{R_1 + R_2}\right)^2 \qquad (2.14)$$

The Hall signal was measured between two ends while passing the current through the other two ends. Hall mobility is,

$$\mu = \Delta R \times \frac{10^8}{BR_s} \qquad (2.15)$$

Where ΔR is the change in resistance due to magnetic field (B), which was applied to measure Hall voltage. Carrier concentration was determined using the equation 2.12. The hall coefficient R_H is given by,

$$R_H = \mu \rho \qquad (2.16)$$

The type of carriers can be understood from the sign of the R_H. The negative values of R_H correspond to the electrons (n-type) and positive values to holes (p-type) responsible for conduction.

iii) Thermopower measurement – Carrier type determination

Thermo power measurement is a useful technique for the evaluation of the type of carriers responsible for the conduction. Thermo power measurements were carried out using an indigenously made automated set up [44]. The thermal gradients applied at the thin film surface produce current in the semiconductor. This constitutes the thermoemf (ΔV) corresponds to thermal gradient (ΔT). The slope of the ΔV versus ΔT curve gives the Seebeck coefficient. A positive Seebeck coefficient is obtained when the majority carriers are holes and a negative Seebeck coefficient for electrons. This technique is especially useful for characterisation of type of carriers in semiconductor materials with low mobility.

2.4. References

1. S. Christoulakis, M. Suchea, M. Katharakis, N. Katsarakis, E. Koudoumas and G. Kiriakidis, Rev. Adv. Mater. Sci. **10** (2005) 331.
2. M. Grundmann, H. Wenckstern, R. Pickenhain, T. Nobis, A. Rahm and M. Lorenz, Superlattices Microstruct. **38** (2005) 317.
3. K. Matsubara, P. Fons, K. Iwata, A. Yamada and S. Niki, Thin Solid Films **422** (2002) 176.
4. V. Bhosle, A. Tiwari and J. Narayan, J. Appl. Phys. **100** (2006) 033713.
5. V. Craciun, D. Craciun, X. Wang, T. J. Anderson and R. K. Singh, Thin Solid Films **453** (2004) 256.
6. H. Agura, A. Suzuki, T. Matsushita, T. Aoki and M. Okuda, Thin Solid Films **445** (2003) 263.
7. H. Agura, H. Okinaka, S. Hoki, T. Aoki, A. Suzuki, T. Matsushita and M. Okuda, Electr. Eng. Jpn. **151** (2005) 40.
8. A. Suzuki, T. Matsushita, T. Aoki, A. Mori and M. Okuda, Thin Solid Films **411** (2002) 23.
9. A. Suzuki, T. Matsushita, T. Aoki, Y. Yoneyama and M. Okuda, Jpn. J. Appl. Phys., Part 2 **40** (2001) L401.
10. D. R. Sahu and J. L. Huang, Thin Solid Films **515** (2006) 876.
11. Douglas B. Chrisey and Graham K. Hubler; *Pulsed Laser Deposition of Thin Films*, John Wiley and sons Inc., New York (1994) chapter 8.
12. P. F. Carcia, R. S. McLean, M. H. Reilly, Z. G. Li, L. J. Pillione and R. F. Messier, J. Vac. Sci. Technol. A, Vac. Surf. Films **21** (2003) 745.

13. N. L. Dehuff, E. S. Kettenring, D. Hong, H. Q. Chiang, J. F. Wager, R. L. Hoffman, C. H. Park and D. A. Keszler, J. Appl. Phys. **97** (2005) 064505.
14. K. B. Sundaram and A. Khan, J. Vac. Sci. Technol. A, Vac. Surf. Films **15** (1997) 428.
15. K. Yim and C. Lee, Cryst. Res. Technol. **41** (2006) 1198.
16. P. J. Kelly and R.D. Arnell, Vacuum **56** (2000) 159.
17. P. J. Kelly, J. Hisek, Y. Zhou, R.D. Pilkington and R.D. Arnell, Surf. Eng. **20** (2004) 157.
18. P. J. Kelly, J. O'Brien and R.D. Arnell, Vacuum **74** (2004) 1.
19. E. M. Alkoy and P.J. Kelly, Vacuum **79** (2005) 221.
20. M. S. Hwang, H. J. Lee, H. S. Jeong, Y. W. Seo and S. J. Kwon, Surf. Coat.Technol. **171** (2003) 29.
21. I. Baia, M. Quintela, L. Mendes, P. Nunesa and R. Martins, Thin Solid Films **337** (1999) 171.
22. M.Mizuhashi, Thin Solid Films **70** (1980) 91.
23. K. D. J. Christian and S.R.Shatynski, Thin Solid Films **108** (1983) 319.
24. Y. Shigesato,Y.Hayashi and T.Haranoh, Appl.Phys.Lett. **61** (12992) 73.
25. H. U. Habermeier, Thin Solid Films **80** (1981) 157.
26. K. R. Babu, M. S. Mohan., M. Deepa. and K. G. Nair, Proc. of International Conference on Optoelectronic Materials and Thin film for Advanced Technology, Allied Publishers, (2005) pp 87.
27. K. E. Gonsalves, S. P. Rangarajan and J. Wang edited by Hari Singh Nalwa, *Nanostructured Materials and Nanotechnology,* Academic Press (2002) pp 3.

28. A. Rahm, M. Lorenz, T. Nobis, G. Zimmermann, M. Grundmann, B. Fuhrmann and F. Syrowatka, Appl. Phys. A **88** (2007) 31.
29. H. B. Zeng, W. P. Cai, B. Q. Cao, J. L. Hu, Y. Li and P. S. Liu Appl. Phys. Lett. **88** (2006) 181905.
30. Veeco Dektak 6M stylus profiler, Manual 2004.
31. P E J Flewitt and R K Wild, *Physical methods for materials characterisation*, IOP Publishing Ltd, (2003) pp 138.
32. Dieter K. Schroder, *Semiconductor material and device characterization,* A Wiley-intersciernce publication, (1998) pp 700.
33. A. Stefánsson, I. Gunnarsson and N. Giroud. *Anal. Chim. Acta* **582** (1) (2007) 69.
34. B. D. Cullity and S.R. Stock, *Elements of X ray diffraction,* Third edition, New Jersey, Prentice Hall (2001) pp 170.
35. M. J. Buerger, *X-ray Crystallography*, John Wiley & Sons, NewYork (1962) chapter 3.
36. C. Kittel, Introduction to Solid State Physics, Seventh edn, Wiley Eastern Limited, (1996) pp 29.
37. J. Bardeen, F. J. Blatt and L. H. Hall, Proceedings of Photoconductivity Conf. (1954, Atlantic City), (Eds) R. Breckenridze, B. Russel and T. Hahn, J.Wiley and Chapman and Hall, New York, 1956.
38. P. Kubelka and F. Munk, Zh.Tekh.Fiz. **12** (1931) 593.
39. P. Kubelka, J. Opt. Soc .Am, **38** (1948) 448.
40. D. R. Vij (Ed.) *Luminescence of solids*, Plenum Press, New York, (1998) chapter 3.

41. C. V. Raman and K. S. Krishna Nature **121** (1928) 501.
42. H. Richter, Z. P. Wang and L. Ley, Solid State Commun **39** (1981) 625.
43. Manual, Model H 50 MMR technologies Inc. California.
44. R. Manoj, P. Promodan, Johny Isaac and M. K. Jayaraj, proceedings of DAE solid state symposium, Gowaliar, December 2003, pp 249.

Chapter 3

Transparent p-$AgCoO_2$/n-ZnO heterojunction fabricated by pulsed laser deposition

Transparent p-n heterojunction on ITO coated glass substrates were fabricated using p-type $AgCoO_2$ and n-type ZnO films by pulsed laser deposition (PLD). The junction between p-$AgCoO_2$ and n-ZnO was found to be rectifying. The ratio of forward current to the reverse current was about 7 at 1.5V. The diode ideality factor was much greater than 2.

3.1. Introduction

The requirement for blue and UV emitters and detectors has aroused much interest in wide bandgap oxide semiconducting materials. Optically transparent oxides with larger band gap are intrinsically insulators. However materials like ZnO, In_2O_3, SnO_2 etc show high transparency for visible light and high electrical conductivity due to high electron concentration in the conduction band. These transparent conducting oxides (TCO's) find a wide range of applications. The use of TCO's in the fabrication of optoelectronic devices was not materialized due to the lack of TCO's exhibiting p-type conductivity. The low carrier mobility and density associated with narrow valance bands of these TCO's make it further difficult to obtain good p-type conduction required for device applications. The materials that are currently being investigated for the application of p-type TCO's are ABO_2 type of delafossites where A is the monovalent cation and B is the trivalent cation [1]. The p-type delafossite TCO thin films are all so far based on copper delafossites [2, 3]. Several strategies have been adopted to explore the possibilities of high quality TCO's in these delafossite materials in bulk and thin film form. These include varying the trivalent B cation and appropriate dopants and producing such materials based on silver rather than copper [4].

The first all-TCO diodes were reported by Sato et al. [5]. They fabricated a semi-transparent thin film of p-i-n structure consisting of p-NiO/i-NiO/i-ZnO/n-ZnO:Al. The thicknesses of the p-layer and n-layer were 195 and 400 nm, respectively. The rectifying properties of the structure confirmed the formation of the junction. They also tried to fabricate p-n diodes of the form p-NiO/n-ZnO:Al. But they observed linear I-V characteristics in both forward and reverse directions. Similarly, fabrication of all-TCO p-n hetero-junction thin film diode of the form p-$SrCu_2O_2$/n-ZnO was reported by Kudo et al. [6]. The same group also reported UV emission

from a p-n hetero-junction diode composed of p-$SrCu_2O_2$/n-ZnO after current injection through it [7-10]. p-i-n hetero-junction in the form of p-$SrCu_2O_2$:K/i-ZnO/n-ZnO was also constructed by this group [9]. A p-i-n hetero-junction with the structure p-$CuYO_2$:Ca/i-ZnO/n-ITO was fabricated by Hoffman et al. [11]. Lattice matching is one of the most important requirements for realizing rectifying junctions. In most of the reports on the p-n hetero-junctions published so far, n-ZnO and p-$SrCu_2O_2$ were used as the n and p-layers, respectively, because of lattice matching between them. Also the low deposition temperature (~350^oC) of $SrCu_2O_2$ made it possible to minimize the chemical reaction at the $SrCu_2O_2$-ZnO interface. Lastly, carrier concentration in ZnO can be controlled easily by varying the O_2 partial pressure during deposition in order to match the hole concentration in $SrCu_2O_2$ [6,8,9]. Jayaraj et al. [12] fabricated p-n hetero-junction using p-$CuY_{1-x}Ca_xO_2$/n-$Zn_{1-x}Al_xO$ structure. They observed rectifying I-V characteristics with a turn-on voltage between 0.4 and 0.8 V. Rectifying behaviour in oxide based homojunctions has also been reported, including n-ZnO/p-ZnO [13] and n-$CuInO_2$/p-$CuInO_2$ structures [14]. This chapter presents the electrical characteristics of all oxide transparent p-n heterojunction fabricated using $AgCoO_2$ as p-type TCO on glass substrates.

3.2. Experimental

The transparent heterojunctions fabricated in this study had a structure of glass/ITO/n-ZnO/p-$AgCoO_2$/In, which is schematically depicted in figure 3.1. The 2.5 cm x 2.5 cm glass substrate coated with 200 nm thick indium tin oxide (ITO) film with conductivity ~ 10^4 Scm^{-1} was used as a substrate. The p-n junctions were fabricated using undoped ZnO as the n-type semiconductor while $AgCoO_2$ as the p-type semiconductor. The different layers of thin films of transparent heterojunction were deposited by

using a multicarousal pulsed laser deposition (PLD) system. The third harmonic of a Q-switched Nd: YAG laser operating at 355 nm with a repetition rate of 10 Hz and pulse width of 9 ns was used for ablation of the targets. The $AgCoO_2$ target was prepared by pelletizing polycrystalline $AgCoO_2$ powder prepared in-house by hydrothermal reaction of $AgNO_3$, Co_3O_4 and KOH in a parr bomb at 250^oC. The as prepared pellet was sintered at 350^oC for 5 hours in air.

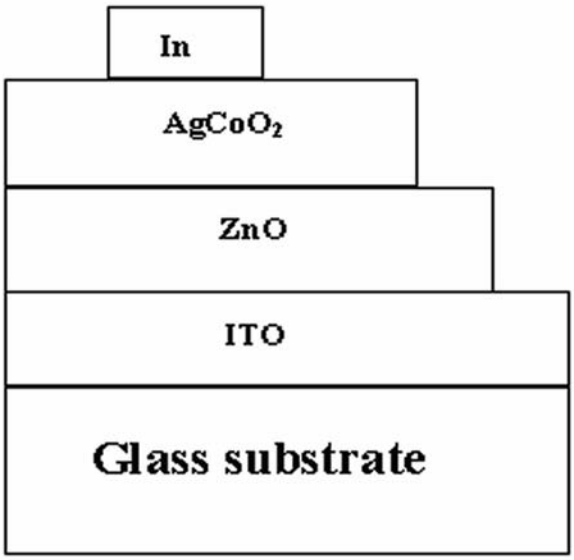

Figure 3.1 Structure of the p-n junction.

All the depositions were carried out at an oxygen pressure of 10^{-4} mbar and target to substrate distance kept at 5.5 cm. The silver delafossite compound decomposes at temperature ~ 600^oC. The trials to deposit $AgCoO_2$ on suphire substrates at higher substrate temperature resulted in the secondary phases of Ag_2O. The growth parameters like substrate temperature and energy density for $AgCoO_2$ thin films were fixed at 300^oC

for and 1 J/cm^2 respectively. For ZnO, laser energy density 2 J/cm^2 was used and the substrate temperature was kept at 400^{o}C.

The target was continuously rotated during the deposition to ensure uniform pitting and ablation. The thickness of these films was ~200 nm as measured by surface profilometer. The crystalline structure of the $AgCoO_2$ bulk target and thin film were analyzed using an X-ray diffractometer (Rigaku) using Cu-K_α radiation (1.5414 Å). The surface morphology and microstructure of the grown films were studied using transmission electron microscope (TEM) and high resolution transmission electron microscope (HRTEM) model JEM-2010 UHR of JEOL at an operating voltage of 200 keV. For TEM analysis, the films were directly coated on carbon coated copper grid. Transmission spectra of the films in the UV-visible spectral region were recorded using JASCO V 570 UV-VIS-NIR spectrophotometer.

3.3. Results and discussion

3.3.1. Structural characterization

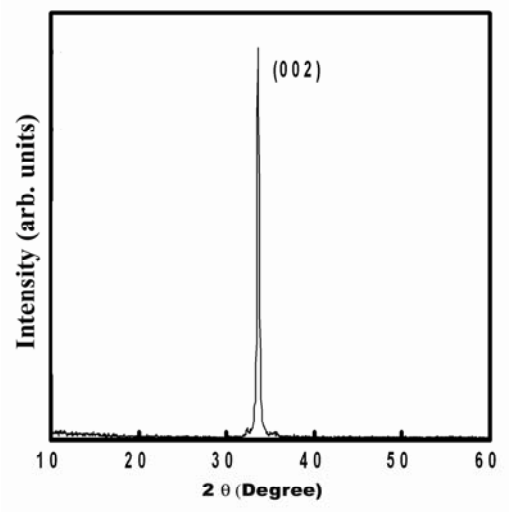

Figure 3.2. X-ray diffraction pattern of ZnO thin film.

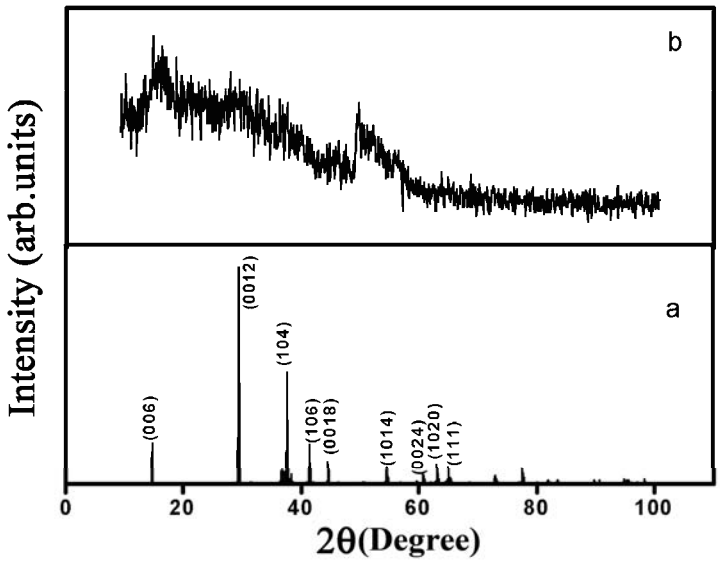

Figure 3.3. X-ray diffraction pattern of (a) $AgCoO_2$ target and (b) $AgCoO_2$ thin film.

The XRD pattern of ZnO thin film grown by PLD on glass substrate is shown in figure 3.2. This revealed the highly crystalline and preferentially [002] oriented growth of the ZnO films. Figure 3.3 (a) & (b) show the x-ray diffraction pattern of the $AgCoO_2$ target used for the ablation and a 200 nm thick $AgCoO_2$ film coated on glass substrate. The X-ray diffraction pattern of $AgCoO_2$ target shown in figure 3.3 (a) showed 6H polytype of $AgCoO_2$. No peaks corresponding to other polytypes were detected and all the observed peaks could be indexed by assuming a hexagonal 6H polytype structure [15]. However the observed diffraction pattern could be accounted for as a mixture of 2H and 3R forms rather than an actual 6H delafossite structure, a situation commonly observed in delafossite compounds. The diffraction pattern of $AgCoO_2$ film is featureless, except for a few humps probably due to the short range ordering present in the $AgCoO_2$ lattice, indicating nearly amorphous growth of $AgCoO_2$ film on glass substrate. The HRTEM of the $AgCoO_2$ films having thickness ~16 nm, grown under the

same deposition conditions but on the carbon coated copper grids is shown in figure 3.4. The atomic scale images showed parallel lines of ions at intervals of ~2.03 Å. This value of lattice spacing coincides with d spacing of $AgCoO_2$ (0018) planes observed from powder diffraction.

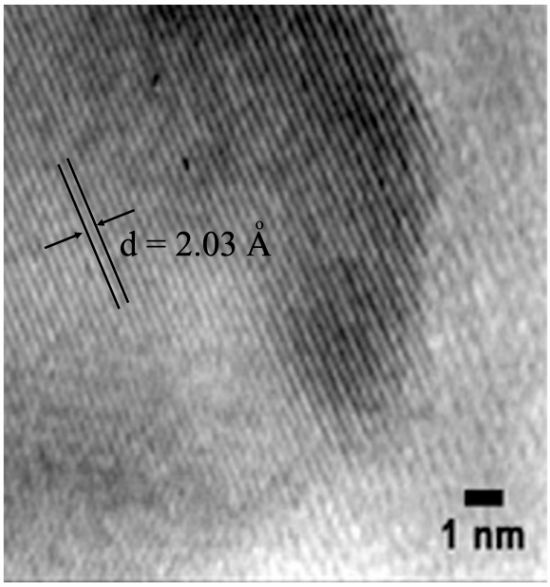

Figure 3.4. HRTEM of $AgCoO_2$ thin film grown on carbon coated copper grid representing (0018) planes with d spacing 2.303 Å.

3.3.2. Optical studies

The transmission spectra of ZnO and $AgCoO_2$ thin films are shown in figure 3.5. The average transmission of ZnO and $AgCoO_2$ thin film was ~ 85 and 55% respectively in the visible spectral region. From $(\alpha h\nu)^2$ vs. $h\nu$ plots, where α is the absorption coefficient and $h\nu$ denotes the photon energy, as shown in figure 3.6 and 3.7, the optical band gap at room temperature of ZnO and $AgCoO_2$ thin films were estimated to be ~ 3.28eV and 3.89 eV respectively. The band gap of the $AgCoO_2$ powder was

estimated from the diffuse reflectance spectrum using $((k/s)\ h\nu)^2$ vs. $h\nu$ plot, where $h\nu$ is the photon energy and k & s denote the absorption and scattering coefficients respectively. The ratio (k/s) can be calculated from the reflectance spectra using the Kubelka-Mank equation [16, 17]. This plot is shown in the inset of figure 3.7. From this plot the band gap of the $AgCoO_2$ powder was found to be ~3.96 eV.

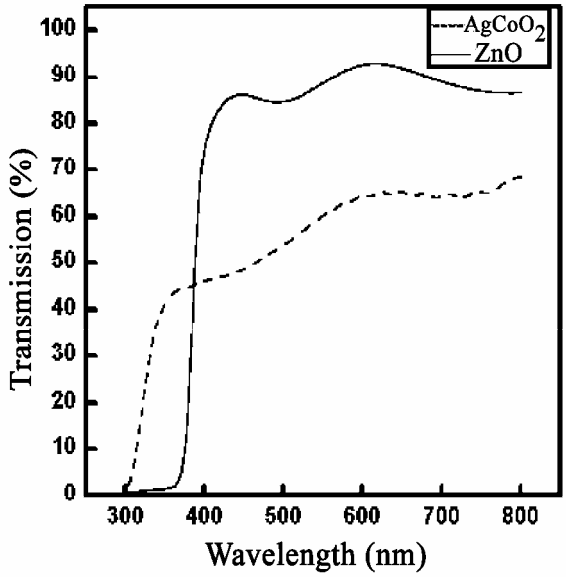

Figure 3.5 Transmission spectra of $AgCoO_2$ and ZnO thin films.

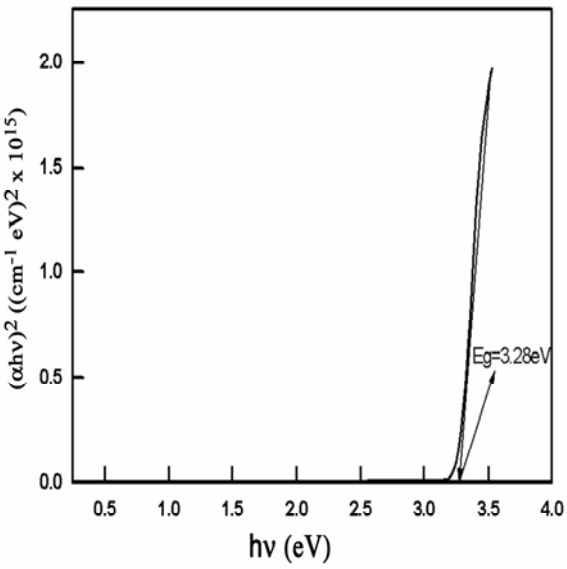

Figure 3.6 $(\alpha h\nu)^2$ vs. hν plot of ZnO thin film.

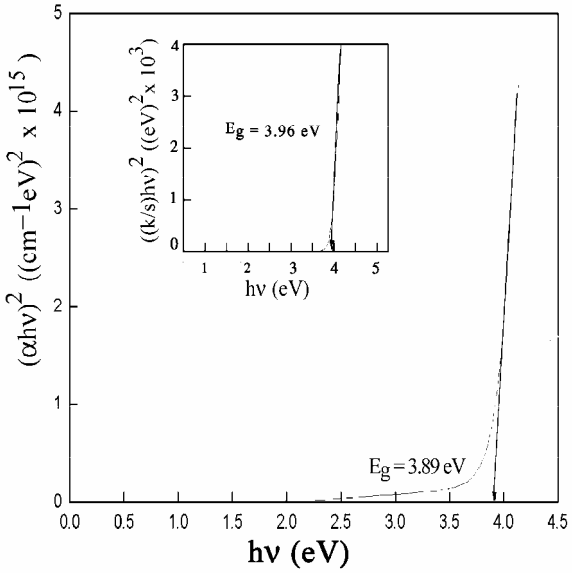

Figure 3.7 $(\alpha h\nu)^2$ vs. hν plot of $AgCoO_2$ thin film and inset shows the $((k/s)h\nu)^2$ vs. hν plot of $AgCoO_2$ powder.

3.3.3. Electrical characterization

The room temperature electrical measurements of both the ZnO and $AgCoO_2$ thin films grown on glass substrate were carried out by four probe technique with van der Pauw configuration in Hall geometry. Indium metal was used to make electrical contacts. The ohmic nature of these contacts was confirmed with current-voltage (I-V) measurements which showed linear behavior. For the ZnO films grown on glass substrates the carrier concentration and Hall mobility at room temperature were found to be ~ 4.6 x 10^{19} cm^{-3} and ~ 40.27 $cm^2V^{-1}s^{-1}$ respectively. The measured resistivity of the PLD grown $AgCoO_2$ thin film on glass was found to be ~1.14 x 10^3 ohm-cm. The effort to measure the carrier type and their concentration in $AgCoO_2$ films did not succeed due to the observation of unpredictable dependence of Hall voltage on the magnitude and direction of the applied magnetic field. The Hall voltage showed nonlinear behavior as a function of applied magnetic field and did not change sign with reversing the direction of applied magnetic field. Such an electrical behavior has also been reported by p-type TCO's other than $AgCoO_2$ and has been largely attributed to mixed conduction. This may be either due to the nearly same values of donar density (N_d) and acceptor density (N_a) or to the limitation posed due to the large width of the depletion region. However the p-type conduction in $AgCoO_2$ film was confirmed by the thermoelectric power measurements which showed the seebeck coefficient of ~ +230 μVK^{-1}.

Figure 3.8 shows a typical current density-voltage (J-V) characteristic of the p-$AgCoO_2$/ n-ZnO hetero-junction structure. The characteristics showed the rectifying nature of this hetero-junction with a typical forward to reverse current ratio of ~7 in the range of –1.5 to +1.5 V. The turn-on voltage of the heterojunction was found to be ~ 0.75 V. The turn on voltage, also identified as the diffusion or built in potential, would

correspond to a potential barrier such that carrier has to overcome in order to contribute to forward current [18]. The n-type ZnO layer grown by PLD was crystalline and the $AgCoO_2$ p layer was nearly amorphous. This could lead to structural imperfections at grain boundaries and at the interface, which could lead to the deterioration of the diode quality. It is well known that the conductivity of the n-ZnO layer is mainly due to the oxygen deficiency where as in $AgCoO_2$, the excess oxygen is responsible for inducing p-type conductivity. The $AgCoO_2$ was deposited on the ZnO layer under oxygen ambient, which may result in a very thin mixed intrinsic layer between n-ZnO and p-$AgCoO_2$. The diode ideality factor was determined from the slope of the forward bias lnI vs. V curve [19] using the equation given by

$$n = \frac{q}{kT}\frac{dV}{d\ \ln\ I} \qquad (3.1)$$

where k is the Boltzmann constant and dV/dlnI is the inverse slope of lnI vs. V curve, which is shown in figure 3.9. The diode did not conform to the normal forward bias I-V relationship in which the current depends exponentially on the voltage divided by a product of thermal energy times an ideality factor n =1 or 2. At very small voltages the ideality factor was n = 5 and it increased as the voltage increased.

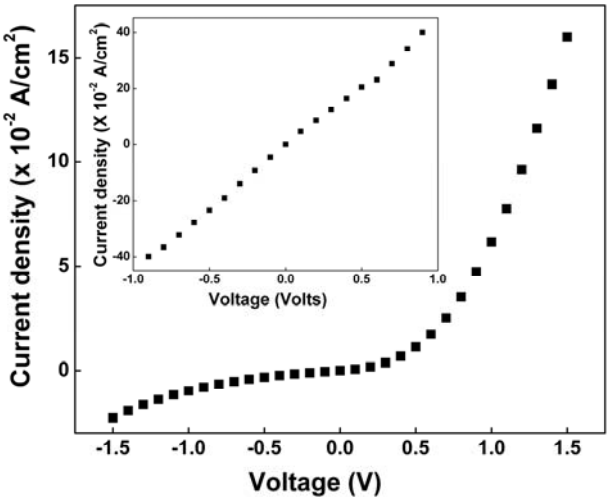

Figure 3.8 Current density - Voltage (J-V) characteristics of $AgCoO_2$/ZnO p-n junction diode and inset shows the J-V characteristics of ZnO/ITO contact.

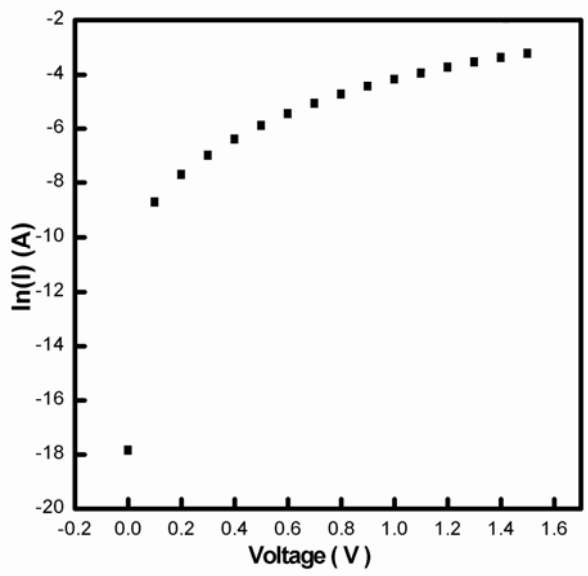

Figure 3.9 ln (I) vs. V plot for determining the ideality factor.

According to Sah-Noyce Shockley theory [20] in a p-n junction, the ideality factor is 1 at low voltage and 2 at high voltage. The high value of the ideality factor could then be attributed to the presence of non-linear metal semiconductor contact. According to Wang et al [21] the heterojunction diode can be modeled in different bias voltage ranges by a series of diodes or resistances: the actual p-$AgCoO_2$/n-ZnO heterojunction and the metal semiconductor contact resistances. Eventhough the metal semiconductor junctions of a diode ideally have ohmic characteristics (inset of figure 3.8), contacts could exhibit non-linear characteristics. In the limit of high contact resistance the metal-semiconductor contact could be considered as a resistance in the low and high voltage range and a reverse bias Schottky contact in the interim voltage range. According to Sha-Li-Schubert Model [22], the ideality factor of the device is the sum of the ideality factors of the individual rectifying junctions and may lead to ideality factors much greater than 2.

3.4. Conclusion

A transparent p-n heterojunction was fabricated using p-$AgCoO_2$ and n-ZnO layers deposited on glass substrate using pulsed laser deposition. Rectifying behaviour was observed in the junction with a turn on voltage of 0.75 volt. Diode ideality factor was found to be much greater than 1, which could be attributed to the non-linearity of the metal semiconductor contacts in the device.

3.5. References

1. N. Duan, A. W. Sleight and M. K. Jayaraj, J. Tate, Appl. Phys. Lett. **77** (2000) 1325
2. H. Kawazoe, M. Yasukawa, H. Hyodo, M. Kurita, H. Yanagi and H. Hosono, Nature **389** (1997) 939.
3. M. S. Lee, T. Y. Kim and D. Kim, Appl. Phys. Lett. **79** (2001) 2028.
4. J. Tate, M. K. Jayaraj, A. D. Draeseke, T. Ulbrich, A. W.Sleight, K. A. Vanaja, R. Nagarajan, J. F. Wager and R. L. Hoffman, Thin Solid Films **411** (2002) 119.
5. H. Sato, T. Minami, S. Takata and T. Yamada, Thin Solid Films **236** (1993) 27.
6. A. Kudo, H. Yanagi, K. Ueda, H. Hosono, H. Kawazoe and Y. Yano, Appl. Phys. Lett. **75** (1999) 2851.
7. H. Ohta, K. Kawamura, M. Orita, N. Sarukura, M. Hirano and H. Hosono, Electron. Lett. **36** (2000) 984.
8. H. Ohta, K. Kawamura, M. Orita, M. Hirano, N. Sarukura and H. Hosono, Appl. Phys. Lett**. 77** (2000) 475.
9. H. Ohta, M. Orita and M. Hirano, J. Appl. Phys. **89** (2001) 5720.
10. H. Hosono, H. Ohta, K. Hayashi, M. Orita and M. Hirano, J. Cryst. Growth **237** (2002) 496.
11. R. L. Hoffman, J. F. Wager, M. K. Jayaraj and J. Tate, J. Appl. Phys **90** (2001) 5763.
12. M.K. Jayaraj, A.D. Draeseke, J. Tate and A.W. Sleight, Thin Solid Films **397** (2001) 244.
13. T. Aoki, Y. Hatanaka and D. C. Look, Appl. Phys. Lett **76** (2000) 3527.

14. H. Yanagi, T. Hase, S. Ibuki, K. Ueda and H. Hosono, Appl. Phys. Lett. **78** (2001) 1583.
15. J. S. Kang, J. H. Kwak, Y. J. Shin, S. W. Han, K. H. Kim and B. I. Min, Phys. Rev. B. **61** (2000) 10682.
16. P. Kubelka and F. Munk, Zh. Tekh. Fiz. **12** (1931) 593.
17. P. Kubelka, J. Opt. Soc. Am. **38** (1948) 448.
18. S. M. Sze, Physics of semiconductor devices, John Wiley and Sons, Newyork (1981) Chapter 2
19. D. K. Schroeder, Semiconductor Material and Device Characterisation, Wiley, NewYork. (1990) pp 202.
20. C. Sah, R. N. Noyce and W. Shockley, Proc. IRE. **45** (1957) 1228.
21. C. X. Wang, G. W. Yang, H. W. Liu, Y. H. Han, J. F. Luo, C. X. Gao and G. T. Zou, Appl. Phys. Lett. **84** (2004) 2427.
22. J. M. Sha, Y. L. Li, T. Gessmann and E. F. Schubert, J. Appl. Phys. **94** (2003) 2627.

Chapter 4

Electrical characteristics of n-ZnO/p-Si heterojunction diodes grown by pulsed laser deposition

Heterojunction diodes of n-type ZnO/p-type silicon (100) were fabricated by pulsed laser deposition of ZnO films on p-Si substrates in oxygen ambient at different pressures. Turn-on voltage of the heterojunctions was found to depend on the ambient oxygen pressure during the growth of the ZnO film. The current density-voltage characteristics and the variation of the series resistance of the n-ZnO/p-Si heterojunctions were found to be in line with the Anderson model and Burstein-Moss (BM) shift.

4.1. Introduction

Currently there is significant interest in ZnO as a candidate for various futuristic optoelectronic devices. ZnO is a rugged semiconductor with direct wide band-gap and it exhibits significant n-type conductivity even without any intentional doping. This n-type conductivity can be further enhanced by doping it with Al or Ga [1-3]. This property and the transparency in the visible spectral region have prompted extensive investigations of ZnO films as transparent electrodes in flat-panel displays [4], p-n heterojunction diode [5-7], thin film transistors [8], multiple quantum well structures [9] and solar cells [10]. We have fabricated ZnO based all transparent conducting p-n heterojunction diodes with p-type $AgCoO_2$ [11,12]. Albeit ZnO films can be grown by a variety of methods, including radio-frequency (rf) and direct-current (dc) sputtering [3,13,14], chemical vapor deposition [15], spray pyrolysis [16], electron cyclotron resonance-assisted molecular beam epitaxy [17], we used pulsed laser deposition (PLD) [1,18,19] to deposit high quality ZnO films because of its effectiveness and amenability to different growth conditions [20]. For the present study we fabricated heterojunctions of n-type ZnO on p-type Si, which has many advantages such as low cost, large wafer size and possibility of integrating oxide semiconductors with already highly matured silicon technology.

The growth of ZnO on Si substrates has been studied extensively including the epitaxial growth of ZnO on Si (100) substrates [21], ZnO/p-Si diodes [22-24], ZnO:N/p-Si heterostructures [25] etc. Studies on the electrical transport properties of ZnO/p-Si heterojunctions with different dopands in p-Si [26] and ZnO [27] have also been reported recently. However, due to the complex nature of the carrier transport across the interfaces of n-ZnO /p-Si

heterojunction, transport properties of these heterostructures are not yet well understood and even debatable. We have furthered these studies on n-ZnO/p-Si heterojunction diodes fabricated by pulsed laser deposition at different oxygen pressures. These heterojunction diodes are found to have highly favorable forward to reverse current ratio. We have also studied the parametric dependence of the electrical characteristics of these heterojunctions. The results of these studies are presented and discussed in this chapter.

4.2. Experimental

The pulsed laser deposition (PLD) of the ZnO films was carried out in a growth chamber, which was first evacuated to a base pressure of 10^{-6} mbar. Polycrystalline, stoichiometric, sintered (for 5 hours at 1200^{o}C) pellet of ZnO with a purity of 99.999 % was used as the target for PLD. The third harmonics (355 nm) of a Q-switched Nd: YAG laser with repetition rate of 10 Hz, pulse width of 9 ns and fluence of about 3 J/cm^2 per pulse was used for ablation of the ZnO target. P-type silicon wafers with (100) orientation and carrier concentration 1 x 10^{15} cm^{-3} were used as substrates. The silicon substrates were degreased in trichloroethylene (TCE), rinsed in de-ionized water, etched in a mixture of HF and H_2O (1:1) at room temperature for 5 minutes, and rinsed in TCE again. The growth chamber was filled with flowing oxygen ambient and its pressure was varied from 0.003 to 0.007 mbar during the growth of different samples. The substrate to target distance was kept about 4.5 cm. The ZnO films were deposited for about 30 minutes on the Si substrates at room temperature. To measure the conductivity and band gap of the ZnO films, those were

separately deposited on silica substrates under the identical experimental conditions as those used for the growth on the Si substrates. For electrical measurements, indium metal contacts were made on both p-type silicon surface and n-type ZnO films, which were found to be ohmic in nature. The room temperature electrical measurements of the ZnO thin films grown on the silica substrates were carried out using four probe van der Pauw configuration in hall geometry.

4.3. Results and discussion

Thickness of the deposited ZnO films, measured using a stylus profiler (Dektak 6M Stylus profiler) was found to be about 250 nm. X-ray diffraction pattern of all the ZnO films showed only (002) peaks along with that of the Si (200) peak. A typical XRD pattern of these films is shown in figure 4.1(a). This confirmed a highly c-axis oriented growth of the ZnO films. The full width at half maximum (FWHM) of the (002) x-ray diffraction peak of the ZnO films was found to be about 0.34^{o}, indicating reasonably good crystalline quality of these films. X-ray diffraction pattern of the ZnO films deposited on the silica substrates is shown in figure 4.1(b). This also showed only a (002) peak of ZnO confirming the same c-axis oriented growth as in the case of ZnO films grown on p-Si substrates. However the FWHM of this peak was found to be about 0.36^{o}, which is slightly higher than that of the films grown on the Si substrates as expected.

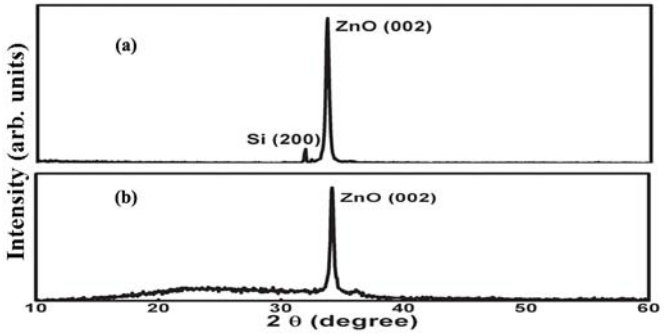

Figure 4.1 XRD pattern of ZnO films deposited on (a) p-silicon (100) and (b) silica substrates.

Figure 4.2 shows the $(\alpha h\nu)^2$ vs. $h\nu$ plot of ZnO films grown on silica substrates at different oxygen pressures. Figure 4.3(a) shows the variation of band gap of the ZnO thin films grown on silica substrates, estimated from $(\alpha h\nu)^2$ vs. $h\nu$ plot. It can be seen from this figure that the band gap decreased from 3.36 to 3.257 eV with increase of oxygen pressure from 0.003 to 0.007 mbar. Series resistance, an inherent resistance of the depletion region in n-ZnO/p-Si heterojunction of all the diodes grown at different oxygen pressures was calculated from log (I) vs. V plots [28], which is also shown in figure 4.3(a). As can be seen in this figure the series resistance increased from 3.45×10^5 to 5.6×10^5 ohm with increasing oxygen partial pressure from 0.003 to 0.007 mbar. Figure 4.3(b) the variation of resistivity and the electron mobility for the ZnO thin films with respect to the oxygen pressure. It can be seen from this figure that while the resistivity increased, the mobility decreased when the oxygen pressure used during the deposition was increased. The hall measurements confirmed the n-type conductivity of the ZnO films.

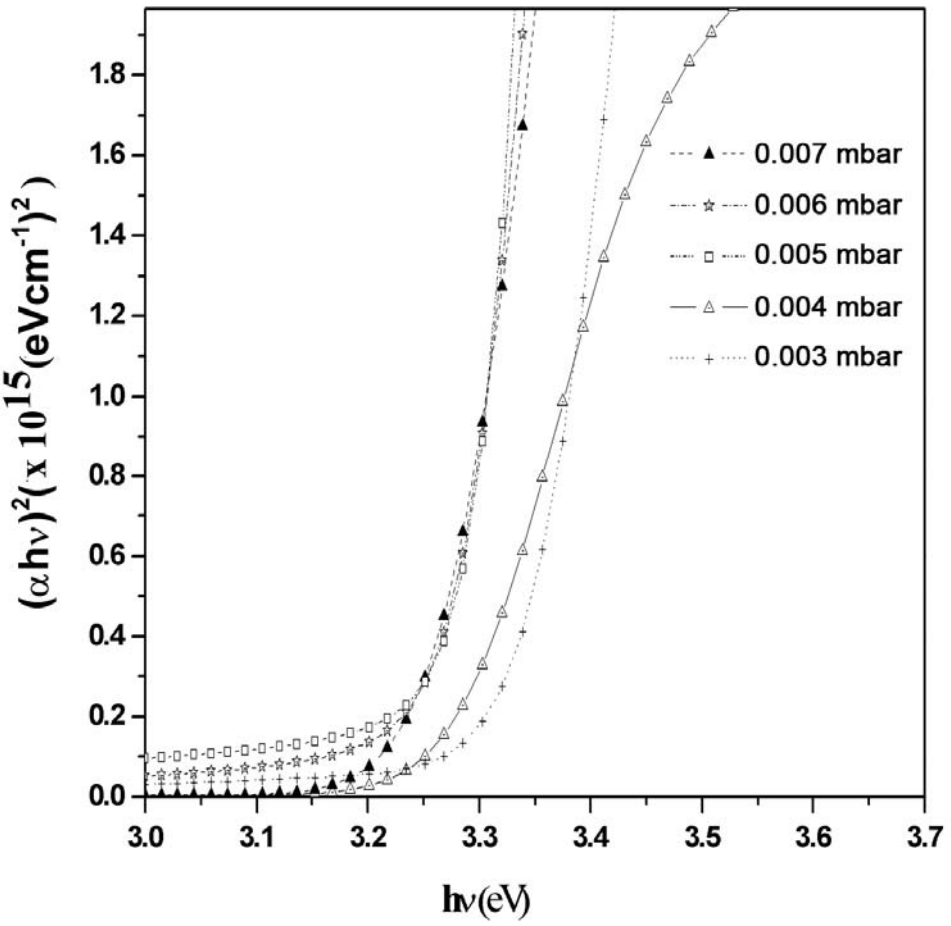

Figure 4.2 The (αhν) vs. hν plot of ZnO films grown on silica substrates at different oxygen pressures.

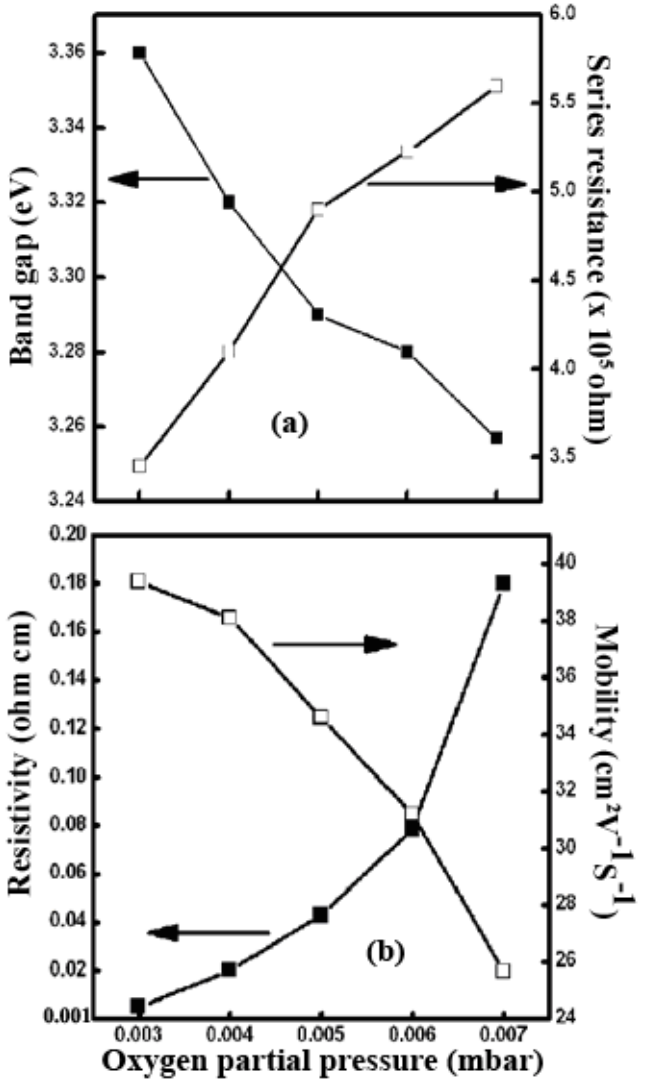

Figure 4.3 (a) The series resistance and the optical band gap variation with oxygen pressure and 2 (b) the plot of resistivity and mobility with oxygen pressure.

Using these Hall measurements, the carrier concentration was found to decrease from about 3.2 x 10^{19} cm^{-3} to 1.32 x 10^{18} cm^{-3} when the oxygen pressure was increased from 0.003 mbar to 0.007 mbar, which is shown in figure 4.4. A theoretical curve based on the calculated values of the carrier concentration from the Burstein-Moss (BM) shift [29] is also shown in this figure. With a small gap between the two curves, the trend of experimental data and that of the calculated ones coincide reasonably well.

As seen from figure 4.3(a) band gap of the ZnO films decreased with increase of the oxygen pressure during their growth and so did the electron concentration. This means the films grown at lower oxygen pressure had higher band gap due to the enhanced carrier concentration in the film. Increase in the band gap accompanied by the enhanced carrier concentration can be explained using the BM shift [29]. As it is well known, this model relies on effective mass approximation (EMA), the wave functions are represented by plane waves and conduction band and valance band are taken to be parabolic near the Brillouin zone. The BM shift in band gap, ΔE_g according to this model [29] is given by:

$$\Delta E_g = \frac{h^2}{8\pi^2}\left(\frac{1}{m_e}+\frac{1}{m_h}\right)\left(3\pi^2 n\right)^{2/3} \qquad (4.1)$$

where m_e = 0.28 m_e, m_h = 0.59 m_e, are the effective electron mass, effective hole mass; h and n are Planck constant and electron density per unit volume respectively.

This leads to a total band gap of

$$E_g = E_{go} + \Delta E_g \qquad (4.2)$$

We took the band gap of ZnO without BM shift as E_{go}= 3.25 eV, which is that of the ZnO bulk crystal at room temperature [30]. BM shift in band gap (ΔE_g) was obtained from equation (4.2) using the total band gap (E_g) estimated from the optical transmission spectra. Then electron concentrations (n) were calculated using the equation (4.1). These calculated values of electron concentrations are plotted as a function of the oxygen partial pressure in figure 4.4.

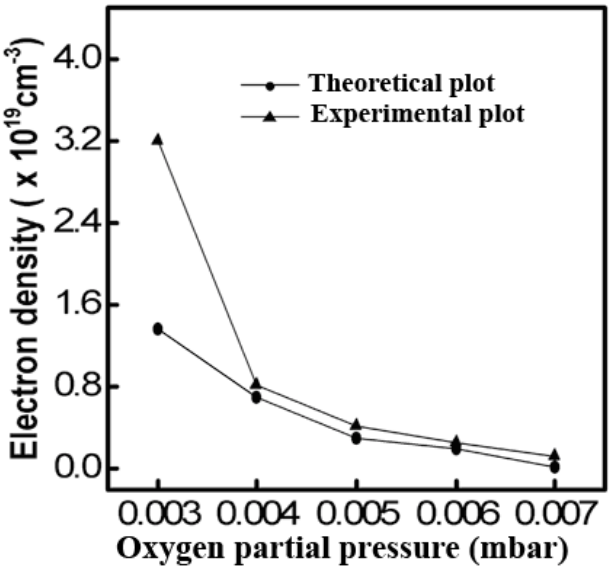

Figure 4.4 The variation of electron concentration in ZnO films (obtained from the Hall measurement and theoretical model using BM shift) with oxygen pressure.

Experimental values of the electron concentrations obtained from the Hall measurements are also shown in figure 4.4. It can be seen in this figure that the electron concentrations obtained from Hall measurements match well with those obtained from the theoretical BM shift except for the lowest oxygen pressure. This might be due to the strain resulting from the increased oxygen vacancies in the film. Values of series resistance of the p-Si/ZnO heterojunctions, electron density (both calculated and experimentally observed) and band gap ZnO films are summarized in the table 4.1.

Table 4.1 The values of various observed and calculated parameters.

Variation of Oxygen pressure (x 10^{-3} mbar)	Band gap (eV) calculated from absorption spectra	Electron density from Hall measurements (cm^{-3} x 10^{19})	Electron density calculated using BM shift (cm^{-3} x 10^{19})	Series resistance across the P-Si/ZnO heterojun-ction (x 10^{5} ohm)
7	3.26	0.13	0.072	5.6
6	3.28	0.256	0.19	5.2
5	3.29	0.421	0.3	4.9
4	3.32	0.81	0.69	4.1
3	3.36	3.2	1.36	3.45

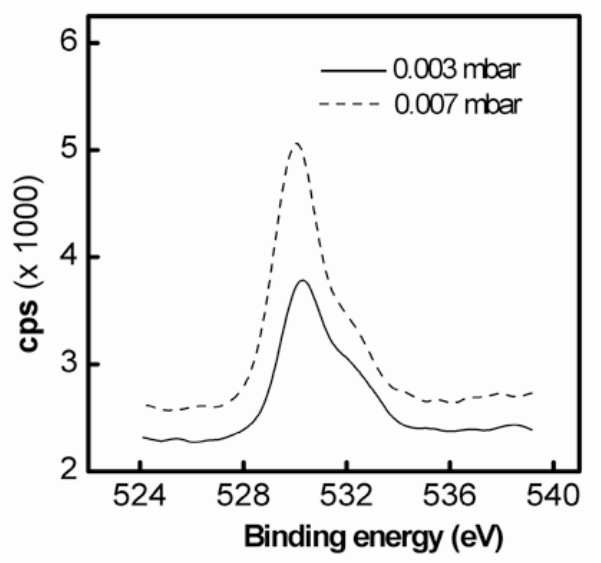

Figure 4.5. XPS of O 1s ZnO thin films deposited at 0.007 mbar and 0.003 mbar oxygen pressures.

The physical basis for the concentration of oxygen incorporation in the ZnO films was investigated by x-ray photoelectron spectroscopy (XPS) of the films grown at oxygen pressures 0.003 and 0.007 mbar using Al K_α radiation source (1486.6 eV). The results are shown in figure 5. XPS of oxygen 1s peak intensity shows higher oxygen incorporation in the ZnO films grown at 0.007 mbar of oxygen pressure. It was also observed from the XPS data that increase of oxygen pressure during deposition enhanced the O/Zn ratio in the ZnO thin films. From the XPS and Hall measurement data it can be elicited that more the oxygen incorporation in the films lesser the electron concentration. This is also in conformation with the earlier study of Look et al [31].

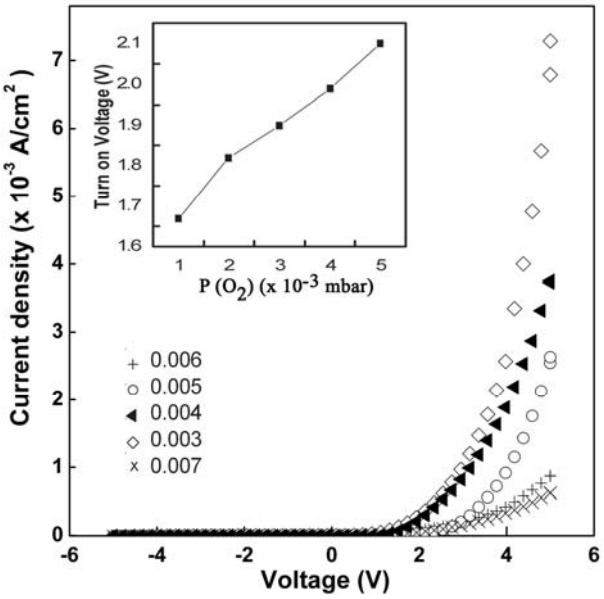

Figure 4.6 Current density–voltage (J-V) plot of ZnO/p-Si heterojunctions. Inset shows the variation of turn on voltage with oxygen pressure (p (O_2)).

Figure 4.6 shows the J-V characteristics of five different n-ZnO/p-Si heterojunctions with ZnO films grown at different oxygen pressures. All the five heterojunctions were found to be rectifying and the turn-on voltage of the heterojunctions increased as shown in the inset of figure 4.6 with increase of oxygen pressure during the growth of the ZnO films. J-V characteristics of the n-ZnO/p-Si heterojunction diode with the lowest turn-on voltage is plotted on a logarithmic scale, which is shown in figure 4.7. Maximum forward to reverse current ratio is found to be about 1000 in the range of the applied voltage from -5 V to +5 V. Inset of the figure 4.7 shows the ohmic nature of In/ZnO contact.

Room temperature leakage current at -5 V is of the order of 10^{-7} A. The ideality factor was found to be greater than 10 for all the heterojunctions fabricated.

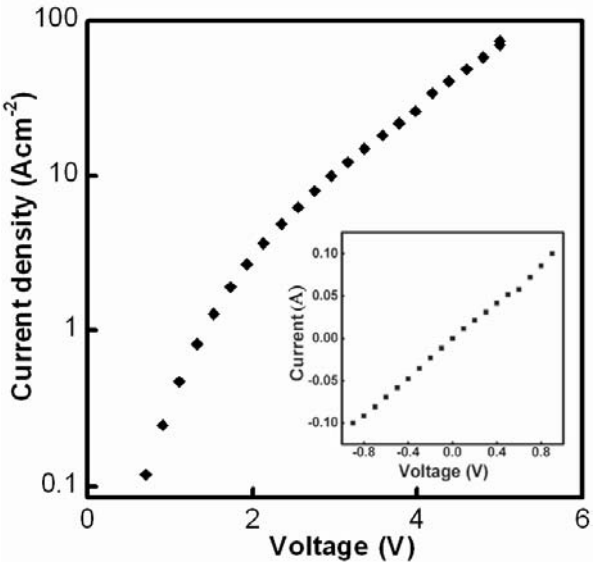

Figure 4.7 Current density–voltage (J-V) plot of ZnO/p-Si heterojunctions on logarithmic scale. Inset shows the current-voltage (I-V) plot of In/ZnO contact.

Band structure of n-ZnO/p-Si at the heterojunction can be constructed using Anderson model [32] by assuming continuity of vacuum levels, neglecting the effects of dipole and interfacial states. Similar band structure has been suggested for doped and pure ZnO/Si heterojunction by P Chen et al [26,33]. Figure 4.8(a) and 4.9 show the constructed band structure of n-ZnO/p-Si heterojunction fabricated at 0.007 mbar oxygen pressure under zero bias and forward bias respectively. Values of band gaps E_g (ZnO) = 3.257 eV and E_g (Si) = 1.12 eV, electron affinities, χ (ZnO) = 4.35 eV and χ (Si) = 4.05 eV were

used [26]. Valance band offset (ΔE_v) and conduction band offset (ΔE_c) are equal to 2.43 eV and 0.3 eV respectively. Variation of ΔE_v with oxygen pressure during PLD of ZnO films is shown in the figure 4.8(b). Both ΔE_v and ΔE_c are emerging out of the difference in the electron affinities and band gaps of two materials forming the junction. It can be noted that valance band offset ΔE_v is much higher than conduction band offset ΔE_c.

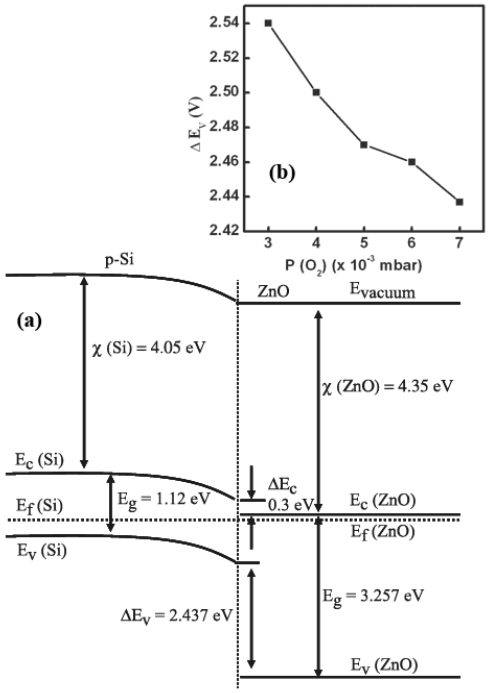

Figure 4.8 (a) The band structure of ZnO/p-Si heterojunction (grown at 0.007 mbar oxygen pressure) under zero bias and (b) shows the variation of ΔE_v with oxygen pressure during PLD of ZnO films.

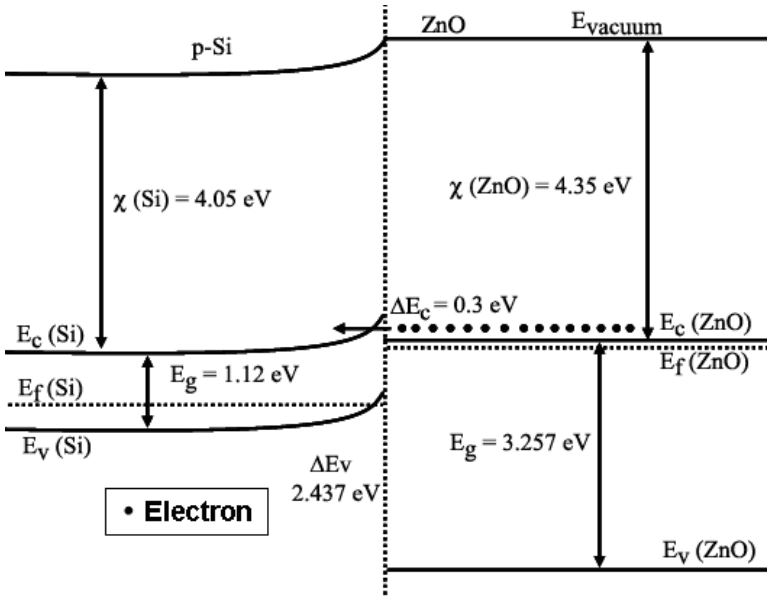

Figure 4.9 The band structure of ZnO/p-Si heterojunction (grown at 0.007 mbar oxygen pressure) under forward bias.

Since carrier concentration in the p-Si side is about 3 orders of magnitude lower than that in ZnO side, all the depletion region within the p-Si/ZnO heterojunction is extended into the p-Si side. Figure 4.8(a) shows that bottom of the conduction band on the ZnO side lies quite lower in energy than that on the p-Si side. Hence under relatively low forward bias, chance of electron flow from ZnO side to the p-Si side is negligible due to the higher barrier difference felt by the electrons in the bottom of the conduction band on the ZnO side. This resulted in higher turn-on voltage for p-Si/ZnO junction grown at 0.007 mbar of oxygen pressure. But under higher forward bias, the barrier difference lowered and the injection of electrons from the bottom of the conduction band on the ZnO side to the p-Si increased considerably (as shown in figure 4.9). Thereby forward current increased rapidly

under higher voltage bias. When the oxygen pressure during the deposition of ZnO decreased, carrier concentration increased and hence Fermi level shifted towards the bottom of the conduction band. That means upon the decrease of oxygen pressure, Fermi level may even get into the conduction band and result in the ease of flow of electrons from ZnO side to p-Si side. Hence forward voltage required for considerable forward current decreased and there by turn-on voltage decreased. This seems to explain the decrease of the turn-on voltage for the n-ZnO/p-Si heterojunction fabricated at the lower oxygen pressure.

Variation of turn-on voltage with oxygen pressure can also be explained with calculated values of series resistance. Due to series resistance, effectively a part of the applied voltage is dropped and hence larger applied voltage is necessary to achieve the same level of current compared to the ideal one. Hence the turn-on voltage will be increasing with the increase of series resistance in the quasineutral region of p-Si/ZnO. It is noticed that calculated values of series resistance thus obtained increased with increase of oxygen pressure and thereby increasing the turn-on voltage.

4.4. Conclusion

In conclusion c-axis oriented crystalline ZnO films deposited on p-type Si (100) at different oxygen pressures using PLD form effective n-ZnO/ p-Si heterojunctions, which were found to be rectifying. Maximum forward to reverse current ratio was found to be 1000 in the applied voltage range from -5 V to +5 V. Variation of the turn-on voltage with oxygen pressure was modeled with Anderson model and BM shift which is in conformity with the values of series resistance calculated across the n-ZnO/p-Si heterojunction.

4.5. References

1. D. C. Look, D. C. Reynolds, C. W. Litton, R. L. Jones, D. B. Eason, and G. Cantwell, Appl. Phys. Lett. **81** (2002) 1830.

2. M. Hiramatsu, K. Imaeda, N. Horio, and M. Nawata, J. Vac. Sci. Technol. ***A*.16** (1998) 669.

3. H. Kim, C. M.Gilmore, J. S. Horwitz, A. Pique, H. Murata, G. P. Kuhsto, R. Schlaf, Z. H. Kafafi, and D. B. Chrisey, Appl. Phys. Lett.**76** (2000) 259.

4. C. J. Lee, T. J. Lee, S. C. Lyu, Y. Zhang, H. Ruh, and H. J. Lee, Appl. Phys. Lett. **81** (2002) 3648.

5. R. L. Hoffman, J. F. Wager, M. K. Jayaraj and J. Tate, J. Appl. Phys. **90** (2001) 5763.

6. H. Ohta, M. Orita and M. Hirano, J. Appl. Phys. **89** (2001) 5720.

7. H. Sato, T. Minami, S. Takata and T. Yamada, Thin Solid Films **236** (1993) 27.

8. R. L. Hoffman, B. J. Norris, and J. F. Wager, Appl. Phys. Lett. **82** (2003) 733.

9. P. Misra, T. K. Sharma, S. Porwal, and L. M. Kukreja, Appl. Phys. Lett. **89** (2006) 161912.

10. J. Aranovich, A. Ortiz and R. H. Bube, J. Vacc. Sci. Technol. **16** (1979) 994.

11. K. A. Vanaja, R. S. Ajimsha, A. S. Asha, and M. K. Jayaraj, Appl. Phys. Lett. **88** (2006) 1.

12. R. S. Ajimsha, K. A. Vanaja, M. K. Jayaraj, P. Misra, V. K. Dixit and L. M. Kukreja, Thin Solid Films **515** (2007) 7352.

13.B. Lin, Z. Fu, and Y. Jia, Appl. Phys. Lett. **79** (2001) 943.

14. F. S. Hickernell, J. Appl. Phys. **44** (1973) 1061.

15. G. H. Lee, Y. Yamamoto, M. Kourogi, and M. Ohtsu, Thin Solid Films. **386** (2001) 117.

16. A. S. Riad, S. A. Mahmoud, and A. A. Ibrahim, Physica B **296** (2001) 319.

17. S. H. Lim, J. Washburn, Z. L. Weber, and D. Shindo, J. Vacc. Sci. Technol. ***A* 19**, 2601 (2001).

18. X. W. Sun and H. S. Kwok, J. Appl. Phys. **86** (1999) 408.

19. H. Cao, J. Y. Wu, H. C. Ong, J. Y. Dai, and R. P. H. Chang, Appl. Phys. Lett. **73** (1998) 572.

20. P. Misra and L. M. Kukreja, Thin Solid Films. **485** (2005) 42.

21. S. M. Jejurikar, A. G. Banpurkar, A. V. Limaye, S. K. Date, S. I. Patil, K. P. Adhi, P. Misra and L. M. Kukreja, J. Appl. Phys. **99** (2006) 014907.

22. Sang-Hun Jeong, Bong-Soo Kim, and Byung-Teak Lee, Appl. Phys. Lett. **82** (2003) 2625.

23. I. S. Jeong, Jae Hoon Kim, and Seongil Im, Appl. Phys. Lett. **83** (2003) 2946.

24. Y. S. Choi, J. Y. Lee, S. Im, and S. J. Lee, J. Vac. Sci. Technol. **B 20** (2002) 2384.

25. J. Y. Lee, Y. S. Choi, J. H. Kim, M. O. Park, and S. Im, Thin Solid Films. **403** (2002) 553.

26. P. Chen, X. Ma and D. Yang, J. Appl. Phys. **101** (2007) 053103.

27. X. D. Chen, C. C. Ling, S. Fung, and C. D. Beling Appl. Phys. Lett. **88** (2006) 132104.

28. D. K. Schroeder, Semiconductor Material and Device Characterisation, Wiley, NewYork. (1990) pp 205.

29. H. L. Hartnagel, A. L. Dawar, A. K. Jain, and C. Jagadish, *Semiconducting transparent thin films* (IOP Publishing Ltd, 1995) pp 10.
30. V. Srikant and D. R. Clarke, J. Appl. Phys. **83** (1998) 5447.
31. D. C. Look, J.W. Hemsky, and J. R. Sizelove, Phys. Rev. Lett. **82** (1999) 2552, and references cited therein
32. S. M. Sze, Physics of semiconductor devices, John Wiley and Sons, Newyork (1981) pp 123.
33. P. Chen, X. Ma and D. Yang, J. Appl. Phys. **102** (2007) 083103.

Chapter 5

Pulsed laser assisted growth of ZnMgO/ZnO multiple quantum well and ZnO nanorods

ZnMgO/ZnO multiple quantum well (MQW) of well layer thickness of 2 nm was grown on sapphire (0001) substrate by pulsed laser deposition (PLD) at a substrate temperature 400^{o}C. Room temperature photoluminescence (PL) was observed from these MQW's, which was found to be blue shifted as compared to the room temperature near band edge PL from ZnO thin film of 200 nm grown at same experimental conditions. ZnO thin films were deposited using PLD at room temperature by varying the oxygen pressure. Morphological analysis using scanning electron microscope (SEM) and atomic force microscopy (AFM) demonstrated the formation ZnO nanorods at a particular oxygen pressure. Temperature dependent luminescent studies of both ZnMgO/ZnO MQW and ZnO nanorods were carried out in detail. In this chapter, discussion of the growth and characterization of ZnMgO/ZnO Multiple Quantum Well and ZnO nanorods is presented in two parts.

Part I

Pulsed laser assisted growth of ZnMgO/ZnO multiple quantum well

5.1. Introduction

ZnMgO/ZnO multiple quantum well (MQW) structures have been grown by using various deposition techniques. The quantum well approach is effective towards the goal of current injection laser. ZnMgO epilayers and ZnMgO/ZnO multiple quantum wells (MQW) have been mainly prepared by pulsed laser deposition [1-4], metal–organic chemical vapor epitaxial methods [5,6] and molecular beam epitaxy (MBE) [7,8]. Krishnamoorthy et al [9] have reported quantum size effects at 77 K using PL measurements in ZnMgO/ZnO single quantum well samples grown on sapphire substrate using the pulsed laser deposition. However, when lattice matched substrate $ScAlMgO_4$ (SCAM) was used instead of sapphire, a significant improvement in the structural and optical properties was obtained, which was evident from their efficient photoluminescence [10-12]. But the scarce availability and expensive nature of these substrates made the situation essential to improve the method of growing ZnMgO/ZnO quantum wells on less expensive sapphire substrates. The literatures on the room temperature photoluminescence from ZnMgO/ZnO MQW on sapphire substrate are limited. There is a recent report on the room temperature photoluminescence from ZnO based quantum wells on sapphire

grown at 600^{o}C by PLD [13]. Literatures show that not much work has been reported on the room temperature (RT) luminescence from ZnO based quantum wells fabricated at substrate temperature below 500^{o}C. This part of the chapter presents the RT photoluminescence from ZnMgO/ZnO quantum well MQW grown by PLD at 400^{o}C

5.2. Experimental

Q-switched third harmonic Nd: YAG laser (355 nm) with repetition rate of 10 Hz and pulse width of 9 ns was used for the laser assisted film deposition. Laser beam was focused to a spot size 2 mm on the surface of the target and the target was kept in rotation for uniform ablation. The ZnMgO target for ablation was prepared by mixing 10 mol % of high purity MgO in ZnO powders and sintered at 1300^{o}C. The ZnO target was prepared by sintering its high purity powder at 1300^{o}C for 5 hours in air.

The ZnMgO/ZnO MQW's and ZnO thin film was fabricated in this study were deposited by using a multi carousal pulsed laser deposition (PLD) system. The growth chamber was initially evacuated to a base pressure of 4 x 10^{-7} mbar. The depositions were carried out in a high purity oxygen pressure of 10^{-4} mbar and laser energy density of 2 J/cm^{2}. The target to substrate distance was 60 mm and the substrate temperature was kept at ~ 400^{o}C. The film thickness of the PLD grown ZnO and ZnMgO films were measured using stylus profiler. From these thicknesses, the typical growth rate at these optimized conditions was found to be 0.18 nm/s for ZnO and 0.14 nm/s for ZnMgO films. These growth rates were used to control the barrier and well layer thickness. Initialy, a buffer layer of ZnO (thickness ~ 50 nm) was deposited on sapphire

substrate to minimize the lattice mismatch between sapphire and barrier layer of MQW. Then, ten periods of ZnMgO/ZnO layers were grown with a ZnMgO barrier layer thickness of 8 nm and a ZnO well layer thickness 2 nm on this ZnO template as shown in the figure 5.1. A ZnO thin film of thickness 200 nm was also deposited on sapphire substrate at same experimental conditions.

For studying the PL, a fourth harmonic pulsed Nd: YAG laser operating at 266 nm was used as an excitation source and resulting luminescence was collected using gated CCD in the temperature range 77 K to 300 K.

5.3. Results and discussion

Figure 5.2 shows the room temperature PL spectra of the MQW and ZnO thin film. PL peak position shifted from 3.26 eV to 3.58 eV while going from the luminescence of 200 nm ZnO thin film to MQW due to size dependent quantum confinement effects. It can be seen in figure 5.2 that the full width at half maximum (FWHM) of the PL peak of MQW was higher than that of the ZnO thin film. Increase in FWHM and small spikes in the PL spectra can be attributed to the fluctuations in well layer thickness and dominance of the interface roughness in 2 nm thick ZnO layers in MQW.

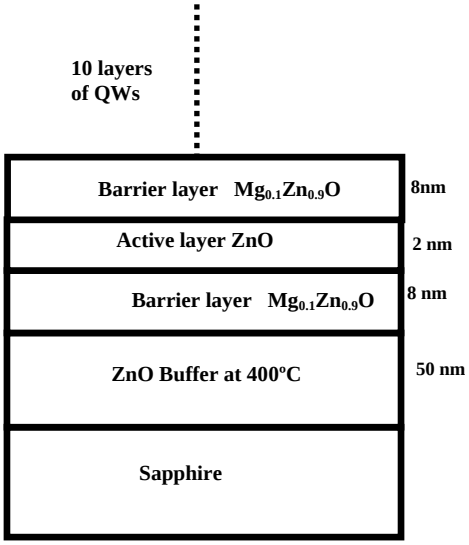

Figure 5.1 The structure of ZnMgO/ZnO MQW

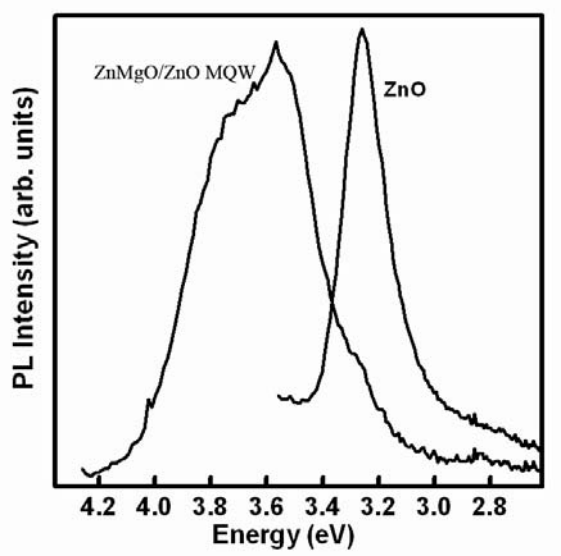

Figure 5.2 The room temperature PL of ZnMgO/ZnO MQW and ZnO thin film

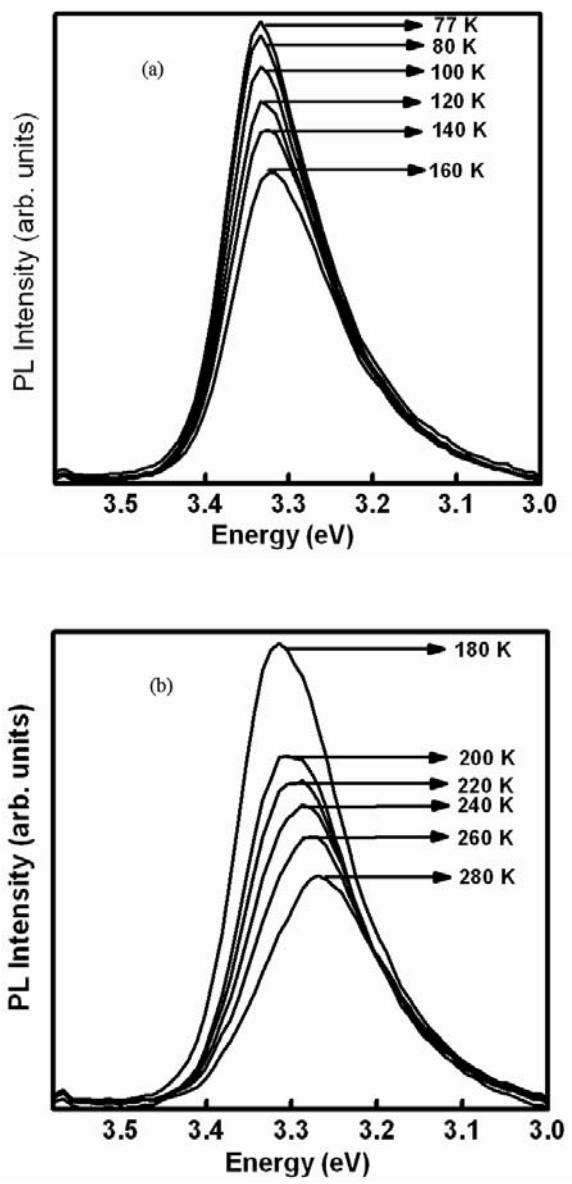

Figure 5.3 Temperature dependent PL spectra of ZnO thin film (a) from 77 K to 160 K (b) from 180 K to 280 K.

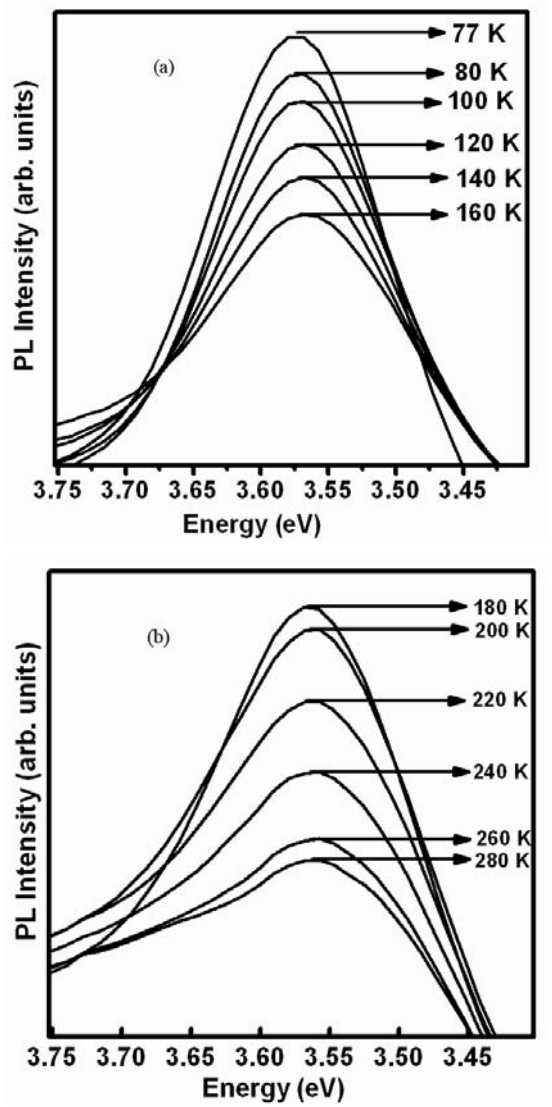

Figure 5.4 Temperature dependent PL spectra of ZnMgO/ZnO MQW (a) from 77 K to 160 K (b) from 180 K to 280 K.

.

Figure 5.3 and 5.4 represents the temperature dependent of PL spectra of ZnO thin film and MQW respectively. Integral intensity of PL decreases with increase of temperature in the case of both ZnO thin film (figure 5.5) and MQW (figure 5.6). Thermal quenching of this emission line can be described by [14]

$$I(T) = I(T=0)/1 + C \exp(-E_a/KT) \qquad (5.1)$$

where I (T) is the PL intensity at temperature T, C is the constant describing the capture of carriers at centre and E_a is the activation energy of the quenching process. Variation of PL intensity with temperature was fitted with eqn (5.1) to obtain the activation energy E_a. E_a was found to be comparable with the excitonic binding energy of ZnO and the values were 46.57 meV and 50.03 meV for MQW and ZnO thin film respectively. The decrease in E_a in the case of MQW may be due to quantum confinement effect.

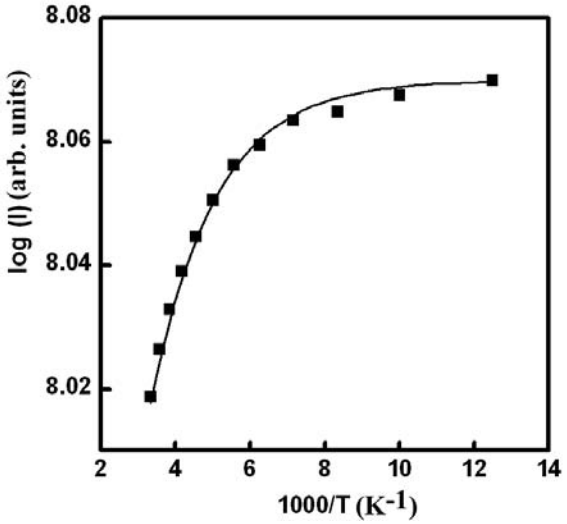

Figure 5.5 Integral intensity of PL emission of ZnO thin film fitted by the equation (5.1).

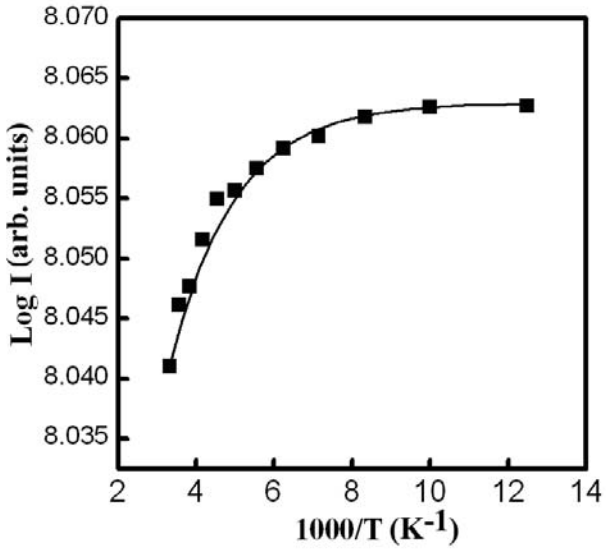

Figure 5.6 Integral intensity of PL emission of ZnMgO/ZnO MQW fitted by the equation (5.1).

Temperature dependence of PL line width of ZnO thin films and MQW is shown in figure 5.7 and 5.8 respectively. It can be seen from figure 5.7(a) and 5.7(b) that the line width of PL peak of ZnO thin film increases gradually up to 140 K and then exponentially up to RT. The linear increase in line width below 140 K implies the dominance of acoustic phonon scattering at lower temperatures, which can be described by [15]

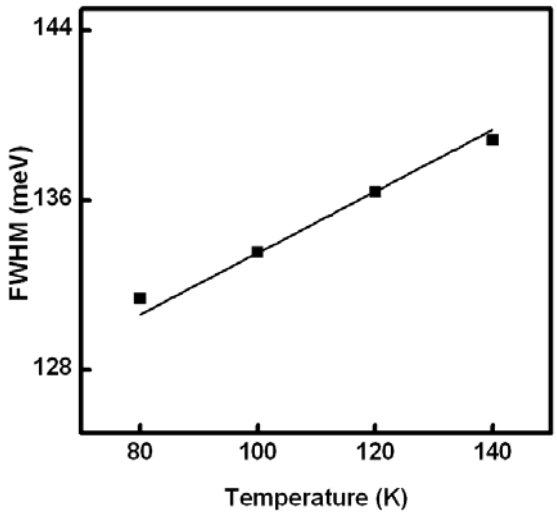

Figure 5.7 (a) Linear dependence of FWHM of PL spectrum (ZnO thin film) from 77 K to 140 K fitted by equation (5.2)

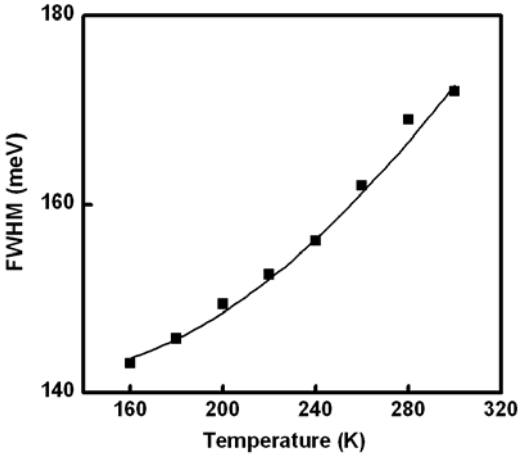

Figure 5.7 (b) Exponential dependence of FWHM of PL spectrum from 160 K to 300 K fitted by equation (5.3)

$$\Gamma_{hom}(T) = \Gamma_{hom}(T=0) + \gamma_{ph}T \qquad (5.2)$$

where γ_{ph} denotes the exciton-acoustic phonon coupling strength, Γ_{hom} (T=0) and Γ_{hom} (T) represents the homogeneous line width at temperature, T = 0 K and T = T K. Exponential increase in line width at higher temperature range, where the exciton-longitudinal optic (LO) phonon interaction predominates the PL line width, which can be approximately described [16] by the equation (5.3).

$$\Gamma(T) = \Gamma_{Inh} + \frac{\Gamma_{LO}}{\exp(\frac{\hbar\Omega_{LO}}{KT}) - 1} \qquad (5.3)$$

Γ_{Inh} is the inhomogeneous line width at 0 K, Γ_{LO} represents the coupling strength of exciton scattering with LO phonon and $(\exp(\frac{\hbar\Omega_{LO}}{KT})-1)$ is the population of LO phonons of energy $\hbar\Omega_{LO}$. The best fit to the experimental data, as shown by continuous curves in figure 5.7 was obtained for the fitting parameters Γ_{hom} (T=0) = 119 meV, $\Gamma_{inh,}$ = 141 meV, Γ_{LO} = 480 meV and γ_{ph} = 145 μeV/K. Figure 5.8 shows that MQW behaves differently in the higher temperature range as compared to ZnO thin film. This may be due to the smaller scattering probability of exciton with LO phonons due to reduced density of LO phonons even at higher temperatures. Figure 5.8 can be divided into three linear regions of decreasing slope with temperature where equation of acoustic phonons fitted very well. In these regions experimental data was fitted using the parameters γ_{ph} = 1220 μeV/K, 482.5 μeV/K, 208 μeV/K and Γ_{hom} (T=0) = 152 meV, 285 meV, 355 meV. The decrease in γ_{ph} with increase of temperature is the result of decreased density of acoustic phonons available for exciton scattering. This may be due to size dependent quantum confinement effect in MQW.

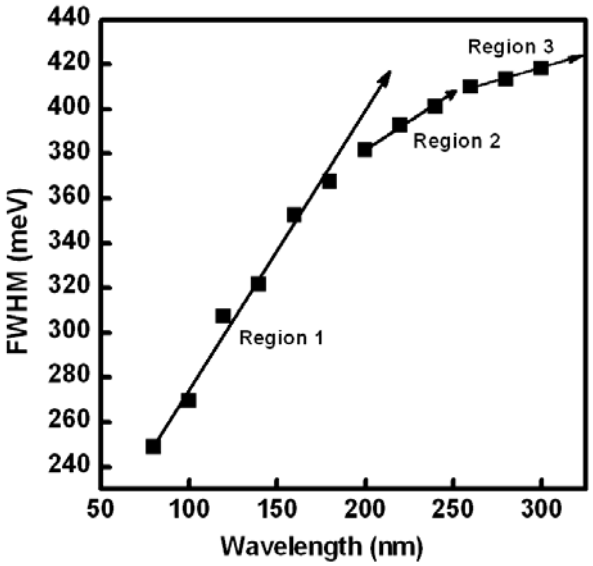

Figure 5.8 Variation of FWHM of PL spectrum of ZnMgO/ZnO MQW with temperature consisting of three linear regions fitted by equation (5.2)

Figure 5.9 shows the temperature dependent PL peak position of ZnO thin films. PL peak positions were found to be red shifted with increase of temperature upto 300 K. This is due to band gap shrinkage with increase in temperature. The variation of the band gap with temperature was fitted with Varshni's empirical relation [17] and best fit to the experimental data was obtained for the fitting parameters, $\alpha = -4.2 \times 10^{-4}$ eV/K and $\beta = 1070$ K.

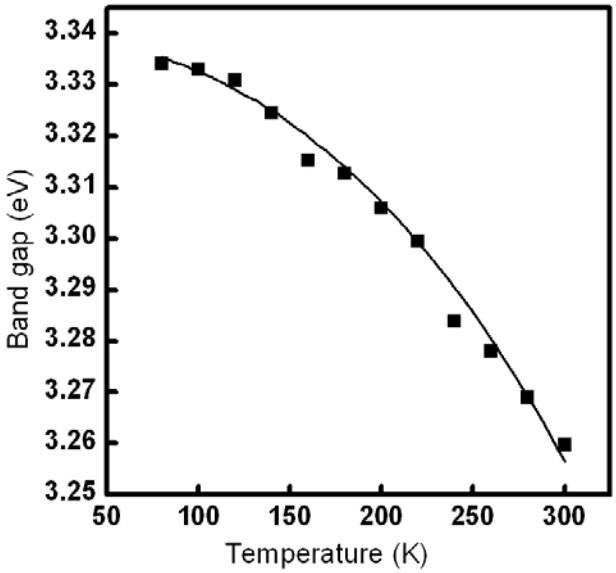

Figure 5.9 The temperature dependent PL peak position of ZnO thin films fitted by Varshni's empirical relation.

5.4. Conclusion

Room temperature PL was observed from ZnMgO/ZnO MQW with well layer thickness of 2 nm grown on sapphire (0001) substrate by buffer assisted pulsed laser deposition (PLD) at a substrate temperature of 400^{o}C. A blue shift in PL from ZnMgO/ZnO MQW was found as compared to the room temperature near band edge PL from ZnO thin film. Low temperature PL studies were carried out on ZnMgO/ZnO MQW and ZnO thin film in the range from 300 K to 77 K. The results thus obtained can be explained using the existing models.

Part II

Pulsed laser assisted growth of ZnO nanorods

5.5. Introduction

Synthesis of one dimensional ZnO nanostructures (nanorods) has been paid much attention owing to the promising application in photonic devices. Vertically aligned ZnO nanonails have been successfully grown on annealed sapphire substrates at comparatively high gas pressure using catalyst-free nanoparticle-assisted pulsed-laser ablation deposition (NAPLD) [18]. The well-aligned ZnO nanonails exhibit a strong ultraviolet (UV) emission at 390 nm at room temperature and have only negligible visible emission. The weak visible emission indicates that there is a very low concentration of oxygen vacancies in the highly oriented ZnO nanonails.

Okada et al [19] succeeded in synthesizing ZnO nanorods by nanoparticle assisted pulsed-laser deposition (NAPLD) without using any catalyst where nanoparticles formed by condensation of ablated particles play an important role. Stimulated emission (at 388 nm) was observed from ZnO nanorods grown by pulsed-laser deposition [20]. But the literatures on the room temperature violet luminescence from ZnO nanorods grown on substrates at room temperature are scarcely available. This section discusses the room temperature violet luminescence from ZnO nanorods grown at room temperature by PLD.

5.6. Experimental

Depositions of ZnO films were carried out by ablating sintered ZnO target at room temperature. The conditions of target preparation and details of the PLD system are similar to that described in section 5.2. Before starting deposition the chamber was evacuated to a pressure of 10^{-6} mbar. At room temperature the ZnO films on quartz substrates were grown at different oxygen partial pressures varying between 0.007 mbar to 0.003 mbar and at laser energy density of 3 J/cm^2 for 20 minutes resulting film thickness of 200 nm. The target to substrate distance was varied from 6 cm to 4 cm to optimize the growth of ZnO.

Crystalline nature of the films was confirmed using x-ray diffractometer (Rigaku) with Cu-Kα radiation (1.5414 Å). Thickness was measured using Dektak 6M stylus profiler. Surface morphology of the ZnO films were studied using atomic force microscope (AFM) (Veeco) and scanning electron microscope (SEM) (JEOL JSM 5600). Raman studies was carried out with micro Raman (Jobin Yvon Horibra) with excitation source as argon ion laser (488 nm).

5.7. Results and discussion

Figure 5.10 shows the x-ray diffraction pattern of ZnO thin films grown at room temperature on quartz substrate by varying the oxygen partial pressure in the range 0.003 mbar to 0.007 mbar. X-ray reflections shows the formation of polycrystalline ZnO film with (002) orientation in this pressure window (0.003 mbar to 0.007 mbar). Full width half maximum (FWHM) of (002) diffraction peak was found to be minimum, when an oxygen partial pressure of 0.004 mbar

was used during deposition. Better crystalline films were formed at an oxygen background pressure of 0.004 mbar.

In PLD of ZnO, laser ablated plume containing various ionic species of zinc and oxygen is expanding adiabatically towards the substrate. Kinetic energy of the zinc and oxygen ionic species reaching the substrate is likely to stimulate the motion of the surface and near surface atoms in the deposited film, thereby relieving film stress, and encouraging changes in film morphology and microcrystalline structure. The discussion thus far has implicitly assumed that adatom adsorption and nucleation occurs homogeneously, and at various sites on the substrate surface. Amorphous films with almost uniform thickness were obtained when the deposition was carried out at room temperature at a target to substrate distance of 6 cm. Polycrystalline films of ZnO oriented in the (002) plane having uniform thickness on 1 cm^2 area were formed when the substrate to target distance is decreased to 4 cm. This type of variation in crystalline nature with substrate to target distance was reported by Cherief et al [21]. Various ionic species of ZnO in the laser ablated plasma plume bombarding the substrate kept at 4 cm distance from the target surface may have sufficient energy for crystallization in the form of ZnO film. When the substrate is placed at 6 cm the ablated species reaching the substrate may not have the minimum energy required for crystallization and thereby getting amorphous films.

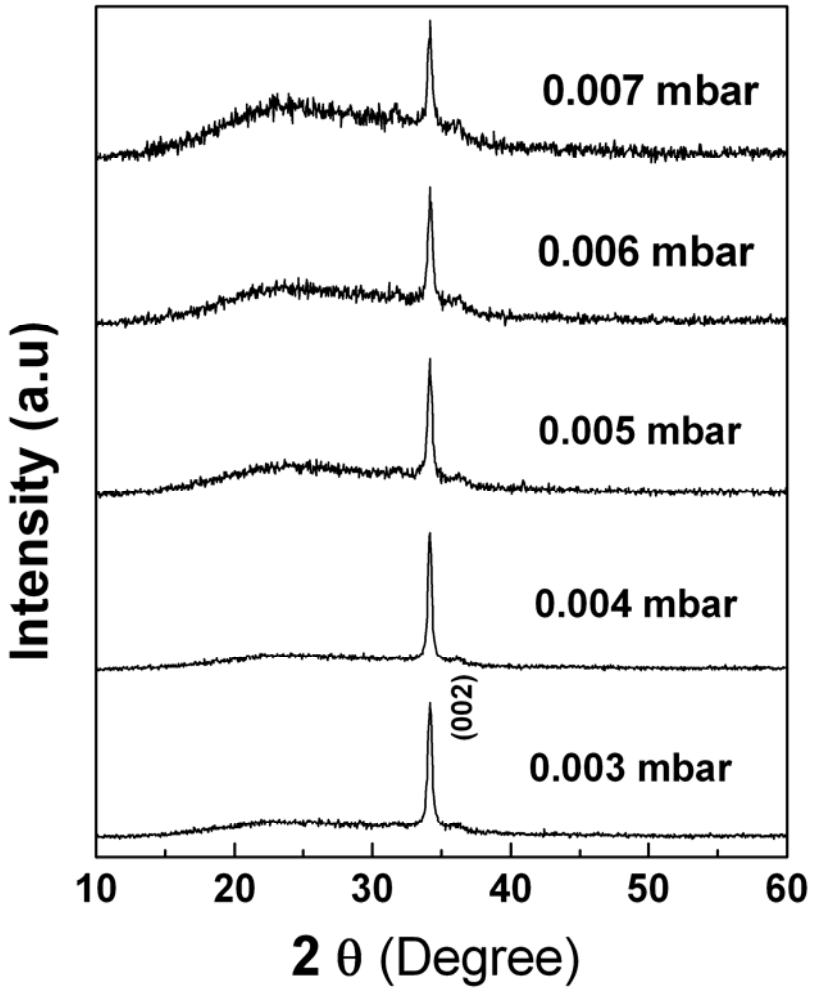

Figure 5.10 XRD patterns of ZnO films grown by PLD at various oxygen pressures (0.003 mbar to 0.007 mbar).

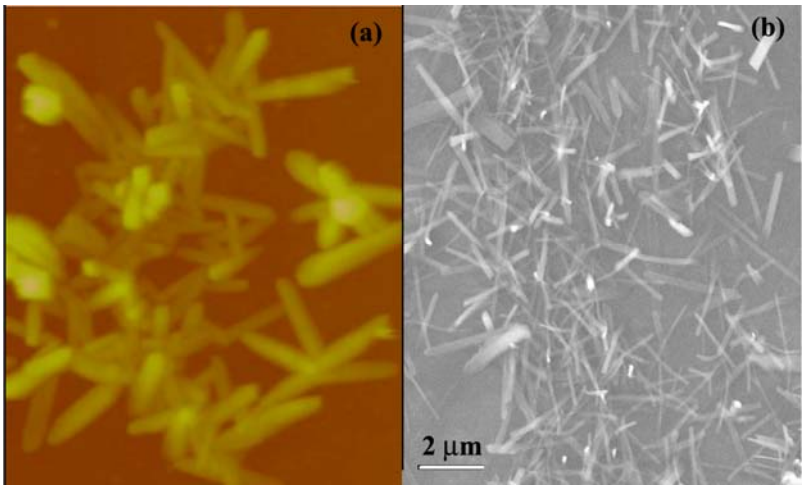

Figure 5.11 (a) The AFM and (b) represents the SEM of ZnO nano rods.

AFM of ZnO grown on quartz substrate at 0.004 mbar demonstrates the formation of nanorods of length 2 μm and diameter 100 nm (as shown in figure 5.11 (a)). SEM also confirmed the growth of ZnO nanorods (shown in figure 5.11 (b)). The films grown at other oxygen pressures do not show any rod like growth as confirmed by AFM. Thus 0.004 mbar was found to be the optimum oxygen pressure at room temperature for the growth of ZnO nano rods.

Room temperature violet luminescence was observed from ZnO nano rods when excited at 266 nm using fourth harmonic Nd: YAG laser. Figure 5.12 shows the temperature dependent PL spectrum of ZnO nano rods at low temperature up to 77 K and the inset represents it's room temperature violet luminescence. Violet emission peaking at 408 nm is due to the transition of electrons from shallow donor levels to valance band [22].

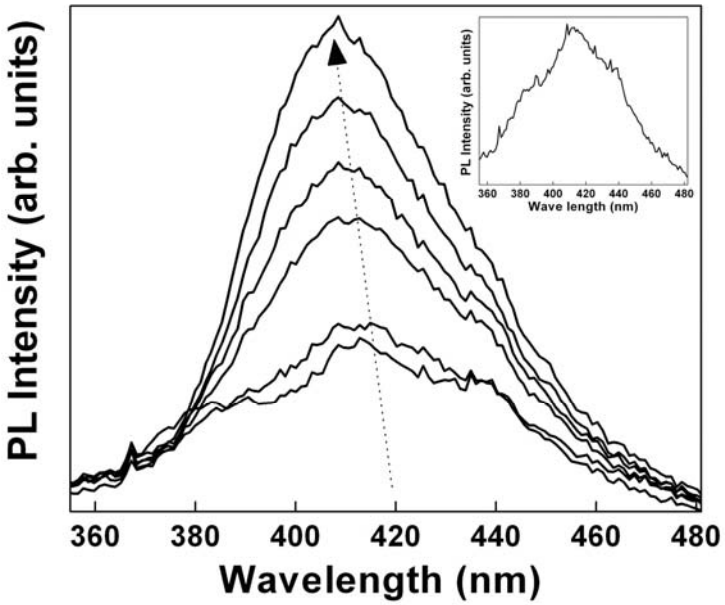

Figure 5.12 PL spectra of ZnO nano rods at 77 K, 100 K, 140 K, 180 K, 220 K, 260 K and 280 K and arrow represents the decreasing temperature. Inset show the room temperature PL.

From figure 5.12, it is found that PL peak position was found to shift by 38 meV towards red with increase in temperature up to 300 K (shown in figure 5.13 (a)). This is expected due to band gap shrinkage with increasing temperature. But, the full width at half maximum (FWHM) of the PL peak increases (figure 5.13 (a)) and integral intensity of PL spectra decreases with increase of temperature (figure 5.13 (b)). Increase of PL line width with temperature is almost exponential in nature. Variation of PL intensity with temperature was fitted with equation (5.1) (figure 5.13 (b)) to obtain the activation energy E_a and it was found to be 38 meV.

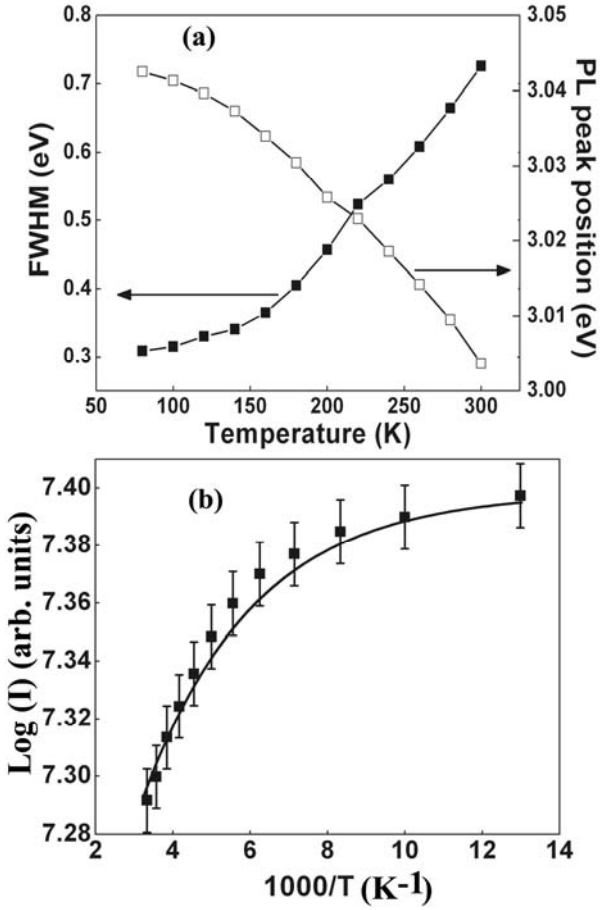

Figure 5.13 (a) Variation of FWHM and peak position of PL spectra of ZnO nanorods with temperature and it's (b) PL integral intensity fitted with equation 5.1

Micro Raman scattering studies were carried out on ZnO nanorods to obtain information about the effects of increase in surface area in comparison to the continuous film or single crystal on the optical phonons and the lattice defect modes. ZnO with a wurtzite structure belongs to the C_{6v} symmetry group. At the $\tilde{\Gamma}$ point of the Brillouin zone, optical phonons have $\Gamma_{opt} = A_1 + 2B_1 + E_1 + 2E_2$, where A_1 and E_1 modes belong to polar symmetries and can have different transverse (TO) and longitudinal (LO) optical phonon frequencies, all being Raman active, while the B_1 modes are silent. Figure 5.14 shows the Raman spectra of ZnO nanorods excited using the 488 nm line of argon ion laser. The spectra exhibits asymmetric broad peak at 575 cm^{-1} which is the red shifted A_1-LO phonon mode at 579 cm^{-1} of bulk ZnO [23]. Such red shift, broadening and asymmetry of the A_1-LO mode could result from three main mechanism [24] (1) phonon localization by intrinsic defects, (2) laser heating in nanostructure ensembles, and (3) the spatial confinement with in the rod boundaries.

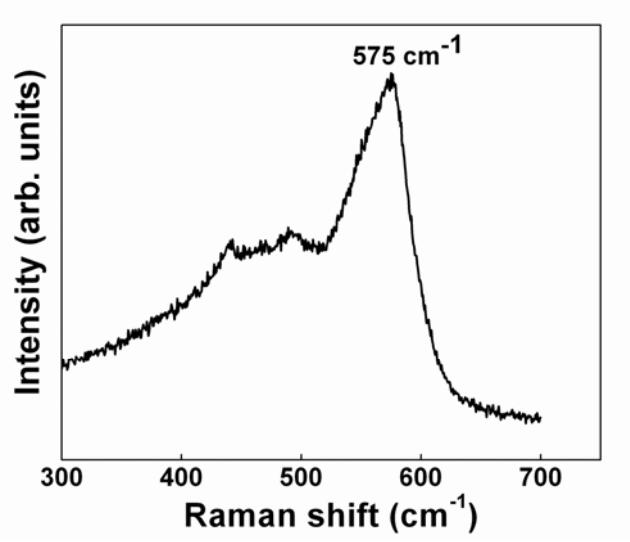

Figure 5.14 Micro Raman spectrum of ZnO nanorods grown by PLD

5.8. Conclusion

Polycrystalline ZnO films oriented in the (002) plane were grown by room temperature Pulsed Laser Deposition (PLD). Formation ZnO nanorods at a particular oxygen pressure was observed from SEM and AFM. Room temperature violet luminescence peaking at 408 nm was observed from these ZnO nano rods. Micro Raman spectra of ZnO nanorods exhibited shift and broadening in the peak clearly shows the formation of nanorods. Low temperature PL spectra were recorded for ZnO nanorods in the temperature range 300 K to 77 K. The results are explained using the existing models.

5.9. References

1. A. K. Sharma, J. Narayan, J. F. Muth, C. W. Teng, C. Jin, A. Kvit, R. M. Kolbas, and O. W. Holland, Appl. Phys. Lett. **75** (1999) 3327.
2. A. Ohtomo and A. Tuskazati, Semicond. Sci. Technol. **20** (2005) S1, and references therein.
3. I. Takeuchi, W. Yang, K. S. Chang, M. A. Aronova, T. Venkatesan, R. D. Vispute, and L. A. Bendersky, J. Appl. Phys. **94** (2003) 7336.
4. C. Bundesmann, M. Schubert, D. Spemann, T. Butz, M. Lorenz, E. M. Kaidashev, M. Grundmann, N. Ashkenov, H. Neumann, and G. Wagner, Appl. Phys. Lett. **81** (2002) 2376.
5. T. Gruber, C. Kirchner, R. Kling, F. Reuss, and A. Waag, Appl. Phys. Lett. **84** (2004) 5359.
6. B. P. Zhang, N. T. Binh, K. Wakatsuki, C. Y. Liu, Y. Segawa, and N. Usami, Appl. Phys. Lett. **86** (2005) 032105.
7. Y. Chen, H.-J. Ko, S.-K. Hong, T. Sekiuchi, T. Yao, and Y. Segawa, J. Vac. Sci. Technol. B **18** (2000) 1514.
8. K. Koike, K. Hama, I. Nakashima, G.-Y. Takada, M. Ozaki, K.-I. Ogata, S. Sasa, M. Inoue, and M. Yano, Jpn. J. Appl. Phys., Part 2 **43** (2004) L1372.
9. S. Krishnamoorthy, A. A. Iliadis, A. Inumpudi, S. Choopun, R. D. Vispute, and T. Venkatesan, Solid-State Electron. **46** (2002) 1633.
10. T. Makino, Y. Segawa, M. Kawasaki, and H. Koinuma, Semicond. Sci. Technol. **20** (2005) S78.

11. T. Makino, N. T. Tuan, H. D. Sun, C. H. Chia, Y. Segawa, M. Kawasaki, A. Ohtomo, K. Tamura, T. Suemoto, H. Akiyama, M. Baba, S. Saito, T. Tomita, and H. Koinuma, Appl. Phys. Lett. **78** (2001) 1979.
12. T. Makino, C. H. Chia, Nguen T. Tuan, H. D. Sun, Y. Segawa, M. Kawasaki, A. Ohtomo, K. Tamura, and H. Koinuma, Appl. Phys. Lett. **77** (2000) 975.
13. P. Misra, T. K. Sharma, S. Porwal and L. M. Kukreja, Appl. Phys. Lett. **89** (2006) 161912.
14. J. P. Dean Phys Rev, **157 (**1967) 655.
15. R. Hellmann, M. Koch, J. Feldmann, S. T. Condiff, E. O. Gobel, D. R. Yakovlev, A. Waag, and G. Landwehr, Phys. Rev. B **48** (1993) 2847.
16. M. O'Neill, M. Oestreich, W. W. Ruhle, and D. E. Ashenford, Phys. Rev. B **48** (1993) 8980.
17. Y. P. Varshni, Physica (Amsterdam) **34** (1967) 149.
18. R. Q. Guo, J. Nishimura, M. Ueda, M. Higashihata, D. Nakamura and T. Okada, Appl. Phys. A **89** (2007) 141.
19. T. Okada, B. H. Agung and Y. Nakata, Appl. Phys. A **79**, (2004) 1417.
20. A. Rahm, M. Lorenz, T. Nobis, G. Zimmermann, M. Grundmann, B. Fuhrmann and F. Syrowatka, Appl. Phys. A **88** (2007) 31.
21. N. Cherief, D. Givord, A. Lienard, K. Mackay, O. F. K. McGrath, J. P. Rebouillat, F. Robaut and Y. Souche, J. Magn. Magn. Mate. **121** (1993) 94.
22. H. Zeng, W. Cai, J. Hu, G. Duan, P. Liu, and Y. Li, Appl. Phys. Lett. **88** (2006) 171910.

23. M. Rajalekshmi, A. K. Arora, B. S. Bendre and Shailaja Mahamuni, Appl. Phys. Lett. **87** (2000) 2445.
24. K. A. Alim, V. A. Fonoberov and A. A. Balandin, Appl. Phys. Lett. **86** (2005) 53103.

Chapter 6

Synthesis and characterization of surfactant free ZnO quantum dots by laser ablation in liquid

Highly transparent, luminescent and bio-compatible ZnO quantum dots were prepared in water, methanol and ethanol using liquid phase pulsed laser ablation technique without using any surfactant. Transmission Electron Microscope (TEM) analysis confirm the formation of good crystalline ZnO quantum dots with a uniform size distribution of 7 nm. The emission wavelength could be varied by playing the native defect chemistry of ZnO quantum dots and by varying the laser fluence.

6.1. Introduction

Synthesis of nanoparticles has been a focus of an ever-increasing number of reasearchers world wide, mainly due to their unique optical and electronic properties [1-5] which makes them ideal for a wide spectrum of applications ranging from displays [6], lasers [7, 8] to *in vivo* biological imaging and therapeutic agents [9]. Large number of different preparation methods are reported to produce nanoparticles, such as magnetic liquids [10], metal-polymer nano composites [11], semiconductors [12] and colloidal systems [13]. Over the past decade a novel technique known as liquid phase pulsed laser ablation (LP-PLA) has aroused immense interest [14, 15] and it involves the firing of laser pulses through liquids transparent to that wavelength on to the target surface. The ablation plume interacts with the surrounding liquid particles creating cavitation bubbles, which upon their collapse, give rise to extremely high pressures and temperatures. These conditions are, however, very localized and exist across the nano meter scale. Compared with the ablation in vacuum, formation of nanoparticles by pulsed laser ablation of targets in liquid environments has been less studied. Parameters like laser wavelength, pulse energy, pulse duration, repetition rate and nature of the liquid medium have influences on the ablation, nucleation, growth and aggregation mechanisms.

LP-PLA has proven to be an effective method for preparation of many nanostructured materials, including nanocrystalline diamond [16], cubic boron nitride [17], and nanometer-sized particles of Ti [18], Ag [19], Au [20] and TiC [21]. Wurtzite ZnO with wide band gap and excitonic energy of 60 meV has many important applications in UV light emitting diodes, diode lasers, sensors, etc. Since zinc is very important trace elements of humans [22], ZnO is

environmentally friendly and suitable for *in vivo* bio-imaging and cancer detection. Recent reports came on the synthesis of ZnO nanoparticles using LP-PLA technique from Zn target in an aqueous solution containing different surfactants [23, 24]. Zeng et.al [24] has used 1064 nm for ablation which will have greater penetration in to the target ablating more particulates. Further more without any surfactant these particles will not stand isolated. The use of metallic Zn target along with surfactants like sodium dodecyl sulfate (SDS) give rise to the formation of several bye products like $Zn(OH)_2$ and the QD's were Zn/ZnO core shell structure. The present investigation is on surfacatant free pure ZnO QD's with out any byproducts using LP-PLA technique. To the best of our knowledge, LP-PLA technique has not been used for the synthesis of pure ZnO quantum dots (QD's) without the use of surfactants. The literature survey shows not much work has been done on the synthesis of ZnO quantum dots using methods without any surfactants. Recently we reported [25] the growth of luminescent, bio-compatible ZnO quantum dots using wet chemical method without any surfactant. The preparation of high quality ZnO QD's with specific interest on their luminescence properties and surface functionality with the aim of biological applications have not been studied widely**.**

This chapter presents the preparation of highly luminescent (visible to naked eye on Ultra-Violet (UV) illumination) transparent, chemically pure and crystalline ZnO QD's using LP-PLA technique without the aid of any surfactant. Clear, deep yellow and blueish-violet emitting ZnO QD's fully dispersed in water, ethanol and methanol were prepared directly from the ZnO targets by this technique without any byproduct. Thus obtained bio-friendly ZnO QD's can be

used as fluorescent probes in various biomedical applications by easily attaching bio-molecules to the bare surface of these ZnO QD's.

6.2. Experimental

A sintered ZnO mosaic target was used for the fabrication of ZnO QD's. The ZnO target was prepared by sintering its high purity (99.99%) powder at 1300^{o}C for 5 hours in air. Sintering conditions of the target was similar to that of the ZnO target used in the fabrication of diode, nanorods and quantum wires discussed in other chapters. ZnO target immersed in 20 ml of different liquid media like deionized water, methanol and ethanol was ablated at room temperature by the third harmonic Nd: YAG (Yitrium Aluminium Garnet) laser (355 nm, repetition frequency of 10 Hz, pulse duration 9 ns). Spot size of the laser beam was 2 mm after focusing using a lens and the ablation was done at laser fluences 25 mJ/pulse, 35 mJ/pulse and 45 mJ/pulse. Duration of laser ablation was 1 hr in all the liquids. In water, ablation was also carried out for different durations of 1 hr, 2 hrs and 3 hrs by keeping the laser fluence at 45 mJ/pulse. This simple room temperature technique produced highly transparent ZnO QD's well dispersed in respective liquid media. Formation of nanoparticles of ZnO was confirmed by Transmission Electron Microscope (TEM) (JEOL) operating at an accelerating voltage of 200 kV. A small droplet of the liquid obtained after ablation was deposited on to a copper grid with carbon film for TEM analysis. Photoluminescence emission (PL) and excitation spectra (PLE) were recorded using Jobin Yvon Fluoromax-3 spectrometer equipped with 150 W xenon lamp.

6.3. Results and discussion

6.3.1. Transmission electron microscopy

To study the morphology and microstructure, Transmission electron microscope (TEM) analysis were carried out on the resultant product after laser ablation. TEM analysis revealed that ZnO samples after laser ablation with energy 25 mJ/pulse in water consists of particles in the nano regime as shown in figure 6.1(a). Statistical size analysis (figure 6.1(b)) shows almost uniform particle size distribution with particle size 7 nm.

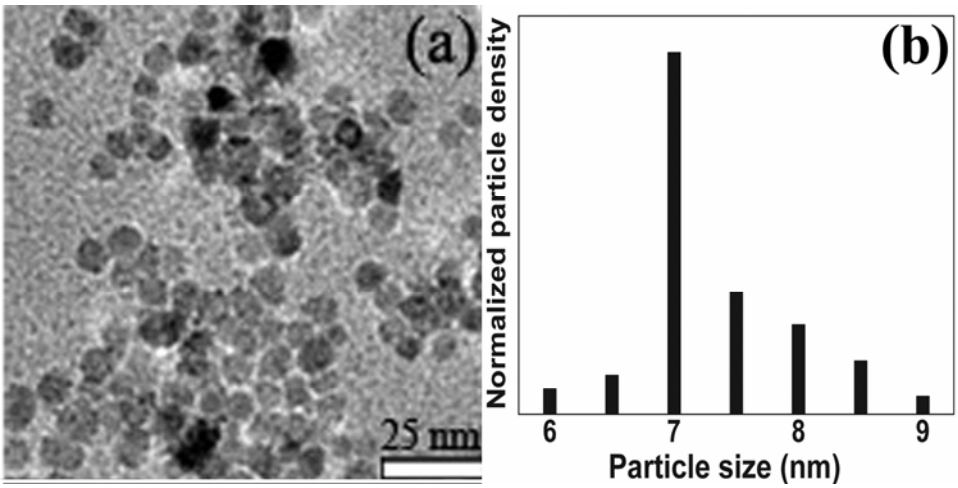

Figure 6.1 (a) TEM image and (b) particle size distribution of ZnO QD's obtained by laser ablation with fluence 25 mJ/pulse in water

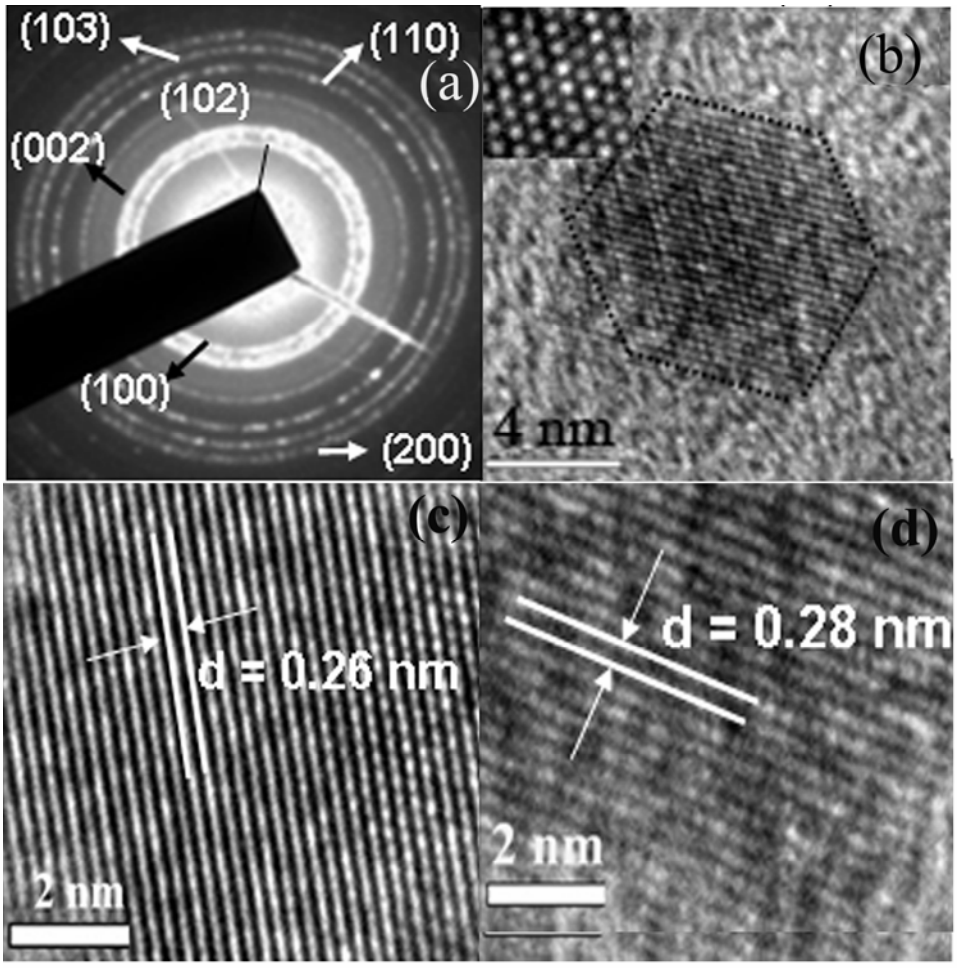

Figure 6.2 (a) SAED pattern of ZnO QD's, (b) HRTEM image for a single QD and it's inset shows the arrangement in the hcp mode, (c) and (d) HRTEM showing (002) and (100) planes ZnO QD's respectively (obtained by laser ablation with fluence 25 mJ/pulse in water).

Selective Area Electron Diffraction (SAED) was used for the material identification of quantum dots. SAED pattern was analysed using the equation (2.8) and indexed various planes corresponding to ZnO. The SAED

pattern (figure 6.2(a)) exhibits well distinguishable concentric ring pattern representing the (100), (002), (102), (110) and (103) planes of hexagonal ZnO. This clearly shows the growth of crystalline ZnO QD's with random orientation. ZnO QD's were arranged in hexagonal shape as observed from high resolution transmission electron microscope (HRTEM) image (figure 6.2(b)). The stacking of about 85 hexagonal unit cells make a 7 nm sized hexagonal shaped QD. The inset of figure 6.2(b) shows the arrangement of individual unit cells which again demonstrates the crystalline quality of ZnO QD's. The Zn/ZnO composite nanoparticles grown by Zeng et.al [24] has an average particle size 18 nm and colored due to turbidity. An atomic scale image shows the parallel lines of ions at intervals of 0.26 nm (figure 6.2(c)) and 0.28 nm (figure 6.2(d)) which corresponds to (002) and (100) planes of ZnO respectively. From TEM analysis, the formation of other molecules like $Zn(OH)_2$ or ZnO/Zn core shell formation is not found. Since the ejected molten material from the target normally reacts with medium only at the outer surface [26], the ejected plasma readily cools thereby reforming ZnO itself. Since there are many surface defects, mainly due to surface oxygen deficiency (discussed later), these nano particles are charged. This surface charge will provide a shield, preventing further agglomeration thereby forming self-stabilized particles even in the absence of surfactant.

Figure 6.3 (a), (c) and (e) shows the TEM images and (b), (d) and (f) represents the particle size distribution of the ZnO QD's prepared in methanol at laser fluences 25 mJ/pulse, 35 mJ/pulse and 45 mJ/pulse respectively. It explicitly demonstrates the increase of both particle size and particle density with laser fluence. Particle sizes as observed from the size distribution (b), (d) and (f)) are 7.1 nm, 8 nm and 9.1 nm for ZnO QD's

prepared at laser fluence 25 mJ/pulse, 35 mJ/pulse and 45 mJ/pulse respectively. TEM shows a similar size distribution for those prepared in ethanol where as for the QD's prepared in water by LP-PLA of ZnO doesn't show any variation in size on varying the fluence from 25 mJ/pulse to 45 mJ/pulse. The thermodynamic conditions created by the laser ablation plume in the liquid are localized to a nano meter scale which is varying with laser fluence. This is the reason for variation of particle size of ZnO QD's with laser fluence.

However, the interaction of laser pulse with the organic solvents and water are different and a complex phenomenon. Also the ejected plasma interaction with the liquid will depend up on the composition, nature and dielectric constant of the media which may influence the particle size to a greater extent. With the characterization techniques used in this work, it is possible only to give a speculative explanation. Hence the mechanism of particle formation in different liquid media is not discussed in the current work.

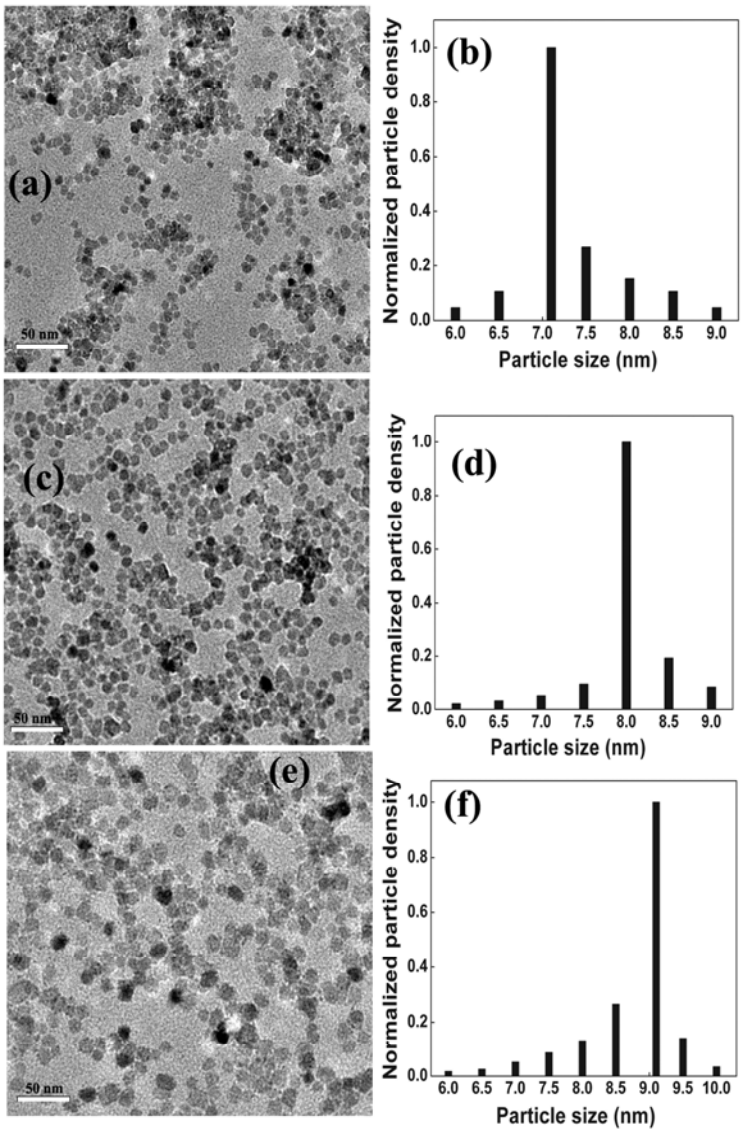

Figure 6.3 (a), (c) and (e) shows the TEM and (b), (d) and (f) represents the particle size distribution of ZnO QD's dispersed in methanol prepared at laser fluences of 25 mJ/pulse, 35 mJ/pulse and 45 mJ/pulse respectively.

6.3.2. Optical absorption spectra

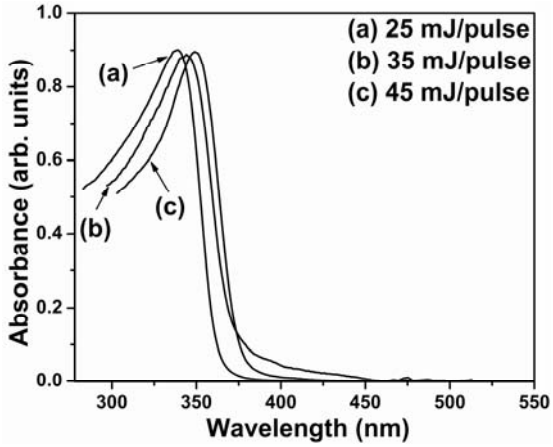

Figure 6.4 Absorption spectra of ZnO QD's in methanol prepared at (a) 25 mJ/pulse (b) 35 mJ/pulse and (c) 45 mJ/pulse.

Figure 6.4 shows the absorption spectra in the UV-VIS range of ZnO QD's (of sizes 7 nm, 8.1 nm and 9 nm) dispersed in methanol prepared at laser energy 25 mJ/pulse, 35 mJ/pulse and 45 mJ/pulse. It is observed that the increase in laser energy (increase in particle size) resulted in red shift of excitonic peak from 3.67 eV to 3.57 eV and slightly broadened due to quantum size effects [27].

6.3.3. Photoluminescent (PL) studies

PL measurement was performed in the QD's dispersed in water, ethanol and methanol at excitation wavelength of 345 nm. Deep yellow luminescence was observed from the ZnO QD's dispersed in water. Figure 6.5(a) shows the photograph of highly transparent ZnO QD's (left) dispersed in water and it's yellow emission under UV excitation. This yellow luminescence originates from the native oxygen defects of the prepared ZnO QD's (discussed latter).

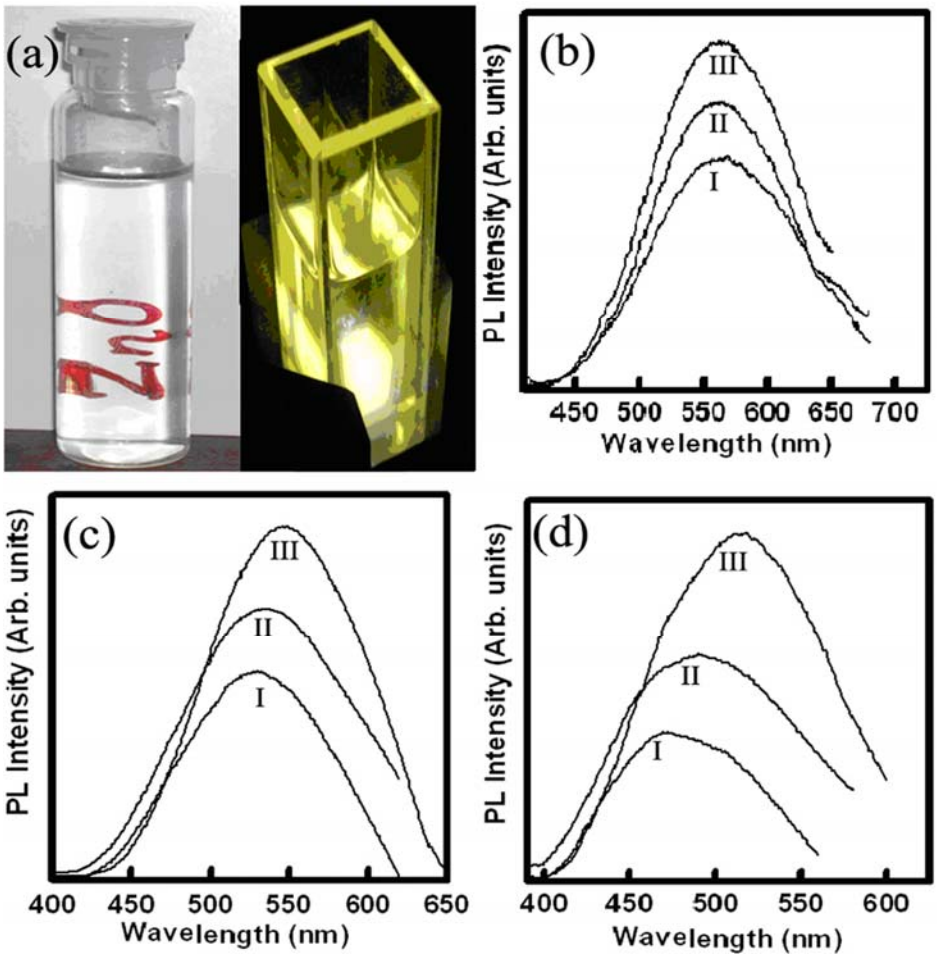

Figure 6.5 (a) Photograph of transparent ZnO QD's obtained by laser ablation in water with fluence 25 mJ/pulse (left) and it's yellow emission (right). (b) PL spectra of ZnO QD's in water (c) ethanol and (d) methanol. In each figure, curve I (25 mJ/pulse), curve II (35 mJ/pulse), and curve III (45 mJ/pulse) represents the laser fluence.

Figure 6.5(b) - (d) shows the PL spectra of ZnO QD's dispersed in water, ethanol and methanol respectively. Pure water, ethanol and methanol do not show any emission under UV excitation. Each figure depicts the variation of PL intensity with the laser fluence at which these QD's were prepared in the liquid.

Considerable increase of PL intensity with fluence of the laser beam (used for pulsed laser ablation in liquid media) is observed for all the samples. The increase in PL intensity with laser fluence used during the synthesis of ZnO QD's cannot be attributed to increase in particle density alone. There can be a possibility of formation of more defect states at higher fluence which is not clear in the present investigation.

A blue shift in PL maximum was observed for QD's prepared with lower laser fluence, in the case of QD's grown in methanol (from 2.41 eV at 45 mJ/pulse to 2.6 eV at 25 mJ/pulse) and ethanol (from 2.27 eV at 45 mJ/pulse to 2.35 eV at 25 mJ/pulse). However the PL peak position remains unchanged for QD's grown in water.

The origin of yellow luminescence due to oxygen vacancy was further supported by the experiment done with oxygen bubbled into the water during laser ablation of ZnO targets. Interestingly PL spectrum shows an emission peaking at 408 nm and 427 nm in the violet blue region, suppressing the yellow emission (figure 6.6(a)) when oxygen was bubbled through liquid during the ablation.

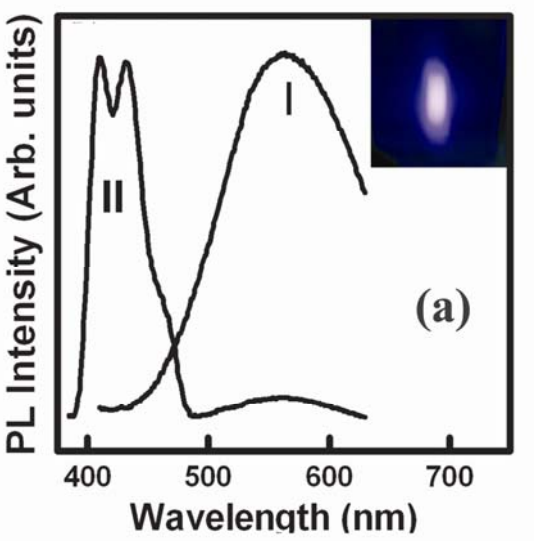

Figure 6.6 (a) PL spectra of ZnO QD's prepared without (curve I) and with (curve II) oxygen atmosphere. Inset shows the photo of bluish- violet luminescence.

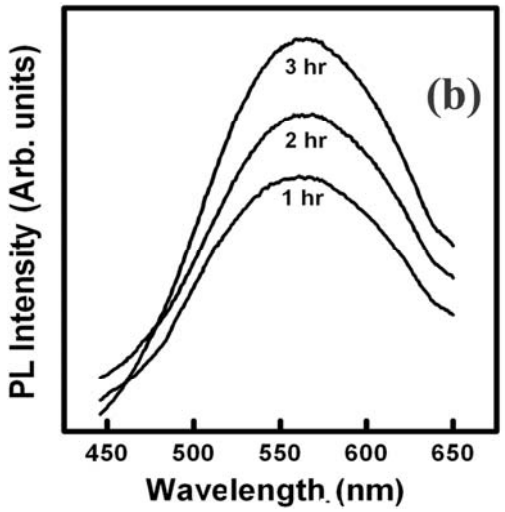

Figure 6.6 (b) PL spectra of ZnO QD's in water for various duration of ablation.

This emergence of deep bluish-violet emission opens the possibility of tuning emission color for different bio-medical applications. Inset of figure 6.6(a) shows the photograph of deep bluish-violet emission. Due to the bubbling of oxygen during ablation, defect density was considerably reduced tending to more stoichiometric ZnO QD's. This further supports that yellow luminescence originates from oxygen vacancies. Emission at 408 nm is due to the transition of electrons from shallow donor levels to valance band [28]. According to Lin *et al* [29] the energy gap between the valance band and energy level of interstitial zinc is 2.9 eV. This is very well consistent with PL emission at 427 nm in the present study. The future application potential of ZnO quantum dots resides in biomedical field, growth of QD's in bio-friendly medium like water and it's luminescent emission was studied for various ablation time. Figure 6.6(b) shows the PL of QD's dispersed in water prepared at different ablation times 1 hr, 2 hr and 3 hr keeping the laser fluence as 45 mJ/pulse. It is found that PL intensity increases with duration of laser ablation without any shift in PL peak position. The increase in PL intensity is due to the increased density of QD's of same size. The transparency of prepared ZnO QD's remained as such even though the duration of ablation was 3 hrs. The maximum concentration of ZnO QD's that can be achieved keeping the transparency was 17.5 μg/ml. But when the duration of ablation increased to 4 hrs, the resultant water containing ZnO QD's became turbid.

Semiconductor QD's have been covalently linked (*in vivo*) to biorecognition molecules such as peptides, antibodies and nucleic acids for application as fluorescent probes [30, 31]. The ZnO QD's prepared in the present study can be used in various bio-medical applications by conjugating with

ligands like poly ethylene glycol (PEG) soluble in both medium. Then it can be used as florescent probes in cancer targeting and imaging by attaching the corresponding antibodies to the bare surface of ZnO QD's.

6.4. Conclusion

In conclusion, highly transparent, deep yellow and bluish-violet emitting, bio-compatible 7 nm sized ZnO QD's were prepared in various liquid media using LP-PLA technique without using any surfactant. The emission wavelength was tuned by playing the defect chemistry and varying the laser fluence. The origin of yellow luminescence is due to oxygen vacancies. Highly luminescent bio-friendly ZnO QD's can be used as florescent probes in cancer diagnosis and therapy.

6.5. References

1. Y. Wu and P. Yang, Chem.Mater., **12** (2000) 605.

2. A. M. Morales and C. M. Lieber, Science **279** (1998) 208.

3. W. S. Shi, Y. F. Zheng, N. Wang, C. S. Lee and S. T. Lee J. Vac, Sci.Technol. *B* **19** (2001) 115.

4. Y. Cui, Q. Wei, H. Park and C. M. Leiber, Science, **293** (2001) 1298.

5. M. H. Huang, S. Mao, H. Feick, H.Yan, Y. Wu, H. Kind, E.Weber, R. Russo and P.Yang, Science, **292** (2001) 1897.

6. K. Manzoor, S. R. Vadera and N. Kumar, App. Phys. Lett. **84** (2004) 284.

7. J. T. Andrews and P. Sen, J. Appl. Phys, **91** (2002) 2827.

8. L. V. Asryana, M. Grundmann, N. N. Ledentsov, O. Stier, D. Bimberg, J. Appl. Phys, **90** (2001) 1666.

9. X. Gao, Y. Cui, R. M. Levenson, L. W. K.Chung and S. Nie, Nature Biotechnology **22** (2004) 969.

10. K. V. P. M Shafi, S. Wizel, T. Prozorov and A. Gedanken, ThinSolid Films **318** (1998) 38.

11. S. P. Gubin and J. D. Kosobudskii,. Russ. Chem. ReV. **52** (1983) 776.

12. J. Shi, S Gilder, K Babcock and D. D Awschalom, Science **271**, (1996) 937.

13. A. Henglein, J. Phys. Chem. **97 (**1993) 5457.

14. G.W. Yang and J.B Wang , Appl. Phys. A-Mate., **71** (2000) 343.

15. C.H. Liang, Y. Shimizu, M. Masuda, T. Sasaki and N. Koshizaki , Chem. Mater. **16** (2004) 963.

16. L. Yang, P.W May, L.Yin, J.A Smith and K.N Rosser, Diamond Relat. Mater. **16** (2007) 725.

17. J.B. Wang, G.W Yang, C.Y. Zhang, X. L. Zhong and Z.H.A Ren Chem. Phys. Lett. **367** (2003) 10.

18. A.V. Simakin, V.V Voronov, N .A Kirichenko and G.A. Shafeev, Appl. Phys. A-Mater, **79** (2004) 1127.

19. G.A. Shafeev, E. Freysz and F. Bozon-Verduraz, Appl. Phys. A-Mater, **78** (2004) 307.

20. J.P. Sylvestre, S. Poulin, A.V. Kabashin, E. Sacher, M. Meunier and J.H.T Luong, J.Phys. Chem. *B* **108** (2004) 16864.

21. S .I. Dolgaev, A.V. Simakin, V.V. Voronov, G.A Shafeev and F. Bozon-Verduraz Appl. Surf. Sci. **186** (2002) 546.

22. G. Thomas, *Chemistry for Pharmacy and Life Sciences: Including Pharmacology and Biomedical Science* (Englewoods cliffs, NJ: Pentice Hall) (Padstow: T J Press) (1996).

23. H.B. Zeng, W.P. Cai, B.Q. Cao, J.L. Hu, Y. Li and P.S. Liu Appl. Phys. Lett. **88** (2006) 181905.

24. H.B. Zeng, W.P. Cai, Y.Li, J.L. Hu and P.S. Liu J. Phys.Chem. *B* **109** (2005) 18260.

25. B. Vineetha, K. Manzoor, R. S. Ajimsha, P. M. Aneesh and M. K. Jayaraj Proceedings of 4th International Conference on Materials for Advanced Technology, Symposium M (ICMAT 2007) p. 31

26. W.T. Nichols, T. Sasaki, and N. Koshizaki, J.App.Phys, **100** (2006) 114913

27. L. Brus *J. Phys. Chem.* **90** (1986) 2555.

28. H. Zeng, W. Cai, J. Hu, G. Duan, P. Liu, and Y. Li, Appl. Phys. Lett. **88** (2006) 171910.

29. B. X. Lin, Z. X. Fu and Y. B. Jia, Appl. Phys. Lett. **79** (2001) 943.

30. M. R Gwinn and V. Vallyathan, Environ Health Persp. **114** (2006)1818.

31. X. Gao, Y. Cui, R. M. Levenson, L. W. K.Chung and S. Nie, Nature Biotechnology **22** (2004) 969.

Chapter 7

Summary and outlook

7.1. Summary

Development of p and n type transparent conducting oxides have opened up new and exciting applications. The active devices that are transparent to visible light including diodes, transistors and field effect transistors can be fabricated. All transparent $AgCoO_2$/n-ZnO heterojunction diodes were fabricated for the first time by pulsed laser deposition in the present study. Crystallinity and surface morphology of the $AgCoO_2$ films can be improved by optimising the deposition parameters. This would leads to better interface which will result in the diode with improved quality.

With the intention of integrating ZnO with already matured silicon technology, ZnO films were deposited on p-type Si (100) wafer using PLD at room temperature. All the junctions fabricated at different oxygen pressures were found to be rectifying with variation in turn on voltage. Variation of turn on voltage with oxygen pressure was modelled with Anderson model. Turn on voltage was found to be higher in all the diode fabricated owing to the interfacial defects. Interfacial defects would be reduced by optimising the deposition parameters which will improve the quality of the heterojunctions. This will increase the possibility of application in the area of photo detectors.

All oxide devices are being fabricated and they use of the potential advantages of transparency, high temperature performance and radiation hardness [1]. Transparent thin film transistor (TFT) utilising TCO as channel layer has several merits. The oxide TFT has advantage over the semiconductor FET in high voltage, temperature tolerances and are insensitive to visible light radiation. UV–LED is a typical active device utilising optical transparency and p-n junction. Near UV emission has been achieved by p type $SrCu_2O_2$ and n type

ZnO [2]. Improving the device that has been fabricated in the present study can yield UV emitting LEDs.

ZnO based nanostructures were attracting the interest of researchers worldwide due to its exciting optoelectronic applications. ZnMgO/ZnO multiple quantum wells (MQW) were grown using PLD at low temperature (400^{o}C). Temperature dependent photoluminescence (PL) studies were carried out on the MQW grown and it is found that PL peak position blue shifted considerably due to quantum size effects. The quality of the individual layers of ZnO and ZnMgO can be improved by the optimisation of the deposition parameters. This will enhance the luminescent properties of the ZnMgO/ZnO quantum well with possibility of application in lasing actions. ZnO nanorods were grown by PLD at room temperature and its room temperature photoluminescence was observed. By playing the deposition parameters, ZnO nanorods can be aligned in various directions according to the possible applications.

Semiconductor quantum dots have been covalently linked to biological molecules peptides, antibodies and nucleic acids for application as fluorescent probes [3]. Liquid phase pulsed laser ablation (LP-PLA) had been employed to synthesise of Zn/ZnO coreshell structure directly from Zn metal using sodium dodecyl sulphate (SDS) as surfactant [4]. In present study, transparent, biocompatible, monodispersed and 7 nm sized ZnO quantum dots were prepared in water by liquid phase pulsed laser ablation (LP-PLA) without the aid of any surfactant. This was the first report of surfactant free ZnO quantum dots synthesized directly from ZnO targets. These ZnO quantum dots were highly luminescent when illuminated with UV radiation. These surfactant free, highly luminescent ZnO quantum dots are promising candidate for biological

applications. ZnO quantum dots can be tagged with biomolecules with aim of using as fluorescent probes in cancer diagnosis and therapy. Surfactant free nature of ZnO quantum dots will be playing key role in increasing the easiness of attaching biomolecules according to application requirements. Our preliminary studies shows that ZnO quantum dots has been found to have excellent optical limiting properties owing to its quantum size effects [5]. The transparent ZnO quantum dots can be embedded in poly vinyl alcohol (PVA) matrix and will be deposited on glass plate to get films. These films could be used as optical limiters. The transparency of the ZnO quantum dots will reduce the possibility of scattering and thereby avoiding the chances of other optical process to interfere the optical limiting properties.

7.2. References

[1.] A.Kudo, H.Yanagi, K.Ueda, H.Hosono, H.Kawazoe and Y. Yano, Appl. Phy. Lett. **75** (1999) 285.

[2.] H Ohata, K Kawamura, M Oita, N Sarukura and H Hosono, Appl. Phys. Lett. **77** (2000) 475.

[3.] X. Gao, Y. Cui, R. M. Levenson, L. W. K. Chung and S. Nie, Nat. Biotechnol. **22** (2004) 969.

[4.] H. B. Zeng, W. P. Cai, B. Q. Cao, J. L. Hu and P. S. Liu, J. Phys. Chem. B. **109** (2005) 18260.

[5.] R. Sreeja, Manu George and M. K. Jayaraj (Communicated to SPIE workshop, Singapore)